

Characterisation of quantum channels in plasmonic metamaterials and bulk optical systems

by

Solomon Akpore Uriri, BSc(Hons), MSc



School of Chemistry and Physics

University of KwaZulu-Natal

A thesis submitted in fulfilment of the requirements for the degree of
Doctor of Philosophy

November 19, 2018

Abstract

Quantum channels are key to our understanding of how quantum information can be processed and transmitted. In this respect, over the past decade light has become an important carrier of quantum information. More recently, metamaterials have opened up many new exciting ways of controlling and manipulating light in the quantum regime, and in particular, controlling the polarisation and orbital angular momentum of light. In this work, we undertake an indepth characterisation of quantum channels made from plasmonic metamaterials and bulk optical systems by probing them with quantum states of light. We first experimentally demonstrate the active control of a plasmonic metamaterial operating in the quantum regime. Using an external laser, we control the temperature of the metamaterial and carry out quantum process tomography on single-photon polarization-encoded qubits sent through, characterizing the metamaterial as a variable quantum channel. We find that the overall polarization response can be tuned by up to 33%. Second, we experimentally realise a more complicated type of quantum channel in the form of a non-Markovian process made from the sum of two Markovian processes, and a Markovian process from two non-Markovian processes in a comparable bulk optical system. We perform quantum process tomography, and obtain high process fidelities. We discuss how these more complex types of quantum channel may be implemented using metamaterials.

Preface

The experimental work reported in this dissertation was carried out in the School of Chemistry and Physics, University of KwaZulu-Natal, under the supervision of Prof. Mark Tame. As the candidates supervisor I have approved this dissertation for submission.

Prof Mark Tame

Date

Declaration

I, Solomon Akpore Uriri declare that

1. The research reported in this thesis, except where otherwise indicated, is my original research.
2. This thesis has not been submitted for any degree or examination at any other university.
3. This thesis does not contain other persons data, pictures, graphs or other information, unless specifically acknowledged as being sourced from other persons.
 - (a) This thesis does not contain other persons writing, unless specifically acknowledged as being sourced from other researchers. Where other written sources have been quoted, then:
 - (b) Their words have been re-written, but the general information attributed to them has been referenced; Where their exact words have been used, their writing has been placed inside quotation marks and referenced.
4. This thesis does not contain text, graphics or tables copied and pasted from the Internet, unless specifically acknowledged, and the source being detailed in the thesis and in the References sections.

Signed:  _____

List of Publications

1. S. A. Uriri, T. Tashima, X. Zhang, M. Asano, M. Bechu, D. O. Guney, T. Yamamoto, S. K. Ozdemir, M. Wegener, and M. S. Tame. Active control of a plasmonic metamaterial for quantum state engineering. *Physical Review A*, 97, 053810, 2018.
2. S. A. Uriri, T. Tashima, and M. S. Tame. Experimental characterisation of a metamaterial polariser in the quantum regime. 61st Annual Conference Proceedings of the South Africa Institute of Physics- pg 194 – 199, December 2017.
3. S. A. Uriri, F. Wudarski, I. Sinayskiy, F. Petruccione, and M. S. Tame. Experimental realisation of a non-Markovian process from two Markovian processes and a Markovian from two non-Markovian processes, *in preparation*, 2018.

Acknowledgements

"Genius is one percent inspiration, ninety-nine percent perspiration."

— *Thomas A. Edison*

I am indeed grateful to the Almighty God for the gift of life and for giving me the best supervisor. I would like to express my profound appreciation to my supervisor Prof. Mark S. Tame whose constructive criticisms, suggestions, patience and inestimable assistance, enhanced the quality of this research study. May the Almighty God continue to guide, protect and uplift you in all manners of life.

Special thanks to my parents Overseer & Deaconess John Uriri for their constant encouragement, support, care and prayers during the course of this project. To my love and wife, Favour Omenuwoma Solomon-uriri, my deepest gratitude for your love, understanding, care and prayers you shown to me all through till the end of this project. Many thanks to my only dearest brother, Dr. Nelson Oghenekaro Odume for your constant motivation and always being there for me.

I would like to thank the National Research Foundation of South Africa for providing financial support in the form of bursary through the NRF grant-linked bursary scheme and for sponsoring my travel trip to attend the international conference on quantum and nonlinear optics (QNO), Malaysia, February 2018 and the South Africa Institute of Physics Annual Conference, Cape Town, South Africa. To the University of KwaZulu-Natal, I say thank you for providing a conducive research environment in the form of laboratories, wonderful staff and science equipment that made this project possible. The university refined me into a growing and a professional physics scholar.

I must not forget to acknowledge the staff of the Physics Department, my fellow colleagues and friends for the wonderful time we had together. God bless you all!!!

Dedication

I dedicate this project to my parents Overseer & Deaconess John Uriri. Your endless motivation, love, support inspired me to accomplish this work.

Contents

Abstract	ii
Preface	iv
Declaration	iv
List of Publications	iv
Acknowledgements	ii
Dedication	iv
List of Figures	viii
List of Tables	xvi
1 Introduction	1
1.1 Background	1
1.2 Aim of the study	7
1.3 Synopsis of thesis	8
2 Basic Tools and Techniques	9
2.1 Localised Surface Plasmon	9
2.1.1 Sub-wavelength metal particles	10

2.1.2	The dielectric function of the free electron gas	12
2.1.3	Scattering and absorption by small particles compared with the wavelength	13
2.2	Electromagnetic theory of materials	15
2.2.1	Fabrication techniques	21
2.3	Quantum mechanics	28
2.3.1	Vector Spaces	28
2.3.2	Linear Operators and Matrices	28
2.3.3	Pauli Matrices	29
2.3.4	Inner products	29
2.3.5	Eigenvectors and Eigenvalues	30
2.3.6	Adjoint and Hermitian Operators	31
2.3.7	Commutator and Anti-commutator	31
2.3.8	Quantum measurements	31
2.3.9	Density operator	34
2.3.10	Quantum State Tomography	35
2.3.11	Quantum Process Tomography	37
2.4	Quantum Optics	40
2.4.1	Light in the quantum regime	40
2.4.2	Single-Photon Source	45
3	Active control of a plasmonic metamaterial for quantum state engineer-	
	ing	52
3.1	Introduction	52
3.2	Transmission of single-photons through plasmonic metamaterials: Simulations	54
3.3	Temperature dependence of single photon transmission via plasmonic meta-	
	materials: Simulations	56
3.3.1	Temperature dependence of the permittivity of fused-silica	56

3.3.2	Temperature dependence of the permittivity of gold	57
3.3.3	Temperature dependence of plasmonic metamaterials in the quantum regime	59
3.4	Transmission of single photons through plasmonic metamaterials: Experiment	63
3.4.1	Experimental setup	63
3.4.2	Quantum State probing	65
3.4.3	Results and discussion	66
3.5	Temperature dependence of a plasmonic metamaterial in the quantum regime: Experiment	73
3.5.1	Experimental setup	73
3.5.2	Results and discussion	76
4	Markovian and non-Markovian quantum channels	86
4.1	Introduction	86
4.2	Markovian Quantum channels	88
4.2.1	Non-Markovian process from two Markovian processes	90
4.2.2	Determining Markovianity	92
4.3	non-Markovian quantum channels	94
4.3.1	Markovian process from two non-Markovian process	94
4.4	Experimental setup/procedure	95
4.4.1	Results and discussion	100
5	Conclusion	107
	References	110

List of Figures

1.1	An experimental demonstration showing the resonance curve of a copper split-ring resonator (inset) with $c = 0.8$ mm, $d = 0.2$ mm and $r = 1.5$ mm. The resonance is about 4.845 GHz, and measured quality factor $Q > 600$. Figure taken from Smith et al. [22]	4
2.1	A diagram of a homogenous sphere placed in an electrostatic field [85].	11
2.2	A diagram of light scattering by an obstacle (a particle).	14
2.3	Properties of metamaterials based on ϵ and μ	21
2.4	Scanning electron microscope image of a NIM sample based on the fishnet geometry suggested in [32] fabricated using EBL, followed by electron-beam evaporation and lift-off. The structure is made up of two layers of silver separated by a 10 nm thick layer of aluminium which operates at a wavelength of 813 nm. Taken from [30, 31].	24
2.5	SEM image of a $16 \mu\text{m} \times 16 \mu\text{m}$ array of SRRs fabricated using FIB writing, with the inset showing the magnified image of the magnetic metamaterial. Taken from [96].	25
2.6	SPDC experimental setup. Here, a BBO (β -barium borate) is a nonlinear crystal, IF is an interference filter, and A and B are avalanche photo-detectors.	46

2.7	A diagram of a Hanbury-Brown and Twiss interferometer, with associated electronics. The output of arm B of the SPDC is connected to the input arms of the interferometer. Here, SM is a single-mode fibre, MM is a multi-mode fibre, FC is a fibre coupler, M is a mirror, BS is a beam splitter, and A, B, and B' are avalanche photo detectors. SPCM is a single-mode counting module.	49
2.8	A plot of the degree of second-order coherence as a function of delay time. The solid line is for 3 detectors, while the dotted line is for 2 detectors. . .	50
3.1	A schematic diagram of the metamaterials investigated in this thesis. . . .	53
3.2	Theoretical transmission spectra for horizontally (orange line) and vertically (blue line) polarised light sent through a plasmonic metamaterial made of gold nanorods ($w = 39$ nm, $l = 110$ nm, $t = 30$ nm). The dashed line corresponds to 810 nm.	55
3.3	Temperature dependence of the permittivity ϵ_d of the silica substrate. . . .	57
3.4	Temperature dependence of the permittivity ϵ_m of the gold used for the nanorods. (a) $\text{Re}[\epsilon_m]$ and (b) $\text{Im}[\epsilon_m]$	58
3.5	Temperature-dependent transmission response of a plasmonic metamaterial with nanorod dimensions, width $w = 46$ nm and length $l = 130$ nm (theory). The period is fixed at $d_x = d_y = 200$ nm and the thickness is $t = 30$ nm. In (a) the lower solid resonance curve is for vertical transmission at $T = 300$ K and the lower dotted resonance curve is for vertical transmission at $T = 340$ K. The horizontal solid line is for horizontal transmission. (b) Corresponding temperature dependence over a range of 50 K at $\lambda = 810$ nm with the nanorod dimensions chosen as those used in (a).	60

- 3.6 Temperature-dependent transmission response of a plasmonic metamaterial with nanorod dimensions: width $w = 47$ nm and $l = 140$ nm (theory). The period is fixed at $d_x = d_y = 200$ nm and the thickness is $t = 30$ nm. In (a) the lower solid resonance curve is for vertical transmission at $T = 300$ K and the lower dotted resonance curve is for vertical transmission at $T = 340$ K. The horizontal solid line is for horizontal transmission. (b) Corresponding temperature dependence over a range of 50 K at $\lambda = 810$ nm with the nanorod dimensions chosen as those used in (a). 61
- 3.7 Temperature-dependent transmission response of a plasmonic metamaterial with nanorod dimensions: width $w = 48$ nm and $l = 144$ nm. (theory). The period is fixed at $d_x = d_y = 200$ nm and the thickness is $t = 30$ nm. In (a) the lower solid resonance curve is for vertical transmission at $T = 300$ K and the lower dotted resonance curve is for vertical transmission at $T = 340$ K. The horizontal solid line is for horizontal transmission. (b) corresponding temperature dependence over a range of 50 K at $\lambda = 810$ nm with the nanorod dimensions chosen as those used in (a). 62
- 3.8 Transmission response of a metamaterial with nanorod dimensions corresponding to figure 3.5(a) in the middle and with ± 2 nm added to the length, width and thickness. A larger variation of the nanorod size leads to even bigger shifts in the response. 62
- 3.9 Overview of the experiment. (a) Experimental setup. Here, L is a convex lens, HWP and QWP are a half- and quarter-wave plate, BiBO is a non-linear crystal, PBS is a polarising beamsplitter, IF is an interference filter (800 nm and $\Delta\lambda = 40$ nm) and D_A and D_B are avalanche photodetectors. (b) Telescope system for imaging the alignment laser and its position on different metamaterials. FM is a flip mirror. (c) Image of metamaterials with the alignment beam on a particular design. 65

3.10	Transmission coefficients of horizontally (black) and vertically (grey) polarised single photons (at 810 nm) through different plasmonic metamaterials (nanorods with $w = 39$ to 47 nm, $l = 110$ nm, $t = 30$ nm) obtained via experiment. The nanorod widths increase from left to right.	68
3.11	Quantum state tomography of probe states sent through the substrate and metamaterial. Real and imaginary parts of the output state ρ_{exp} obtained from the state $ H\rangle$ sent through the substrate and metamaterial.	69
3.12	Quantum state tomography of probe states sent through the substrate and metamaterial. Real and imaginary parts of the output state ρ_{exp} obtained from the state $ V\rangle$ sent through the substrate and metamaterial.	70
3.13	Quantum state tomography of probe states sent through the substrate and metamaterial. Real and imaginary parts of the output state ρ_{exp} obtained from the state $ +\rangle$ sent through the substrate and metamaterial.	71
3.14	Quantum state tomography of probe states sent through the substrate and metamaterial. Real and imaginary parts of the output state ρ_{exp} obtained from the state $ L\rangle$ sent through the substrate and metamaterial.	72

3.15	Overview and experimental setup for demonstrating active control of a metamaterial in the quantum regime. (a) Pictorial representation of one of the metamaterials used with a single photon (red) and an active control laser beam (white) sent through. The spot size of the control and single-photon beams are the same in the experiment; however, the control beam is shown smaller for pictorial purposes. The inset shows a three-dimensional figure of the nanorods in each unit cell (dimensions considered are given in the main text). (b) Experimental setup, where a nonlinear BiBO crystal is pumped at 405 nm, producing pairs of photons at 810 nm via spontaneous parametric down-conversion. One photon is detected at detector D_A and heralds the presence of a single photon in the other arm. Here H is a half-wave plate, Q is a quarter-wave plate, L is a plano-convex lens ($f = 25$ mm), PBS is a polarizing beam splitter, IF is an interference filter ($\lambda = 810$ nm and $\Delta\lambda = 10$ nm), and D_A and D_B are single-photon detectors.	75
3.16	Theory and experiment compared.	77
3.17	Temperature-dependent transmission response of a metamaterial (experiment). (a) Atomic force microscope image. See the main text for dimension details. (b) Classical transmission spectra of the metamaterial at T_0 for horizontal (squares) and vertical (circles) polarized light. The spectra was measured using frustrated total internal reflection (FTIR). (c) Transmission probabilities in the quantum regime for single qubits encoded into the vertical polarization of single photons as $ V\rangle$ and sent through the metamaterials as the temperature is changed. The five different temperature settings are $T_0 = 295$ K, $T_1 = 303$ K, $T_2 = 319$ K, $T_3 = 331$ K, and $T_4 = 347$ K, corresponding to values consistent with the range used in the theoretical model. The values are determined by the laser power used and are spaced apart by approximately 10 K	80

- 3.18 Temperature-dependent transmission response of a metamaterial (experiment). (a) Atomic force microscope image. See the main text for dimension details. (b) Classical transmission spectra via FTIR of the metamaterial at T_0 for horizontal (squares) and vertical (circles) polarized light. (c) Transmission probabilities in the quantum regime for single qubits encoded into the vertical polarization of single photons as $|V\rangle$ and sent through the metamaterials as the temperature is changed. The five different temperature settings are $T_0 = 295$ K, $T_1 = 303$ K, $T_2 = 319$ K, $T_3 = 331$ K, and $T_4 = 347$ K, corresponding to values consistent with the range used in the theoretical model. The values are determined by the laser power used and are spaced apart by approximately 10 K 81
- 3.19 Temperature-dependent transmission response of a metamaterial (experiment). (a) Atomic force microscope image. See the main text for dimension details. (b) Classical transmission spectra via FTIR of the metamaterial at T_0 for horizontal (squares) and vertical (circles) polarized light. (c) Transmission probabilities in the quantum regime for single qubits encoded into the vertical polarization of single photons as $|V\rangle$ and sent through the metamaterials as the temperature is changed. The five different temperature settings are $T_0 = 295$ K, $T_1 = 303$ K, $T_2 = 319$ K, $T_3 = 331$ K, and $T_4 = 347$ K, corresponding to values consistent with the range used in the theoretical model. The values are determined by the laser power used and are spaced apart by approximately 10 K 82
- 3.20 Quantum process tomography χ matrices for the first metamaterial at the reference temperature (T_0). (a) and (c) Real and imaginary parts of the experimental χ matrix at T_0 . (b) and (d) Real and imaginary parts of an ideal partial polarizer χ matrix with $T_V = 0.476$ 84

3.21	Quantum process tomography χ matrices for the first metamaterial at the final temperature (T_4). (a) and (c) Real and imaginary parts of the experimental χ matrix at T_4 . (b) and (d) Real and imaginary parts of an ideal partial polarizer χ matrix with $T_V = 0.476$	85
4.1	Representation of a system-environment time-dependent unitary transformation. The entire system is 'closed', but the dynamics of the system alone can be described using open quantum system techniques.	88
4.2	Time dependent probability for application of σ_x and σ_y in Eq. 4.12. The points at various times represent possible times at which the channels could be realized for.	92
4.3	Time-dependent probabilities p_1 and p_2	95
4.4	Overview and experimental setup for realising Markovian and non-Markovian channels. Experimental setup, where a nonlinear BiBO crystal is pumped at 405 nm, producing pairs of photons at 810 nm via spontaneous parametric down-conversion. One photon is detected at detector D_A and heralds the presence of a single photon in the other arm. Here H is a half-wave plate, Q is a quarter-wave plate, PBS is a polarizing beam splitter, BS is a beam splitter, ND is neutral density filter, IF is an interference filter ($\lambda = 810$ nm and $\Delta\lambda = 10$ nm), and D_A and D_B are single-photon detectors. (b) shows the top channel waveplates and angles settings and (c) shows the bottom channel waveplates and angles settings.	98
4.5	Expected behaviour of individual channels: top or bottom (Markovian)	99
4.6	Expected behaviour of the joint channel (non-Markovian). Similar behaviour for other starting times s with the maximum negative value becoming more negative for larger s	99
4.7	Individual channels for times $s = 0.5$ and $t = 0.75$	102
4.8	Joint channel for times $s = 0.5$ and $t = 0.75$	102

4.9	Individual channels for times $s = 2$ and $t = 2.25$	102
4.10	Joint channel for times $s = 2$ and $t = 2.25$	103
4.11	Using ideal counts for top and bottom channels for times $s = 0.5$ and $t =$ 0.75	103
4.12	Using ideal counts for the joint channel for times $s = 0.5$ and $t = 0.75$. . .	103
4.13	Top and bottom channels for time-distribution for $s = 0.6$ and $t = 1.2$. . .	104
4.14	Both channels combined for times $s = 0.6$ to $t = 1.2$	105
4.15	Using Ideal counts for top and bottom channels for times $s = 0.5$ to $t = 0.75$	105
4.16	Using Ideal counts for both channels combined for times $s = 0.6$ to $t = 1.2$	106

List of Tables

2.1	Counts rate at zero time delay	51
3.1	Fidelity and purity for the single-photon probe states. The error bars here and elsewhere are obtained from a 100 run Monte Carlo simulation which uses the collected data and adds Poissonian noise on the counts, as this is the main source of noise in down-conversion experiments.	72
3.2	Process fidelities for the three metamaterials investigated as the temperature is changed, as well as horizontal and vertical transmission probabilities T_H and T_V extracted from maximizing the process fidelity, respectively. The error bars here and elsewhere are obtained from a 100 run Monte Carlo simulation which uses the collected data and adds Poissonian noise on the counts, as this is the main source of noise in down-conversion experiments.	85
4.1	Process fidelity of the channels for different times for the top, bottom and joint channels.	100
4.2	Process fidelity at different time-distribution for top, bottom and joint channels.	106

Chapter 1

Introduction

1.1 Background

Interest in metamaterials and plasmonics has been growing rapidly for the past 15 years within the scientific community. The increase in publication of scientific papers in this field in recent years is enormous due to the range of applications of metamaterials in various fields including optics, physics, remote sensing, aerospace, quantum optics/communication, electrical engineering, radar systems and many more [1].

The prefix meta is a Greek ($\mu\epsilon\tau\alpha$) preposition - meaning "after", or "beyond", and in this way, metamaterials mean artificial materials beyond conventional materials found in nature. However, the exact meaning of metamaterials is still vague, and a unique and accepted interpretation is yet to be established. For example, the European Union's Metamorphose Network, defines metamaterials as "an arrangement of artificial structural elements, designed to achieve advantageous and unusual electromagnetic properties" [2]. In their book, Wenshan Cai and Vladimir Shalaev [1] define metamaterials as an artificially structured material which attains its properties from the unit structure rather than the constituent materials. Wikipedia [3] describes them as materials engineered to have properties that have not yet been found in nature. Elsewhere, Cui et al. [4] defines a

metamaterial as a macroscopic composite of periodic or non-periodic structures whose function is due to both the cellular architecture and the chemical composition. From the definitions given above, they all point to a central meaning which is that metamaterials are artificially made materials consisting of unit cells or meta-atoms, whether periodic or non-periodic, having special properties that are not found in conventional materials. Metamaterial properties depend on the constituents and how the unit cells are designed. Metamaterials are designed to have an electromagnetic response, that is, effective electric permittivity ϵ and magnetic permeability μ that can be positive, negative or simultaneously negative. These electromagnetic properties make them useful materials that can be used to control the propagation of electromagnetic waves in matter.

History

Metamaterials research started long before the name "metamaterial" was suggested by Rodger M. Walser in 1999, a Professor of Physics at the University of Texas [5]. Before this, several terminologies were used to describe metamaterials, including left-handed substance [6], artificial dielectric material [7, 8, 9], and backward-wave media [10, 11]. The first artificial dielectric materials appear to have been put-forward by Chunder Bose in 1898 in his first microwave experiment in which an artificial chirality effect was observed [7]. Subsequently, Lindman in 1914 studied artificial chiral materials through which electromagnetic waves pass by, made by many randomly oriented small wire helices in a host material [9]. Thereafter, artificial dielectric materials that are arranged periodically in many numbers of wires, plates or spheres were reported in the literature [8, 12, 13, 14]. For example, Kock in 1948 developed lightweight microwave lenses by arranging conducting spheres, disks and strips periodically and effectively tailoring the refractive index of the artificial media [8]. Artificial dielectric materials were later reported with spring-ring-resonators [15, 16], bianisotropic and chiral elements [17], and arrayed frequency filters [18].

The concept of left-handed materials, which are now known as double negative metamaterials (DNM) [19], was first proposed theoretically by Veselago in 1967 theoretically [6]. In his work, he showed the possibility of producing plane electromagnetic-wave propagation with negative ϵ and μ using the Poynting vector ($\mathbf{S} = \mathbf{E} \times \mathbf{H}$), where \mathbf{S} is the Poynting vector, and \mathbf{E} and \mathbf{H} are the usual electric field and magnetic field, respectively. In contrast to materials available in nature where the vector \mathbf{S} always forms a right-handed set with vectors \mathbf{E} and \mathbf{H} , and vector \mathbf{S} and the wave vector \mathbf{K} are in the same direction of propagation, left-handed materials have \mathbf{S} and \mathbf{K} in the opposite direction. Indeed, these were remarkable mathematical findings by Veselago, that have now had a significant impact on the scientific and technological communities.

A significant result was achieved when Pendry et al. in 1996 [20] proposed a mechanism for shifting the plasma frequency into the far infra-red or even GHz band. In their mechanism, the authors engineered an artificial electric plasma from a periodic structure made of very thin wires whose ϵ was negative. Subsequently, Pendry et al. in 1999 [21] realized a negative μ from an artificial magnetic plasma. A significant contribution to the field of metamaterials was made in 2000 when Smith et al. [22] experimentally demonstrated the prediction of Veselago's seminar paper, and subsequently Pendry's simulation work on the realization of a perfect lens [23]. In their seminar paper (see also figure 1.1), Smith et al. successfully reported an experiment in which a metamaterial that exhibits a frequency region in the microwave regime with simultaneously negative values of effective ϵ and μ . Indeed, it was a remarkable breakthrough because until this achievement, no one had been able to experimentally realize this novel and exciting type of artificial material with a simultaneous negative ϵ and μ , as predicted theoretically by Veselago in 1967. This breakthrough took three decades of active research on how to experimentally realize a metamaterial with simultaneous negative ϵ and μ .

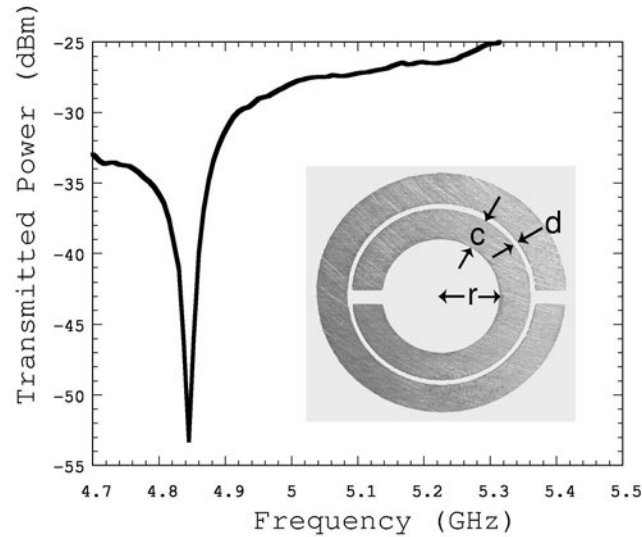


Figure 1.1: An experimental demonstration showing the resonance curve of a copper split-ring resonator (inset) with $c = 0.8$ mm, $d = 0.2$ mm and $r = 1.5$ mm. The resonance is about 4.845 GHz, and measured quality factor $Q > 600$. Figure taken from Smith et al. [22]

After this remarkable breakthrough, researchers started to show a keen interest in metamaterials and to understand how they can be applied to their respective research fields. Other important work in this field was made in 2005, when a gradient refractive index was engineered to diffract or bend electromagnetic waves [24], and in 2006 where metamaterials were used to realize an electromagnetic cloak and to control the propagation of electromagnetic waves [25, 26]. The work of Smith et al. [24] provided an alternative approach to develop gradient index lenses and similar optics even at high temperature. The authors described a structured metamaterial, based on a conducting split ring resonator which had an effective refractive index with a constant spatial gradient. Also, the work of Pendry et al. in 2006 [25] showed how a volume of space could be cloaked to exclude all electromagnetic fields. Pendry's work has a remarkable application to exotic lens design and the cloaking of objects from electromagnetic fields. The word "cloak" is simply used to mean hiding or making an object of a certain volume invisible to sight in an electromagnetic field. Around the same time, Leonhardt [26] developed a general recipe for the design

of media that can create perfect invisibility within the accuracy of geometric optics using a metamaterial. In general, an invisibility cloak is achieved by manipulating the traversal of light through a metamaterial. A metamaterial, based on transformation optics, directs and controls the propagation of the light spectrum, and thus shields an object from view by controlling the electromagnetic wave. Since then, research in metamaterials has taken different directions and several research topics have emerged. Some of these include: optical magnetism [21, 27, 28, 29], optical negative index materials [30, 31, 32, 33, 34], non-linear optics with metamaterials [35, 36, 37, 38], electromagnetic cloaking [39, 40, 41, 42, 43, 44], super-resolution with metamaterials [45, 46, 47, 48, 49], waveguides [50], metamaterial polarizers [51, 52, 53, 54], and very recently quantum metamaterials [55, 56, 57].

Quantum metamaterials

Recently, quantum applications of metamaterials have attracted researchers, most especially those in the field of quantum information science. Quantum metamaterials (QM) control electromagnetic waves by applying the laws of quantum mechanics. Here, the behaviour of the unit cells are described by Maxwell's and Schrödinger's equations. QM show coherent quantum dynamics, and this type of artificial material is a spatially extended controllable quantum object that allows additional ways of controlling the propagation of electromagnetic waves [55, 56].

Quantum metamaterials are therefore optical media that are made of quantum coherent unit structures with engineered parameters and exhibit controllable quantum states in these structures [58]. One of the exciting properties of QM is that they can preserve quantum coherence for longer than the transversal time of a significant electromagnetic wave or signal [59]. However, over the last few years, researchers have been actively studying the quantum applications of metamaterials using superconducting metamaterials [60], hyperbolic metamaterials [61], and plasmonic metamaterials [62, 63, 64]. A detailed review on

superconducting metamaterials is given by Jung et al [60], whereby photons interact with quantized energy levels in a meta-atom, with magnetic flux quantization and the Josephson effect, as well as strong diamagnetism present. Also, an enhancement in the photonic density of states resulting in a broadband Purcell effect for single photon sources using parabolic metamaterials has been demonstrated [65, 66]. On the other hand, research into the applications of plasmonic metamaterials for quantum information processing have been very successful and motivating. For example, the demonstration of the distillation of photon quantum entanglement using a plasmonic metamaterial [62], the coherent absorption of single photons in a deeply subwavelength absorber [63], and Hong–Ou–Mandel interference mediated by magnetic plasmon waves in a three-dimensional optical metamaterial [67]. Some other applications of quantum metamaterials include: the demonstration of a strong anisotropic quantum vacuum over macroscopic distances enabled by a judiciously designed array of subwavelength–scale nanoantennas [68] and tuneable negative permeability in a quantum plasmonic metamaterial [64]. Thus, in the quantum regime, encoded quantum information can be manipulated and controlled using metamaterials.

Quantum information processing

Quantum information processing (QIP) is a research field that deals with the processing of quantum information. In QIP, information is processed using the laws of quantum mechanics. Quantum mechanics began to evolve in the early twentieth century after Einstein’s discovery of the photoelectric effect [69]. Thereafter, major discoveries were made on the behaviour of physical objects at the microscopic level. These included wave-particle duality, where light behaves in some respects like a particle and in other respects like a wave [70, 71], and the uncertainty principle where the momentum and position of a photon (the basic unit of light) cannot be simultaneously measured with absolute precision [72]. In 1925, Erwin Schrödinger developed a mathematical model that describes the behaviour of a quantum mechanical wave [73], which has become central to quantum

mechanics. The model defines the permitted states of a quantum system, and describes how the quantum state of a physical system changes in time. More generally, the quantum state of any physical system is evolved and transmitted via a 'quantum channel'.

In the context of communication, a quantum channel is a channel through which quantum information is transmitted, and includes classical information. In an open quantum system, the interaction of physical systems with their environment during evolution can also be described via a quantum channel. A quantum channel, which is also known sometimes as a quantum operation, can be described by the master equation [74]. The equation approach is a generalised of Schrödinger's model and describes the system evolution and quantum noise in continuous time using differential equations. This equation has been used to describe memoryless and memory quantum channels. These channels are sometimes referred to as Markovian and non-Markovian processes. A Markovian (memoryless) stochastic process involves a channel whereby the future state of a system is only dependent on the present state and is independent of any prior state. On the other hand, a non-Markovian (memory) process is a process whereby the future state of the system is dependent on the present state and prior states. In this thesis, all these types of channel are probed and characterised in plasmonic metamaterials and bulk optical systems.

1.2 Aim of the study

Quantum channels are key information gateways through which quantum information is processed and transmitted. However, information transfer via these channels can be limited due to decoherence (loss of information) due to some physical factor. One of these factors in an optical context, is the loss of quantum information due to the coupling of single-photon states with an environment. A promising route to provide a solution to this problem is to look at the high field confinement in plasmonic metamaterials. Plasmonic metamaterials are a special type of metamaterial that consist of artificially engineered

nano-structures made from metallic-nanoparticles, having unusual optical properties that are not found in conventional materials. There has been tremendous growth in research into plasmonic metamaterials in the quantum regime, including the creation of entanglement with negative index metamaterials [75], tuneable negative permeability in a quantum plasmonic metamaterial [64], and other application including entanglement distillation for quantum state engineering [62], and novel ways of controlling light-matter interactions in a metasurface-enabled remote interference scenario [68]. However, none of the research conducted so far has looked at an indepth characterisation of quantum channels made from plasmonic metamaterials in the quantum regime.

The aim of this study is to find out how to exploit plasmonic metamaterials for realising different types of useful channels in the quantum regime, and use them in real-world applications. This is done by probing quantum states of light in plasmonic metamaterials and characterising the metamaterials as variable quantum channels. This study also looks at other ways of characterising quantum channels in comparable bulk optical systems in the quantum regime.

1.3 Synopsis of thesis

The thesis is organised as follows: Chapter 2 presents the basic tools and techniques that are used in the work. Chapter 3 describes the active control of a plasmonic metamaterial for quantum state engineering. Chapter 4 focusses on the theoretical and experimental realisation of Markovian and non-Markovian processes in bulk optics. A summary and recommendation for further study are given in Chapter 5.

Chapter 2

Basic Tools and Techniques

2.1 Localised Surface Plasmon

Plasmonics is the study of the interaction of the electromagnetic field and excited electrons at a metal-dielectric interface. The physics of plasmonics enables special ways to confine light to regions below the diffraction limit [76] for the localisation of light into subwavelength dimensions enabling strong field enhancement. This special feature has opened up some exciting applications, such as super-resolution imaging [23, 77, 78], enhanced sensing [79, 80], nanophotonic lasers and amplifiers [81, 82], optical metamaterials [83], antennas transmitting and receiving light signals at the nanoscale [84], and quantum information processing [62].

Plasmonics is divided into two types: Surface Plasmon Polaritons (SPPs) and Localised Surface Plasmons (LSPs). SPPs are infrared or visible-frequency excited electromagnetic waves travelling at the interface between a dielectric and a metal. These electromagnetic surface waves arise through the coupling of the oscillating electromagnetic fields [85]. SPPs can be excited at a planar interface using different methods including: Excitation upon charged particle impact, prism coupling, grating coupling, excitation using highly focused optical beams, and near-field excitations. On the other hand, LSPs are non-propagating

excitations of the free electrons of metallic nanoparticles coupled to the electromagnetic field. The size of these nanoparticles are usually smaller than the wavelength of the incident light. In LSPs, the plasmon resonance can be excited by direct light illumination, unlike propagating SPPs where phase-matching techniques have to be employed [85]. The strength of the electric fields near the particle's surface are greatly improved and the particle's optical absorption has a maximum at the plasmon resonant frequency. This resonance enhancement decays quickly with the distance from the surface and, for noble metal nanoparticles, the resonance occurs at visible wavelengths [86]. For semiconductor nanoparticles, the maximum optical absorption is often in the near-infrared and mid-infrared regions [87]. The nanoparticle resonance is usually described by the Frölich criterion [85]. This dipole particle condition is strictly valid only for vanishingly small particles, however, it represents a good approximation for particles small compared to the wavelength of interest. As a result of Ohmic loss and electron-core interactions, loss is inevitable for the plasmon oscillation, which is usually a disadvantage for most plasmonic devices. Meanwhile, if desired, the absorption of light in the metal can be enhanced greatly by carefully designing metal nanoparticle patterns in 2D or 3D. In this project, LSPs were experimentally studied, hence the remaining subsections of this section describe the LSP in detail. We start by looking at the normal modes of sub-wavelength metal particles.

2.1.1 Sub-wavelength metal particles

The interaction of a particle of size s , with the electromagnetic field can be described using the quasi-static approximation, provided the size is smaller than the wavelength of the incident electromagnetic wave [85, 88]. If we consider a homogenous isotropic medium (a sphere) as shown in Figure 2.1 of radius r in a uniform static electric field, $\mathbf{E} = E_0\mathbf{z}$, the potentials and electric field in the electrostatic approximation are given as $\nabla^2\phi = 0$ and $\mathbf{E} = -\nabla\phi$, respectively.

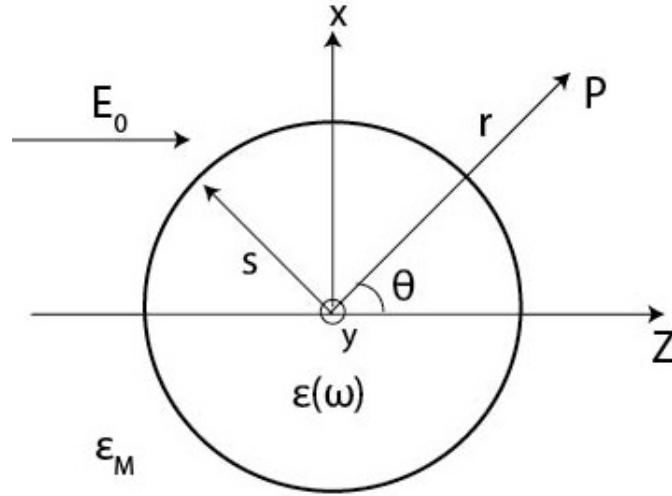


Figure 2.1: A diagram of a homogenous sphere placed in an electrostatic field [85].

Taking the dielectric constant $\epsilon = \epsilon(\omega)$ for the sphere and the frequency dependent dielectric function ϵ_m for the surrounding isotropic medium, the inside and the outside potentials are given as [85]

$$\phi_{in} = -\frac{3\epsilon_m}{\epsilon + 2\epsilon_m} E_0 r \cos\theta, \quad (2.1)$$

$$\phi_{out} = -E_0 r \cos\theta + \frac{\epsilon - \epsilon_m}{\epsilon + 2\epsilon_m} E_0 s^3 \frac{\cos\theta}{r^2}, \quad (2.2)$$

where ϕ_{out} describes the superposition of the applied electromagnetic field and a dipole located at the center of the particle. ϕ_{out} can be written with the dipole moment \mathbf{p} as

$$\phi_{out} = -E_0 r \cos\theta + \frac{\mathbf{p} \cdot \mathbf{r}}{4\pi\epsilon_0\epsilon_m r^3}, \quad (2.3)$$

$$\mathbf{p} = 4\pi\epsilon_0\epsilon_m s^3 \frac{\epsilon - \epsilon_m}{\epsilon + 2\epsilon_m} \mathbf{E}_0. \quad (2.4)$$

Here, it can be seen that a dipole moment is induced by the applied field inside the sphere that is proportional to the magnitude $|\mathbf{E}_0|$. The polarizability α of the sphere can be

defined through the dipole moment: $\mathbf{p} = \epsilon_0 \epsilon_m \alpha \mathbf{E}_0$ [88], where

$$\alpha = 4\pi s^3 \frac{\epsilon - \epsilon_m}{\epsilon + 2\epsilon_m} \quad (2.5)$$

Eq. 2.5 is the polarizability of a small sphere of subwavelength diameter in the electrostatic approximation. From this, it can be seen that α is greatly enhanced if the Frölich criterion $|\epsilon + 2\epsilon_m|$ is a minimum. For an ellipsoid with semi-axes $s_1 \leq s_2 \leq s_3$, we have α_j

$$\alpha_j = 4\pi s_1 s_2 s_3 \frac{\epsilon - \epsilon_m}{3\epsilon_m + 3L_j(\epsilon - \epsilon_m)}, \quad (2.6)$$

where L_j is a geometric factor and is given by

$$L_j = \frac{s_1 s_2 s_3}{2} \int_0^\infty \frac{dq}{(s_j^2 + q)f(q)}, \quad (2.7)$$

where $f(q) = \sqrt{(q + s_1^2)(q + s_2^2)(q + s_3^2)}$ and $j = 1, 2, 3$. Here, $\sum L_j = 1$ and for a sphere $L_1 = L_2 = L_3 = \frac{1}{3}$.

2.1.2 The dielectric function of the free electron gas

The optical properties of metals over a wide frequency range can be described by a plasmon model, where a gas of free electrons of number density n propagates against a fixed background of positive ion cores. The plasmon model was developed in 1927 from the combination of the classical Drude model with quantum mechanical Fermi-Dirac statistics by Arnold Sommerfeld [85]. In this model, one assumes that some aspects of the band structure are incorporated into the effective optical mass m of each electron [85]. The oscillation of the free electrons is damped through collisions occurring with a characteristic collision frequency $\gamma = \frac{1}{\tau}$, where τ is the relaxation time of the free electron gas. τ is of the order of 10^{-14} s at room temperature, corresponding to 100 THz [85]. Thus, assuming a harmonic time-dependence $\mathbf{E}(t) = \mathbf{E}_0 e^{-i\omega t}$ of the driving field, a particular solution

for the electron motion is given as $\mathbf{x}(t) = \mathbf{x}_0 e^{-i\omega t}$, where \mathbf{x}_0 is the complex amplitude which creates any phase shift between the driving field and the response through $\mathbf{x}(t) = \frac{e}{m(\omega^2 + i\gamma\omega)} \mathbf{E}(t)$. The displaced electrons contribute to the macroscopic polarization $\mathbf{P} = -ne\mathbf{x}$, which is given explicitly by

$$\mathbf{P} = -\frac{ne^2}{m(\omega^2 + i\gamma\omega)} \mathbf{E}. \quad (2.8)$$

Substituting Eq. 2.8 into the usual dielectric displacement \mathbf{D} of Maxwell's equations, ie $\mathbf{D} = \epsilon_0 \mathbf{E} + \mathbf{P}$, we have

$$\mathbf{D} = \epsilon_0 \left(1 - \frac{\omega_P^2}{\omega^2 + i\gamma\omega}\right) \mathbf{E}, \quad (2.9)$$

where $\omega_P = \sqrt{\frac{ne^2}{\epsilon_0 m}}$ is the plasma frequency of the free electron gas, n is the number of density of electrons and m is the effective mass of the electrons. Thus, the dielectric function of the free electron gas is given as

$$\epsilon = \left(1 - \frac{\omega_P^2}{\omega^2 + i\gamma\omega}\right). \quad (2.10)$$

The real and imaginary parts of the frequency dependent dielectric function ($\epsilon(\omega) = \epsilon_{re}(\omega) + i\epsilon_{im}(\omega)$) are given as: $\epsilon_{re}(\omega) = 1 - \frac{\omega_P^2 \tau^2}{1 + \omega^2 \tau^2}$ and $\epsilon_{im}(\omega) = \frac{\omega_P^2 \tau}{\omega(1 + \omega^2 \tau^2)}$, respectively. However, we note that at higher frequencies, where ω is close to ω_P , the product $\omega\tau \gg 1$ leading to negligible damping.

2.1.3 Scattering and absorption by small particles compared with the wavelength

Scattering is the process whereby electromagnetic waves are caused to radiate or deflect electromagnetic energy in all directions that are difficult to predict. Scattering

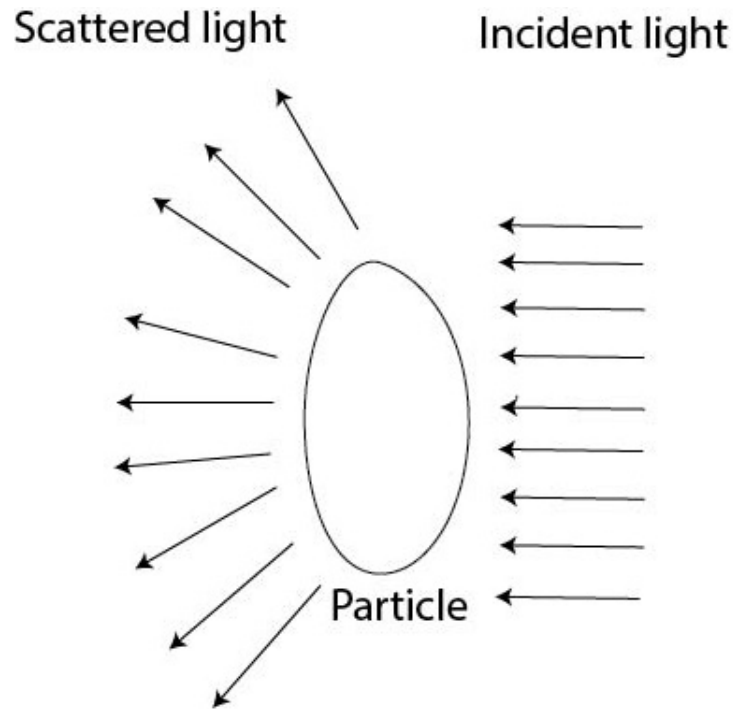


Figure 2.2: A diagram of light scattering by an obstacle (a particle).

of electromagnetic waves by any system is related to the heterogeneity of that system: heterogeneity on the molecular scale or on the scale of aggregations of many molecules [88]. Scattering of electromagnetic waves by any system is about the fields or the wave amplitude. On the other hand, absorption is the process whereby the excited electromagnetic wave of the incident electromagnetic field is transformed into other forms of energy (thermal energy, for example). Figure 2.2 shows the scattering of light in multiple directions by a particle. The physics of scattering is widely discussed in the literature [88, 89]. However, in this thesis, we will briefly discuss scattering by particles whose size is small compared to the wavelength of the incident electromagnetic wave. Of particular interest is the sphere and ellipsoid. The scattering by these type of particles is usually obtained from the power series expansion of the spherical Bessel functions [88]. In most cases, scattering of this nature is generally described in terms of Rayleigh scattering. It is important to note that in these types of small particle, the ratios of the amplitudes of the vibrations of the scattered and incident light is inversely proportional to the square of the wavelength

and the intensity of the light as the inverse fourth power. The contribution to the intensity of the light scattered by these small particles is given by [88]

$$I_{\parallel} = \frac{9|S_1|^2}{4k^2r^2} \cos^2 \theta, \quad (2.11)$$

$$I_{\perp} = \frac{9|S_1|^2}{4k^2r^2}, \quad (2.12)$$

$$I = \frac{1}{2}(I_{\parallel} + I_{\perp}), \quad (2.13)$$

where I_{\parallel} and I_{\perp} are for the incident light that is a plane wave and initially polarized parallel and perpendicular to the scattering plane, respectively and I is for unpolarized incident light. S_1 is a scattering coefficient, r is for the scattering distance, k is the wave-vector and θ is the angle in the scattering plane. The scattering plane is the x-z plane, as shown in Figure 2.1. The above equations assume an incident intensity normalised to 1. From the above scattering equations, one can see that the angular distribution of the scattered light depends on the polarization of the incident light (for example laser illumination). As light made of different polarization states is scattered differently by small particles, the scattered light will be partially polarized if the incident light is unpolarized, leading to an expression of the form:

$$\bar{P} = \frac{1 - \cos^2 \theta}{1 + \cos^2 \theta}, \quad (2.14)$$

where, \bar{P} is the degree of the polarization of the scattered light.

2.2 Electromagnetic theory of materials

This section mathematically describes the electromagnetic theory of materials, including metamaterials. In this work, we only consider linear materials. We start by looking at

the effective parameters and classification of materials. The properties of electromagnetic materials are normally determined by an electric permittivity ϵ , and a magnetic permeability μ where ϵ and μ describe the coupling of a material to the electric E and magnetic H field components of an electromagnetic wave, respectively. Thus, it is important to understand the physics of these two parameters and how they affect the properties of an electromagnetic material, both in wave propagation and coupling efficiency. Fortunately, Maxwell's equations can effectively describe ϵ and μ . We start our discussion with Maxwell's equations and follow the approach given in Maier [85].

The external charge and current ($\rho_{ext}, \mathbf{J}_{ext}$) densities are related to the internal charge and current densities (ρ, \mathbf{J}) by the expression: $\rho_{tot} = \rho_{ext} + \rho$ and $\mathbf{J}_{tot} = \mathbf{J}_{ext} + \mathbf{J}$. The external set drives the system, while the internal set responds to the external stimuli [85]. The Maxwell macroscopic equations are given by

$$\nabla \cdot \mathbf{D} = \rho_{ext} \quad (2.15a)$$

$$\nabla \cdot \mathbf{B} = 0 \quad (2.15b)$$

$$\nabla \times \mathbf{E} = -\frac{\partial \mathbf{B}}{\partial t} \quad (2.15c)$$

$$\nabla \times \mathbf{H} = \mathbf{J}_{ext} + \frac{\partial \mathbf{D}}{\partial t}, \quad (2.15d)$$

where \mathbf{D} is the electric displacement, \mathbf{B} is the magnetic inductance or the magnetic flux density, \mathbf{E} is the electric field and \mathbf{H} is the magnetic field. The polarization \mathbf{P} and the Magnetization \mathbf{M} in a dielectric material are related to the four macroscopic fields ($\mathbf{E}, \mathbf{D}, \mathbf{H}, \mathbf{B}$) as follows:

$$\mathbf{D} = \epsilon_0 \mathbf{E} + \mathbf{P} \quad (2.16a)$$

$$\mathbf{H} = \mu_0 \mathbf{B} - \mathbf{M}, \quad (2.16b)$$

where ϵ_0 and μ_0 are the permittivity and permeability of free space, respectively. Eqs. 2.15a - 2.15d are written in the time domain, while Eqs. 2.16a and 2.16b are the constitutive relations defined in frequency domain. In a dielectric material, the electric displacement is a vector field that accounts for the effect of free and bound charges within the material. Here, the electric polarization \mathbf{P} describes the electric dipole moment per unit volume inside the material, and \mathbf{P} is linked with the internal charge density of the material as: $\nabla \cdot \mathbf{P} = -\rho$. If we substitute Eq. 2.16a into Eq. 2.15a we find

$$\begin{aligned} \nabla \cdot (\epsilon_0 \mathbf{E} + \mathbf{P}) &= \rho_{ext} \\ \epsilon_0 \nabla \cdot \mathbf{E} + \nabla \cdot \mathbf{P} &= \rho_{ext} \end{aligned}$$

$$\text{but, } \nabla \cdot \mathbf{P} = -\rho, \text{ then using this in the above, we have} \quad (2.17)$$

$$\begin{aligned} \epsilon_0 \nabla \cdot \mathbf{E} &= \rho_{ext} + \rho \\ \nabla \cdot \mathbf{E} &= \frac{\rho_{tot}}{\epsilon_0} \end{aligned}$$

Here, Eq. 2.17 is the general form of Maxwell Eq. 2.15a. ρ_{tot} represents the total charge density in the dielectric material. The advantage of this approach is that the macroscopic electric field in the dielectric material includes all polarization effects: In other words, both the external and the induced fields are absorbed into it. The polarization effects come from the dipoles responding to the external electric field and the produced fields are the induced fields. All the induced fields are combined into the field vector. Hence, we have the external field and the induced field. The magnetization can also be obtained in a similar fashion using Eqs. 2.16b and 2.15b. However, for a linear, isotropic and non-magnetic dielectric material, \mathbf{D} and \mathbf{B} can be written as:

$$\mathbf{D} = \epsilon_0 \epsilon \mathbf{E} \quad (2.18a)$$

$$\mathbf{B} = \mu_0 \mu \mathbf{H}, \quad (2.18b)$$

where ϵ is the relative permittivity and μ is the relative permeability (magnetic permeability) of the medium. In the linear regime, \mathbf{D} and \mathbf{E} can also be defined using the electric susceptibility χ , which describes the linear relationship between the polarization and the electric field

$$\mathbf{P} = \epsilon_0 \chi \mathbf{E}. \quad (2.19)$$

Since the response of a dielectric material in an electromagnetic field depends on the optical angular frequency, ω , and on the wavevector, \mathbf{K} , in the frequency domain of the electromagnetic field, we can rewrite Eq. 2.18a as

$$\mathbf{D}(\mathbf{K}, \omega) = \epsilon_0 \epsilon(\mathbf{K}, \omega) \mathbf{E}(\mathbf{K}, \omega) \quad (2.20a)$$

$$\mathbf{J}(\mathbf{K}, \omega) = \sigma(\mathbf{K}, \omega) \mathbf{E}(\mathbf{K}, \omega), \quad (2.20b)$$

where σ is the conductivity of the dielectric material. $\epsilon(\mathbf{K}, \omega)$ and $\mu(\mathbf{K}, \omega)$ can be written as ω as $\epsilon(\mathbf{K}, \omega) = \epsilon_1(\mathbf{K}, \omega) + i\epsilon_2(\mathbf{K}, \omega)$ and $\mu(\mathbf{K}, \omega) = \mu_1(\mathbf{K}, \omega) + i\mu_2(\mathbf{K}, \omega)$, respectively. Here, $\epsilon_1(\mathbf{K}, \omega)$ and $\mu_1(\mathbf{K}, \omega)$ is the real permittivity and permeability, and $\epsilon_2(\mathbf{K}, \omega)$ and $\mu_2(\mathbf{K}, \omega)$ is the imaginary permittivity and permeability of the dielectric material, respectively. The value of $\epsilon(\mathbf{K}, \omega)$ can be experimentally determined at optical frequency through the determination of the refractive index of the medium, defined as $\eta = \sqrt{\epsilon\mu}$. Since at optical frequencies, $\mu = 1$, η is expressed explicitly as $\eta = \sqrt{\epsilon}$. The wavenumber can be expressed as: $|\mathbf{K}| = \frac{\omega}{c_n} \approx \omega \sqrt{\epsilon\mu}$, since $c_n = \frac{c}{\eta}$ and $c = \frac{1}{\sqrt{\epsilon_0\mu_0}}$ where c is the speed of light in a vacuum. If we assume that the charges transit in the same direction as the electric field, the Lorentz model that describes a temporal response of a component of the

polarization field of the medium to the same component of the electric field is given as:

$$\frac{d^2}{dt^2}P_i + \Gamma_L \frac{d}{dt}P_i + \omega_0^2 P_i = \epsilon_0 \chi_L E_i, \quad (2.21)$$

where the second-order differential term on the left accounts for the acceleration of the charges, the first-order differential term accounts for the damping mechanisms of the system with damping coefficient Γ_L , and the ω_0^2 accounts for the restoring forces with the characteristic frequency $f_0 = \omega_0/2\pi$. The charges which experience a driving force manifest a coupling coefficient χ_L , generally known as the electric susceptibility. In the frequency domain, assuming a time dependence $\exp(+j\omega t)$, the response of the polarization field component is

$$P_i(\omega) = \frac{\chi_L}{-\omega^2 + j\Gamma_L\omega + \omega_0^2} \epsilon_0 E_i(\omega). \quad (2.22)$$

The polarization and the electric field are linked with the electric susceptibility, using Eqs. 2.19 and 2.22, we have

$$\chi_{e,lorentz} = \frac{P_i(\omega)}{\epsilon_0 E_i(\omega)} = \frac{\chi_L}{-\omega^2 + j\Gamma_L\omega + \omega_0^2}, \quad (2.23)$$

where ϵ is directly obtained from the relation: $\epsilon_{lorentz}(\omega) = \epsilon_0[1 + \chi_{e,lorentz}(\omega)]$. Using Eqs. 2.16a and 2.18a, when the second-order differential acceleration term of Eq. 2.21 is small or negligible, we have the Debye model which is given by

$$\Gamma_D \frac{d}{dt}P_i + \omega_0^2 P_i = \epsilon_0 \chi_D E_i, \quad (2.24)$$

with

$$\chi_{e,Debye}(\omega) = \frac{\chi_D}{j\Gamma_D\omega + \omega_0^2}. \quad (2.25)$$

When the restoring force is small or negligible, we have the Drude model for the dielectric

material defined by

$$\frac{d^2}{dt^2}P_i + \Gamma_D \frac{d}{dt}P_i = \epsilon_0 \chi_D E_i, \quad (2.26)$$

with

$$\chi_{e,Drude}(\omega) = \frac{\chi_D}{-\omega^2 + j\Gamma_D \omega}. \quad (2.27)$$

In most cases, the coupling efficiency in the Drude model is represented by the plasma frequency $\chi_D = \omega_P^2$, where $\omega_P^2 = \frac{n e^2}{\epsilon_0 m}$ with n as the number of electrons per unit volume and m as the mass of the charge. It should be noted that the Drude and Lorentz models can give negative ϵ if we assume the coupling efficiency to be positive. For example, in the case of the Lorentz model, the real part of χ_L and ϵ can become negative in a narrow frequency region immediately above the resonance [19]. Following a similar derivation, the equations for the magnetic field components of the dielectric material M_i and the magnetic susceptibility χ_m are obtained from the P_i and χ_e expressions with the replacements of E_i by H_i and P_i/ϵ_0 by M_i . The dielectric permeability is given as: $\mu = \mu_0[1 + \chi_m]$. Generally, the Lorentz model for polarization and magnetization of a medium in terms of the ϵ and μ is given by

$$\epsilon(\omega) = 1 + \frac{\omega_P^2}{(\omega_0^2 - \omega^2 - j\Gamma_e \omega)}, \quad (2.28a)$$

and

$$\mu(\omega) = 1 + \frac{\omega_{m,p}^2}{(\omega_{m,0}^2 - \omega^2 - j\Gamma_m \omega)}, \quad (2.28b)$$

respectively, where $\omega_{m,p}$ is the magnetic plasma frequency and $\omega_{m,0}$ is the magnetic resonance frequency.

Metamaterials are usually classified based on ϵ and μ because these two parameters define the dispersion relation ($K = \frac{\omega}{c} = \omega \sqrt{\epsilon \mu}$) of a medium. In a similar fashion to conventional materials, the electromagnetic responses of a metamaterial to external fields can be homogenized and are described using effective parameters including ϵ and μ . Metamaterials open up a new frontier to realize all possible material properties by designing

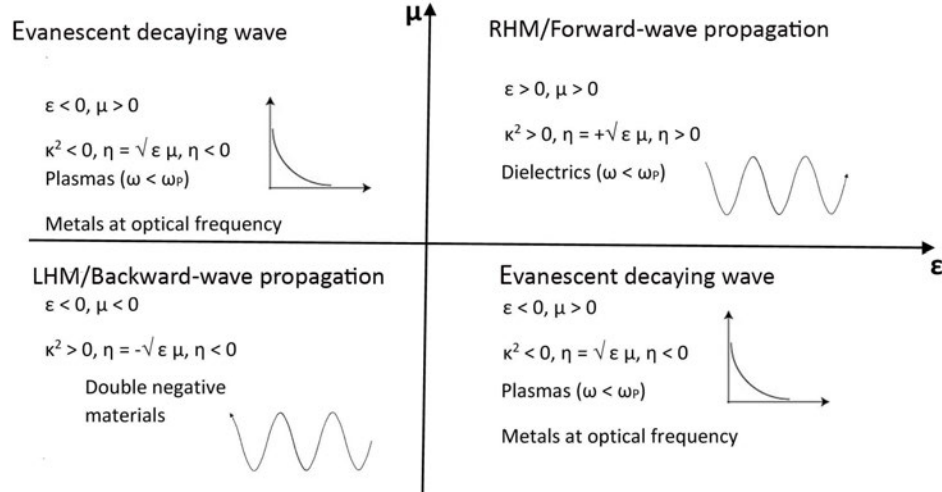


Figure 2.3: Properties of metamaterials based on ϵ and μ .

different cellular architectures and using different substrate materials. Figure 2.3 describes the classification and properties of metamaterials in terms of ϵ and μ . The first quadrant ($\epsilon < 0$ and $\mu > 0$) represents electric plasmas, which support evanescent waves. The second quadrant ($\epsilon > 0$ and $\mu > 0$) denotes right-handed materials (RHM), which support forward propagating waves. This can be seen from Maxwell's equations where \mathbf{E} , \mathbf{H} , and \mathbf{K} form a right-handed system. The third quadrant ($\epsilon < 0$ and $\mu < 0$) is the unusual

well-known left-handed materials (LHM), supporting backward propagating waves. In LHM, the \mathbf{E} , \mathbf{H} , and \mathbf{K} form a left-handed system. The consequence of materials having $\epsilon < 0$ and $\mu < 0$ is that the propagation of the electromagnetic wave is in an opposite direction to the flow of energy. The fourth quadrant ($\epsilon > 0$ and $\mu < 0$) represents magnetic plasmas, which support evanescent waves.

2.2.1 Fabrication techniques

The fabrication of metamaterials requires that the size of the unit cells should have a size that is smaller than the wavelength under consideration, which is of the order a hundred nanometers for visible light. Theoretical studies, such as the testing and design of meta-

materials should not be the only research theme, the fabrication of metamaterials should also be given optimal research attention. If not, the idea of producing a metamaterial in the real world will always remain a dream. However, due to recent advances in nanofabrication techniques, which were developed over the past 20 years, it has become possible to fabricate a metamaterial with the size of the unit cells smaller than the wavelength of interest. Hence, undertaking such a task for optical frequencies requires more sophisticated techniques, such as electron-beam lithography, focused ion beam milling, nanoprint lithography, interference optical lithography, direct laser writing, and many more [90]. These are the commonly used fabrication techniques in producing 2-D and 3-D metamaterials. Although, Veselago in 1967 [6] mentioned in his paper that it is possible to obtain the combination of $\epsilon < 0$ and $\mu < 0$ leading to a negative refractive index, $\eta < 0$, his idea remained unrealized for years because no naturally occurring materials that have simultaneous negative ϵ and μ at optical frequencies exist. While there are natural materials with $\epsilon < 0$, such as silver, gold, ferroelectric materials (e.g barium titanate), and other metals up to the visible part of the electromagnetic spectrum, the case is different with $\mu < 0$, as there are no naturally existing magnetic materials with $\mu < 0$ at optical frequencies. However, with an artificial structure where the unit cells are designed to simultaneously have ϵ and μ responses, one can overcome the limitations imposed on natural materials by their unit cells. To create a metamaterial at optical frequencies, one needs to deal with small periodicities (about 300 nm and less) and tiny feature sizes (about 30 nm) to ensure an effective-medium-like behavior [90]. Despite the fact that photolithography is the dominant process used for microfabrication in the integrated circuit industry, the small periodicities and tiny feature sizes in most optical metamaterials still exceed the capability of the start-of-the-art, 193 nm photolithographic technology, where deep ultraviolet light with $\lambda = 193$ nm is used for exposure [1]. A brief review on metamaterial fabrication techniques is now given, a more detailed review can be found elsewhere [1, 90]. The techniques are as follows.

Electron-beam lithography: Due to the fact that the tiny feature sizes for metamaterials are smaller than the resolution of state-of-the-art photolithography, most reported 2-D metamaterial layers are usually fabricated using electron-beam lithography (EBL). In fact, some of the notable metamaterials with distinctive features that have given remarkable results in this noble field were achieved using EBL. For example, the EBL technique has been used to fabricate optical metamaterials with a negative refractive index [91], which to most researchers is considered to be the first experimentally obtained optical negative metamaterial [90]. Other metamaterials made using EBL include those with a magnetic response [92] and a giant chirality [93]. EBL is the process whereby electron beams are scanned serially on a surface covered with an electron-sensitive film to generate periodic patterns. The EBL technique offers sub-wavelength resolution and flexibility because the width of the beam is of the order of nanometers, resulting in a high nanoscale resolution of the technique. Recently fabricated negative-index metamaterials using EBL showed improved optical performance in terms of low loss. In 2006, the Karlsruhe group in collaboration with Iowa State University engineered negative-refractive-index metamaterials (NIMs) in the optical range at a wavelength of about $1.4 \mu\text{m}$ (telecommunication wavelength) [94]. In 2007, the negative refractive index was pushed into the visible regime of the electromagnetic spectrum at a wavelength of 780 nm [95].

Figure 2.4 shows a scanning electron microscope (SEM) image of a NIM sample based on the fishnet geometry suggested in Ref. [32] using EBL. The structure is made up of two layers of silver separated by a 10 nm thick layer of aluminium which maintains the integrity of the structure during a lift-off process. Fabricating optical metamaterials by EBL is cost intensive and time consuming because of the required tiny feature sizes of the unit cells or meta atoms. Since only small areas of the order of $100 \mu\text{m}$ -by- $100 \mu\text{m}$ can normally be organized within reasonable time and at reasonable cost, EBL is not seen as a good candidate for large-scale metamaterial fabrication required by applications, where many square centimeters may have to be nanopatterned [90]. Despite these challenges,

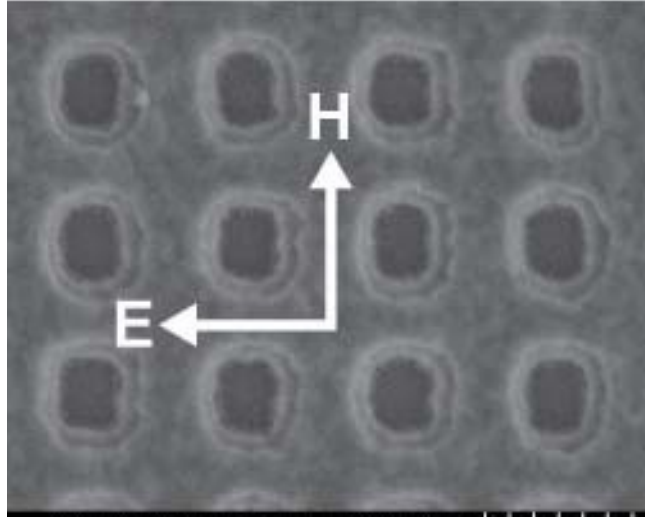


Figure 2.4: Scanning electron microscope image of a NIM sample based on the fishnet geometry suggested in [32] fabricated using EBL, followed by electron-beam evaporation and lift-off. The structure is made up of two layers of silver separated by a 10 nm thick layer of aluminium which operates at a wavelength of 813 nm. Taken from [30, 31].

EBL is the preferred method for fabricating 2-D optical metamaterials with metal-dielectric unit structures because of its subwavelength resolution and flexibility, and is normally referred to as the standard method.

Focused-ion beam lithography and milling: Focused-ion beam (FIB) is a technique normally used in the semiconductor industry, materials science and biological fields for site-specific analysis, deposition, and ablation of materials. FIB has also gained wide interest in the field of metamaterials as an alternative fabrication method for rapid prototype of metamaterials due to its ability to produce high aspect ratio structures, and quick processing time. FIB uses a finely focused ion beam (usually Gallium) to sputter atoms from a sample surface, or uses a focused Gallium ion beam to pattern a design. FIB is often used as a micro-machining tool to machine materials at the micro- and nanoscale because the accelerated ions in FIB have sufficient energy to sputter the atoms from the surface or create a pattern of Gallium atoms into the top few nanometers of the surface. The focused spot size of the ion beam is around 10 nm, which make FIB an alternative technique for the fabrication of photonic metamaterials [1]. One of the advantages of FIB

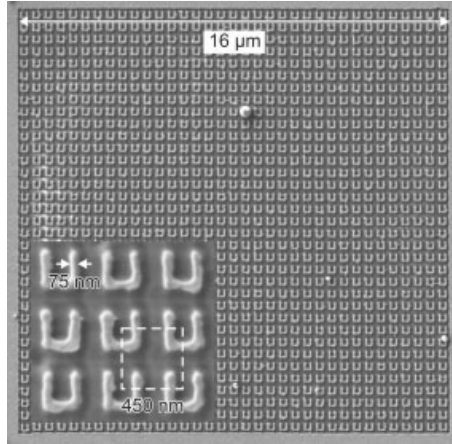


Figure 2.5: SEM image of a $16 \mu\text{m} \times 16 \mu\text{m}$ array of SRRs fabricated using FIB writing, with the inset showing the magnified image of the magnetic metamaterial. Taken from [96].

over EBL is the rapid operation time to pattern a design. In FIB lithography the Gallium ion beam directly cuts pre-deposited layers into the desired nanostructures, unlike EBL that can only scan the layer serially. The FIB lithography technique has been used to fabricate split-ring resonators (SRRs) to give a metamaterial with negative permeability. For example, Enkrich et al. [96] used FIB to fabricate a near-infrared magnetic metamaterial from a split-ring resonator, scaled down to a $1.5 \mu\text{m}$ resonance wavelength and 35 nm minimum feature size. The authors successfully fabricated the complete structure of the magnetic metamaterial via FIB writing in times as short as 20 minutes (rapid prototyping). Figure 2.5 shows a SEM image of a $16 \mu\text{m} \times 16 \mu\text{m}$ array of SRRs fabricated using FIB writing [96]. FIB lithography or milling has also been used to fabricate Mie resonance-based dielectric (MRD) metamaterials where the material was milled by blasting its surface with accelerated Gallium atoms [97]. However, the inherent risk with this technique is that the removed material may contaminate the finished product, especially when making high aspect ratio structures [98]. In this sense, the aspect ratio is limited by re-deposition of the milled material.

Interference Lithography: One type of optical lithography (OP) is called interference lithography (IF). Optical lithography is the method of choice used by the integrated circuit (IC) industry due to its ability to mass produce samples. IF offers new ways of increasing its resolution, for example, by using immersion techniques that meet the industry 45 nm half-pitch-node requirements [99]. Interference lithography is widely used for the fabrication of arrays of samples for the nanotechnology industry. This technique is achieved based on the superposition of two or more coherent optical beams forming a standing wave. The large-scale fabrication, low cost, large area (usually up to cm^2) makes IF a very powerful tool for fabricating metamaterial samples. Other advantages are: a high structural uniformity combined when its resolution is approaching the 20 nm scale [99]. Because of its high resolution and simplicity, IF has been used to fabricate different metamaterial samples including: one dimensional metallic structures [100], magnetic metamaterials [100], negative-index metamaterials [101, 102, 103]. It is interesting to note that IF can be used to fabricate 3D metamaterial structures by piling up 2D layers to make 3D layers due to its simplicity and robustness in making 2D metamaterial structures [90].

Nanoimprint lithography: Nanoimprint lithography (NIL) patterns a design by the mechanical deformation of the resist or surface of the sample by means of a stamp. Unlike in most lithography methods where an electron- or photo-induced process is used to pattern a design, in NIL, a stamp is used. NIL is another promising method for the fabrication of production-compatible, large area, high-quality optical metamaterials at low processing cost and time [104]. One of the greatest strengths of NIL is due to the fact that its resolution is not limited by the wavelength of the light source since the smallest attainable size of the unit cells are fabricated by the stamp. This technique also offers parallel processing and high throughput. NIL is well suited for large scale-production of optical metamaterials, providing wafer-scale processing using standard clean room procedures combined with simplicity and low cost [90]. It is interesting to note that different

metamaterial structures have been fabricated successfully using NIL. Such as NIMs based on fishnet arrays of metallic dielectric metals operating at near infrared frequencies [105] and at mid-infrared frequencies [106]. Others are chiral and planer metamaterials for the study and application of novel polarization effects [107], and for creating metallic 2D structures [108, 109]. However, NIL has some technical challenges in fabricating the stamp, and cannot be directly applied to the fabrication of optical NIMs due to specific requirements on geometry and materials [90].

Fabrication of metamaterials in 3D: We briefly mention the fabrication of metamaterials in 3D. A detailed review on 3D metamaterial fabrication techniques is found in [90, 98]. For low-loss metamaterials to realize their full potential, new ways of designing 3D structures have to be developed. Recently, some 3D fabrication techniques have been developed, and researchers are looking into more new ways for fabricating 3D structures. Techniques used in fabricating 3D structures include making multiple layers, two-photon-photopolymerization (TPP), direct-electron beam writing (EBW), focused-ion beam chemical vapour deposition (FIB-CVD) 3D structures by nanoimprint, self assembly, and many more. Some of these techniques combine two or more of the techniques used in fabricating 2D materials. Multiple layers of up to three functional layers of structures were fabricated by the Karlsruhe group [110], and silver-based three dimensional structures were fabricated using EBL, metal and dielectric deposition and a lift-off procedure [111, 94]. Another approach is a layer-by-layer technique to realize a stack of optical NIMs in a four layer SRR structure [112].

2.3 Quantum mechanics

2.3.1 Vector Spaces

Vector spaces are the basic elements of linear algebra. In quantum mechanics, a vector space can be represented as C^n , comprised of the complex numbers (x_1, x_2, \dots, x_n) . The elements of a vector space are called vectors which can be written in a column form as

$$\begin{bmatrix} x_1 \\ x_2 \\ \vdots \\ x_n \end{bmatrix} \quad (2.29)$$

In quantum mechanics the notation of such a vector is $|\psi\rangle$ and the way of carrying out vector addition and multiplication is the same as in normal linear algebra and therefore will not be treated here.

2.3.2 Linear Operators and Matrices

A linear operator between two vector spaces M and N is defined to be any function $L: M \mapsto N$ given its inputs are linear

$$L\left(\sum_i l_i |m_i\rangle\right) = \sum_i l_i L(|m_i\rangle). \quad (2.30)$$

The above equation is often written as $L|m\rangle$. An example of a type of linear operator on a vector space M is the identity operator $\mathbf{1}_M$ defined by the expression $\mathbf{1}_M|m\rangle \equiv |m\rangle$. Note that, in this thesis, the identity operator will be denoted as $\mathbf{1}$ for simplicity.

2.3.3 Pauli Matrices

The Pauli matrices are a very important set of matrices in quantum mechanics and information science. They are 2 by 2 complex matrices that operate on quantum bits (qubits) which are states from the vector space C^2 . The Pauli matrices are Hermitian and unitary.

$$\begin{aligned} \sigma_0 \equiv \mathbb{I} &= \begin{bmatrix} 1 & 0 \\ 0 & 1 \end{bmatrix} & \sigma_x \equiv X &= \begin{bmatrix} 0 & 1 \\ 1 & 0 \end{bmatrix} \\ \sigma_y \equiv Y &= \begin{bmatrix} 0 & -i \\ i & 0 \end{bmatrix} & \sigma_z \equiv Z &= \begin{bmatrix} 1 & 0 \\ 0 & -1 \end{bmatrix} \end{aligned} \tag{2.31}$$

Here, the identity matrix $\mathbb{1}$ is included. The Pauli matrices form a basis for the vector space of 2 by 2 Hermitian matrices when multiplied by real coefficients. Hermitian operators denote an observable. Hence, the Pauli matrices span the space of observables of the 2-dimensional complex Hilbert space.

2.3.4 Inner products

An inner product is a function which takes two vectors $|m\rangle$ and $|n\rangle$ from a vector space and produces a complex number as an output [74]. In other words, an inner product is an operator that combines two vectors to produce a scalar. In quantum mechanics, the notation of an inner product ($|m\rangle, |n\rangle$) is $\langle m|n\rangle$, where $|m\rangle$ and $|n\rangle$ are the vectors, and the notation $\langle m|$ corresponds to the dual vector for the vector $|m\rangle$. For example, if we take vectors $|m\rangle = (x_1, x_2, x_3)$ and $|n\rangle = (u_1, u_2, u_3)$ we can obtain an inner product by

multiplying both vectors as follows

$$\langle m|n\rangle = \begin{pmatrix} x_1^* & x_2^* & x_3^* \end{pmatrix} \begin{pmatrix} u_1 \\ u_2 \\ u_3 \end{pmatrix} = x_1^*u_1 + x_2^*u_2 + x_3^*u_3 \quad (2.32)$$

Thus, an inner product gives a scalar. In quantum mechanics, vectors $|m\rangle$ and $|n\rangle$ are orthogonal if their inner product is zero. The norm of a vector $|m\rangle$ is defined by

$$\| |m\rangle \| \equiv \sqrt{\langle m|m\rangle}. \quad (2.33)$$

Thus, we call the vector $|m\rangle$ a unit vector if $\| |m\rangle \| = 1$. In this case the vector $|m\rangle$ is normalised.

2.3.5 Eigenvectors and Eigenvalues

An eigenvector of a linear operator L on a vector space is a non-zero vector $|m\rangle$ such that $L|m\rangle = m|m\rangle$, where m is a complex number known as the eigenvalue of L corresponding to $|m\rangle$ [74]. In linear algebra, eigenvectors and eigenvalues are obtained mathematically through the characteristic function given as

$$c(\lambda) \equiv \det |L - \lambda I|, \quad (2.34)$$

\det is the determinant function for matrices. The solutions of Eq. 2.34 for $c(\lambda) = 0$ are the eigenvalues of the operator L [74]. Operator L on a vector space M can be diagonally represented as

$$L = \sum_m \lambda_m |m\rangle \langle m|, \quad (2.35)$$

where the vectors $|m\rangle$ form an orthonormal set of eigenvectors for L , with corresponding eigenvalues λ_m .

2.3.6 Adjoint and Hermitian Operators

An adjoint or Hermitian conjugate operator, L^\dagger can be defined as the complex conjugate transpose of a linear operator, L , acting on a Hilbert space, M , in such a manner that all vectors $|m\rangle, |n\rangle \in M$,

$$(|m\rangle, L|n\rangle) = (L^\dagger|m\rangle, |n\rangle). \quad (2.36)$$

For a vector $|m\rangle$, its complex conjugate transpose $|m\rangle^\dagger$ is equivalent to $\langle m|$. Using $|m\rangle^\dagger \equiv \langle m|$, we have $(L|m\rangle)^\dagger = \langle m|L$.

2.3.7 Commutator and Anti-commutator

This is another important feature of quantum mechanics. Some operators commute while others do not. The commutator between two operators L and O is defined by

$$[L, O] \equiv LO - OL. \quad (2.37)$$

This simply means if $[L, O] = 0$, then $LO = OL$. If the operators satisfy this condition, then we can say that operator L commutes with operator O . In a similar fashion, the anti-commutator between operators L and O can be defined by

$$\{L, O\} \equiv LO + OL. \quad (2.38)$$

In this case we say L anti-commutes with O if $\{L, O\} = 0$.

2.3.8 Quantum measurements

This section briefly deals with the measurement of a physical quantum system. In quantum mechanics, there are two different types of quantum systems: closed and open quantum systems. Closed quantum systems evolve according to the unitary evolution ($|\psi'\rangle = U|\psi\rangle$), where U is a unitary operator acting on the closed system $|\psi\rangle$. A closed quantum system

is a system that does not interact with the environment. However, in a real sense, there is no perfect closed system except when taking the entire universe. Another type of a quantum system is the open quantum system, whereby a quantum system interacts with its environment. As a result of the interaction, the system is no longer closed, and therefore, not necessarily subject to unitary evolution. This process also describes a scenario where an experimentalist observes the interaction of a physical system with its environment in the form of a quantum measurement.

Quantum measurements are described by a collection of measurement operators M_m . These are operators acting on the state space of the system being measured. The subscript m refers to the measurement outcomes that may occur in the experiment. If the state of the quantum system immediately before the measurement is $|\psi\rangle$, then the probability outcome is

$$p(m) = \langle \psi | M_m^\dagger M_m | \psi \rangle, \quad (2.39)$$

and the post-measurement state of the system is given by [74]

$$\frac{M_m |\psi\rangle}{\sqrt{\langle \psi | M_m^\dagger M_m | \psi \rangle}}. \quad (2.40)$$

Eqs. 2.39 and 2.40 ensure that quantum measurements satisfy the completeness condition

$$\sum M_m^\dagger M_m = \mathbb{I}, \quad (2.41)$$

and that the probability of measurement outcomes sum to 1. That is

$$\sum p(m) = \sum_m \langle \psi | M_m^\dagger M_m | \psi \rangle = 1. \quad (2.42)$$

In quantum mechanics, all real physical systems must satisfy Eq. 2.42. Examples of quantum measurements on a qubit use the computational basis ($M_0 = |0\rangle\langle 0|$, $M_1 = |1\rangle\langle 1|$), and

the polarisation basis ($M_H = |H\rangle\langle H|$, $M_V = |V\rangle\langle V|$), where subscripts H and V represent horizontal and vertical polarisation states of photons. Both bases represent the same thing, but with a different notation. The theorist prefers the computational basis while the experimentalist prefers the polarisation basis. A particular class of quantum measurements that is commonly used in quantum mechanics is the projective measurement. In this type of measurement, a given quantum state is projected and measured.

2.3.8.1 Projective measurements

Projective measurements are described by an observable, M , a Hermitian operator on the Hilbert space (state space) of the system being observed [74]. The observable is spectrally decomposed using

$$M = \sum_m m P_m \quad (2.43)$$

where P_m is the projector on the eigenspace with eigenvalue m of the observable. The probability of obtaining result m is

$$p(m) = \langle \psi_m | P_m | \psi_m \rangle, \quad (2.44)$$

and the post-measurement state of the system is

$$\frac{P_m | \psi_m \rangle}{\sqrt{p(m)}}. \quad (2.45)$$

The projectors are self-adjoint operators: $P_m^\dagger \equiv P_m$ because $(| \psi_m \rangle \langle \psi_m |)^\dagger = | \psi_m \rangle \langle \psi_m |$. Projective measurements satisfy the completeness relation, and the condition that measurement operators M_m are Hermitian and orthogonal ($M_m^\dagger M_m = \delta_{m,m} M_m$). Thus, $M_m^\dagger M_m = M_m = P_m$. The average value of the observable is given by [74]

$$\langle M \rangle = \langle \psi | M | \psi \rangle. \quad (2.46)$$

From eq. 2.46, we can obtain the standard deviation associated with the observable

$$\Delta(M) = \sqrt{\langle (M - \langle M \rangle)^2 \rangle} = \sqrt{\langle M^2 \rangle - \langle M \rangle^2}. \quad (2.47)$$

2.3.9 Density operator

Another method of describing quantum states other than the state vector approach is by using the density operator or matrix. The density operator method provides a better way of describing quantum systems whose states are not well known. For example, if we have a quantum system in one of the states $|\psi_k\rangle$, where k is an index, with probabilities p_k respectively, then the density operator for the system is given by

$$\rho = \sum_k p_k |\psi_k\rangle \langle \psi_k| \quad (2.48)$$

Consider the evolution of a closed system that is described by a unitary operator U that has an initial state $|\psi_k\rangle$ with probability p_k and a final state $U|\psi_k\rangle$ after the evolution has occurred. The density operator for the system is given by

$$\rho = \sum_k p_k |\psi_k\rangle \langle \psi_k| \xrightarrow{U} \sum_k p_k U|\psi_k\rangle \langle \psi_k| U^\dagger = U\rho U^\dagger \quad (2.49)$$

Quantum measurements can also be described effectively using the density operator approach. For example, if we carry out a measurement described by operators M_m on a system that has an initial state $|\psi_k\rangle$. The probability of obtaining result m is

$$p(m|k) = \langle \psi_k | M_m^\dagger M_m | \psi_k \rangle = \text{tr}(M_m^\dagger M_m |\psi_k\rangle \langle \psi_k|), \quad (2.50)$$

Here, tr is the trace of a matrix. Therefore, the probability $p(m)$ of obtaining result m is

$$p(m) = \sum_k p(m|k)p_k = \sum_k p_k \text{tr}(M_m^\dagger M_m |\psi_k\rangle \langle \psi_k|) = \text{tr}(M_m^\dagger M_m \sum_k p_k |\psi_k\rangle \langle \psi_k|) = \text{tr}(M_m^\dagger M_m \rho). \quad (2.51)$$

The density operator ρ_m of the system corresponding to the post-measurement with respective probabilities $p(k|m)$ is given by

$$\rho_m = \sum_k p(k|m) |\psi_k^m\rangle \langle \psi_k^m| = \sum_k p(k|m) \frac{M_m |\psi_k\rangle \langle \psi_k| M_m^\dagger}{\langle \psi_k| M_m^\dagger M_m |\psi_k\rangle}. \quad (2.52)$$

Using $p(k|m) = p(m, k)/p(m) = p(m|k)p_k/p(m)$ (Baye's probability theory), we have

$$\rho_m = \sum_k p_k \frac{M_m |\psi_k\rangle \langle \psi_k| M_m^\dagger}{\text{tr}(M_m^\dagger M_m \rho)} = \frac{M_m \rho M_m^\dagger}{\text{tr}(M_m^\dagger M_m \rho)}, \quad (2.53)$$

where $|\psi_k^m\rangle = \frac{M_m^\dagger |\psi_k\rangle}{\sqrt{\langle \psi_k| M_m^\dagger M_m |\psi_k\rangle}}$ is the state of the system after obtaining result m .

2.3.10 Quantum State Tomography

Quantum state tomography (QST) is the process of reconstructing the quantum state (density matrix) for a source of a quantum system via direct measurements on identical copies of the quantum state. In other words, QST can be defined as the process that characterizes the complete quantum state of a particle through a series of measurements in different bases [113]. Unlike in classical computing or classical physics where characterisation of a physical system is done by carrying out a series of measurements on the same system, in quantum mechanics, measuring a single quantum system disturbs its state, often making further measurements lack useful information. Hence, quantum tomography is carried out on a number of identical copies of the same unknown state, and as such cannot be successfully applied to a single unknown state.

Before any quantum state can be analysed, it is important to understand the state representation. The reconstruction of an unknown quantum state is made easier by a specific state parameterization. A single qubit in a pure state can be represented as: $|\psi\rangle = \alpha|0\rangle + \beta|1\rangle$ in the computational basis, whereas for a mixed state, it is best described by a density operator or matrix formulation $\rho = \sum_k p_k |\psi_k\rangle \langle\psi_k|$. This simply means that mixed states may be described by a probabilistically weighted incoherent sum [113].

In this thesis, we will use QST with single photons encoded into the electric field polarization of photons. For single photons, the quantum system has two levels; for example, horizontal ($|H\rangle \equiv |0\rangle$) and vertical ($|V\rangle \equiv |1\rangle$). The remaining other pure polarization states, the diagonal ($|+\rangle = (|H\rangle + |V\rangle)/\sqrt{2}$), antidiagonal ($|-\rangle = (|H\rangle - |V\rangle)/\sqrt{2}$), left-circular ($|L\rangle = (|H\rangle + i|V\rangle)/\sqrt{2}$), and right-circular ($|R\rangle = (|H\rangle - i|V\rangle)/\sqrt{2}$) are constructed from a coherent superposition of $|H\rangle$ and $|V\rangle$ states.

A single qubit density matrix can then be represented by three Stokes parameters $\{S_1, S_2, S_3\}$:

$$\rho = \frac{1}{2} \sum_{k=0}^3 S_k \sigma_k, \quad (2.54)$$

where σ_k corresponds to the usual Pauli matrices ($\sigma_0, \sigma_1, \sigma_2, \sigma_3$), and the values of S_k can be obtained by [74]

$$S_k = \text{tr}(\sigma_k \rho), \quad (2.55)$$

where for pure states, $\sum_{k=1}^3 S_k^2 = 1$; for mixed states, $\sum_{k=1}^3 S_k^2 < 1$; and for completely mixed state, $\sum_{k=1}^3 S_k^2 = 0$. As a result of normalization, $S_0 = 1$. These four parameters

correspond to the outcome of particular pairs of projective measurements [113]

$$\begin{aligned}
 S_0 &= P_{|H\rangle} + P_{|V\rangle} \\
 S_1 &= P_{|+\rangle} - P_{|-\rangle} \\
 S_2 &= P_{|L\rangle} - P_{|R\rangle} \\
 S_3 &= P_{|H\rangle} - P_{|V\rangle}
 \end{aligned} \tag{2.56}$$

where $P_{|\psi\rangle}$ is the probability to measure state $|\psi\rangle$. Thus, the probability of projecting a given state ρ into the state $|\psi\rangle$ is: $P_{|\psi\rangle} = \langle\psi|\rho|\psi\rangle = \text{tr}(|\psi\rangle\langle\psi|\rho)$. In Eq. 2.56, the S_k are defined with respect to the three states, $|\psi_k\rangle$:

$$\begin{aligned}
 |\psi_1\rangle &= \frac{1}{\sqrt{2}}(|H\rangle + |V\rangle) \\
 |\psi_2\rangle &= \frac{1}{\sqrt{2}}(|H\rangle + i|V\rangle) \\
 |\psi_3\rangle &= |H\rangle,
 \end{aligned} \tag{2.57}$$

and their orthogonal counterpart, $|\psi_k^\perp\rangle$.

2.3.11 Quantum Process Tomography

Quantum process tomography is the process of characterising the dynamics of a quantum system. It can also be defined as a procedure for characterising a quantum process by probing with known quantum states. In classical computing, this is known as system identification [74]. For example, if we consider a physical process acting on a quantum system ρ that is described by a channel ξ

$$\xi(\rho) = \sum_k E_k \rho E_k^\dagger, \quad \sum_k E_k^\dagger E_k = \mathbb{1} \tag{2.58}$$

Eq. 2.58 is an example of a Kraus decomposition. In order to know the form of this Kraus decomposition from observables obtained from an experiment, and thus, find the E_k 's, we

need to use a fixed set of operators \hat{E}_k which form a basis for the set of operators [74]

$$E_k = \sum_m \text{tr}(\hat{E}_m^\dagger E_k) \hat{E}_m = \sum_m e_{km} \hat{E}_m. \quad (2.59)$$

Eq. 2.58 then gives

$$\xi(\rho) = \sum_{mn} \hat{E}_m \rho \hat{E}_n^\dagger \chi_{mn}, \quad (2.60)$$

where $\chi_{mn} = \sum_k e_{km} e_{kn}^*$, e_{km} is a set of complex values and e_{kn}^* is the complex conjugate of the set of complex values. Eq. 2.60 shows that the channel ξ can be fully described by a complex number matrix χ and a fixed set of operators $\{\hat{E}_m\}$. To find the entries of χ , we can consider a set of operators which are fixed and form a linearly independent basis for the Hilbert-space, ρ_v . Therefore, the output of the channel ξ acting on these operators is obtained by preparing the following input states

$$|n\rangle, |m\rangle, |+\rangle = \frac{1}{\sqrt{2}}(|n\rangle + |m\rangle), |+_y\rangle = \frac{1}{\sqrt{2}}(|n\rangle + i|m\rangle), \quad (2.61)$$

and then forming linear combinations of the outputs $\xi(|n\rangle \langle n|)$, $\xi(|m\rangle \langle m|)$, $\xi(|+\rangle \langle +|)$, and $\xi(|+_y\rangle \langle +_y|)$ as

$$\xi(|n\rangle \langle m|) = \xi(|+\rangle \langle +|) + i\xi(|+_y\rangle \langle +_y|) - \frac{1+i}{2}\xi(|n\rangle \langle n|) - \frac{1+i}{2}\xi(|m\rangle \langle m|). \quad (2.62)$$

Thus, we can get $\xi(\rho_v)$ for each ρ_v by carrying out state tomography on the output states of the above four input states. The density matrix formulation can be use to denote $\xi(\rho_v)$ as

$$\xi(\rho_v) = \sum_k \lambda_{vk} \rho_k, \quad (2.63)$$

where ρ_k are basis states (just like ρ_v but with a different index). Here, $\xi(\rho_v)$ are experimentally determined, whereas the ρ_k are fixed in advance and the λ_{vk} can be calculated

once the $\xi(\rho_v)$ are known. Thus, $\xi(\rho_v)$ is written

$$\xi(\rho_v) = \sum_{mn} \hat{E}_m \rho_v \hat{E}_n^\dagger \chi_{mn} = \sum_{mnk} \beta_{vk}^{mn} \rho_k \chi_{mn} = \sum_k \lambda_{vk} \rho_k \quad (2.64)$$

where $\hat{E}_m \rho_v \hat{E}_n^\dagger = \sum_k \beta_{vk}^{mn} \rho_k$. Therefore, if $\sum_{mnk} \beta_{vk}^{mn} \rho_k \chi_{mn} = \sum_k \lambda_{vk} \rho_k$, we then have

$$\lambda_{vk} = \sum_{mn} \beta_{vk}^{mn} \chi_{mn}. \quad (2.65)$$

To obtain β_{vk}^{mn} , we invert Eq. 2.65 and have

$$\chi_{mn} = \sum_{vk} \kappa_{vk}^{mn} \lambda_{vk}, \quad (2.66)$$

where κ is the generalised inverse of β , that is, it satisfies the condition

$$\beta_{vk}^{mn} = \sum_{st \ xy} \beta_{vk}^{st} \kappa_{st}^{xy} \beta_{xy}^{mn}. \quad (2.67)$$

β is known and fixed regardless of the channel, thus so is κ . Therefore once the λ_{vk} 's are obtained from the experiment we can calculate χ from Eq. 2.66. To find the set $\{E_k\}$ in Eq. 2.58, the matrix χ is diagonalised (since it is a positive Hermitian matrix)

$$D = U^\dagger \chi U \rightarrow \chi_{mn} = \sum_{kv} U_{mv} d_v \delta_{vk} U_{nk}^*, \quad (2.68)$$

where $d_v \delta_{vk} = D_k$ are real and positive. Thus, associating $e_{km} = \sum_v \sqrt{D_k} U_{mk}^*$, we have from Eqs. 2.59 and 2.60

$$E_k = \sum_m e_{km} \hat{E}_m = \sum_m \sqrt{D_k} U_{mk} \hat{E}_m. \quad (2.69)$$

Here, the fixed set of operators, \hat{E}_k are the four Pauli matrices ($\hat{E}_0 = \mathbf{1}$, $\hat{E}_1 = X$, $\hat{E}_2 = iY$, $\hat{E}_3 = Z$).

2.4 Quantum Optics

2.4.1 Light in the quantum regime

In 1900, the quantum theory of light came into being when Planck [114] put forward a theory that the energy radiation in a black body is quantized. After the work of Einstein [115], in 1905, on the photoelectric effect, the quantum nature of light radiation was accepted with the name photon given much later, in 1926 [116].

The initial quantization of the electromagnetic field was done by Dirac [117], in 1927, where he demonstrated that the wave properties of the field could be preserved alongside the concept of creation and annihilation of photons. It was later shown in Ref [118], how the photoelectric effect was fully described by semi-classical theory, whereby the atomic part of the experimental system was described by quantum theory while the radiation was described by classical theory. In 1960, the laser was invented by Maiman [119], with quantum theory applied to both the radiation and to the atoms with which it interacts. The quantum theory of light is an important concept in this thesis and it begins with the wave equation.

Classically, the electromagnetic field in free space with respect to position \mathbf{r} and time t is described by the wave equation

$$-\nabla^2 \mathbf{A}(\mathbf{r}, t) + \frac{1}{c^2} \frac{\partial^2 \mathbf{A}(\mathbf{r}, t)}{\partial t^2} = 0, \quad (2.70)$$

where the vector potential, $\nabla \cdot \mathbf{A} = 0$ (Coulomb gauge). From Eq. 2.70, the vector potential can be written as set of plane waves

$$\mathbf{A}(\mathbf{r}, t) = \sum_{\mathbf{k}\nu} \boldsymbol{\epsilon}_{\mathbf{k}\nu} [A_{\mathbf{k}\nu} e^{i(\mathbf{k}\cdot\mathbf{r} - \omega_{\mathbf{k}}t)} + A_{\mathbf{k}}^* e^{-i(\mathbf{k}\cdot\mathbf{r} - \omega_{\mathbf{k}}t)}] \quad (2.71)$$

Each term in Eq. 2.71 represents a time-dependent oscillating wave propagating in space in the direction of the wavevector, \mathbf{k} , at an angular frequency, $\omega_{\mathbf{k}}$, with a spatial period $\lambda = \frac{2\pi}{k}$. $A_{\mathbf{k}}$ is the wave amplitude which is directed along the polarisation unit vector $\boldsymbol{\epsilon}_{\mathbf{k}v}$. Since the vector potential is in the Coulomb gauge, that is, $\nabla \cdot \mathbf{A} = 0$, then $\mathbf{k} \cdot \boldsymbol{\epsilon}_{\mathbf{k}v} = 0$, or $\mathbf{k} \perp \boldsymbol{\epsilon}_{\mathbf{k}v}$. From the vector potential, the electric field \mathbf{E} and magnetic field \mathbf{B} can be written as

$$\mathbf{E}(\mathbf{r}, t) = -\frac{\partial \mathbf{A}}{\partial t} = i \sum_{\mathbf{k}v} \omega_{\mathbf{k}} \boldsymbol{\epsilon}_{\mathbf{k}v} (A_{\mathbf{k}v} e^{i(\mathbf{k} \cdot \mathbf{r} - \omega_{\mathbf{k}} t)} - A_{\mathbf{k}v}^* e^{-i(\mathbf{k} \cdot \mathbf{r} - \omega_{\mathbf{k}} t)}), \quad (2.72)$$

and

$$\mathbf{B}(\mathbf{r}, t) = \nabla \times \mathbf{A} = i \sum_{\mathbf{k}v} (\mathbf{k} \times \boldsymbol{\epsilon}_{\mathbf{k}v}) A_{\mathbf{k}v} [e^{i(\mathbf{k} \cdot \mathbf{r} - \omega_{\mathbf{k}} t)} - A_{\mathbf{k}v}^* e^{-i(\mathbf{k} \cdot \mathbf{r} - \omega_{\mathbf{k}} t)}]. \quad (2.73)$$

If we assume a unit vector $\boldsymbol{\kappa}$ along the magnetic field polarisation $\boldsymbol{\kappa} = (\mathbf{k} \times \boldsymbol{\epsilon}_{\mathbf{k}v})/|\mathbf{k}| = \boldsymbol{\kappa} \times \boldsymbol{\epsilon}_{\mathbf{k}v}$ with $\boldsymbol{\kappa} = \frac{\mathbf{k}}{|\mathbf{k}|}$, then the wave vector, and the electric and magnetic field's polarisation are mutually orthogonal ($\boldsymbol{\kappa} \perp \boldsymbol{\epsilon}_{\mathbf{k}v} \perp \boldsymbol{\kappa}$). The electric field and magnetic field can now be written as

$$\mathbf{E}(\mathbf{r}, t) = i \sum_{\mathbf{k}v} \omega_{\mathbf{k}} \boldsymbol{\epsilon}_{\mathbf{k}v} (A_{\mathbf{k}v} e^{i(\mathbf{k} \cdot \mathbf{r} - \omega_{\mathbf{k}} t)} - A_{\mathbf{k}v}^* e^{-i(\mathbf{k} \cdot \mathbf{r} - \omega_{\mathbf{k}} t)}), \quad (2.74)$$

and

$$\mathbf{B}(\mathbf{r}, t) = \frac{1}{c} \sum_{\mathbf{k}v} (\boldsymbol{\kappa} \times \boldsymbol{\epsilon}_{\mathbf{k}v}) \omega_{\mathbf{k}} A_{\mathbf{k}v} [e^{i(\mathbf{k} \cdot \mathbf{r} - \omega_{\mathbf{k}} t)} - A_{\mathbf{k}v}^* e^{-i(\mathbf{k} \cdot \mathbf{r} - \omega_{\mathbf{k}} t)}]. \quad (2.75)$$

The energy of the field is given by [120]

$$H = \frac{1}{2} \int_S (\epsilon_0 \mathbf{E} \cdot \mathbf{E} + \frac{1}{\mu_0} \mathbf{B} \cdot \mathbf{B}) dS \quad (2.76)$$

where $S = L^3$ and L is the length of a cubic cavity. The periodic boundary condition gives

$$\int_S e^{\pm i(\mathbf{k} - \mathbf{k}^l) \cdot \mathbf{r}} dS = \delta_{\mathbf{k}\mathbf{k}^l} S. \quad (2.77)$$

The contribution of the electric field to H is

$$\frac{1}{2} \int_S \epsilon_0 \mathbf{E} \cdot \mathbf{E} dS = \epsilon_0 S \sum_{\mathbf{k}v} \omega_{\mathbf{k}}^2 A_{\mathbf{k}v}(t) A_{\mathbf{k}v}^*(t) - R, \quad (2.78)$$

where $R = \frac{1}{2} \epsilon_0 S \sum_{\mathbf{k}v v'} \omega_{\mathbf{k}}^2 \boldsymbol{\epsilon}_{\mathbf{k}v} \cdot \boldsymbol{\epsilon}_{-\mathbf{k}v'} [A_{\mathbf{k}v}(t) A_{-\mathbf{k}v'}(t) + A_{\mathbf{k}v}^*(t) A_{-\mathbf{k}v'}^*(t)]$. Using the vector identity $(A \times B) \cdot (C \times D) = (A \cdot C)(B \cdot D) - (A \cdot D)(B \cdot C)$, we get

$$(\mathbf{k} \times \boldsymbol{\epsilon}_{\mathbf{k}v}) \cdot (\mathbf{k} \times \boldsymbol{\epsilon}_{\mathbf{k}v'}) = \delta_{vv'} \quad (2.79)$$

and

$$(\mathbf{k} \times \boldsymbol{\epsilon}_{\mathbf{k}v}) \cdot (-\mathbf{k} \times \boldsymbol{\epsilon}_{-\mathbf{k}v'}) = -\boldsymbol{\epsilon}_{\mathbf{k}v} \cdot \boldsymbol{\epsilon}_{-\mathbf{k}v'}. \quad (2.80)$$

From the above results we have

$$\frac{1}{2} \int \frac{1}{\mu_0} \mathbf{B} \cdot \mathbf{B} dS = \epsilon_0 S \sum_{\mathbf{k}v} \omega_{\mathbf{k}}^2 A_{\mathbf{k}v}(t) A_{\mathbf{k}v}^*(t) + R. \quad (2.81)$$

Therefore by summing Eqs. 2.78 and 2.81 we obtain the field energy

$$H = 2\epsilon_0 S \sum_{\mathbf{k}v} \omega_{\mathbf{k}}^2 A_{\mathbf{k}v}(t) A_{\mathbf{k}v}^*(t) = 2\epsilon_0 S \sum_{\mathbf{k}s} \omega_{\mathbf{k}}^2 A_{\mathbf{k}v} A_{\mathbf{k}v}^* \quad (2.82)$$

To quantize the field, we introduce canonical variables p_v and q_v and set

$$A_{\mathbf{k}v} = \frac{1}{2\omega_{\mathbf{k}}(\epsilon_0 S)^{1/2}} [\omega_{\mathbf{k}} q_{\mathbf{k}v} + i p_{\mathbf{k}v}] \quad (2.83)$$

$$A_{\mathbf{k}v}^* = \frac{1}{2\omega_{\mathbf{k}}(\epsilon_0 S)^{1/2}} [\omega_{\mathbf{k}} q_{\mathbf{k}v} - i p_{\mathbf{k}v}], \quad (2.84)$$

and substituting Eqs. 2.83 and 2.84 into Eq. 2.82 we have

$$H = \frac{1}{2} (p_{\mathbf{k}v}^2 + \omega_{\mathbf{k}}^2 q_{\mathbf{k}v}^2). \quad (2.85)$$

Thus, the canonical variables become operators that satisfy the commutation relation

$$[\hat{q}_{\mathbf{k}v}, \hat{q}_{\mathbf{k}'v'}] = 0 = [\hat{p}_{\mathbf{k}v}, \hat{p}_{\mathbf{k}'v'}] \quad (2.86)$$

$$[\hat{q}_{\mathbf{k}v}, \hat{p}_{\mathbf{k}'v'}] = i\hbar\delta_{\mathbf{k}\mathbf{k}'}\delta_{vv'}. \quad (2.87)$$

where \hbar is the Planck constant. For a single mode, the annihilation and creation operators are given by

$$\hat{a}_{\mathbf{k}v} = \frac{1}{(2\hbar\omega_k)^{1/2}}[\omega_k\hat{q}_{\mathbf{k}v} + i\hat{p}_{\mathbf{k}v}] \quad (2.88)$$

$$\hat{a}_{\mathbf{k}v}^\dagger = \frac{1}{(2\hbar\omega_k)^{1/2}}[\omega_k\hat{q}_{\mathbf{k}v} - i\hat{p}_{\mathbf{k}v}] \quad (2.89)$$

The energy of the field becomes the Hamiltonian operator

$$\hat{H} = \sum_{\mathbf{k}v} \hbar\omega_k(\hat{a}_{\mathbf{k}v}^\dagger\hat{a}_{\mathbf{k}v} + \frac{1}{2}) = \sum_{\mathbf{k}v} \hbar\omega_k(\hat{n}_{\mathbf{k}v} + \frac{1}{2}), \quad (2.90)$$

where $\hat{n}_{\mathbf{k}v} = \hat{a}_{\mathbf{k}v}^\dagger\hat{a}_{\mathbf{k}v}$ is the number operator for the mode $\mathbf{k}v$. For the j th mode, let $\hat{a}_{\mathbf{k}jv} = \hat{a}_j$ and the Hamiltonian of the field is given by

$$\hat{H} = \sum_j \hbar\omega_j(\hat{n}_j + \frac{1}{2}). \quad (2.91)$$

Therefore, if we apply the Hamiltonian on $|n\rangle$, an energy eigenstate with eigenvalue E_n , we then have for each j

$$\hat{H}|n\rangle = \hbar\omega(\hat{a}^\dagger\hat{a} + \frac{1}{2})|n\rangle = E_n|n\rangle. \quad (2.92)$$

If we multiply both sides of Eq. 2.92 by \hat{a}^\dagger and use the commutation relation $([\hat{a}, \hat{a}^\dagger] =$

$\hat{a}\hat{a}^\dagger - \hat{a}^\dagger\hat{a} = 1$) on the first term of the result, we have [121]

$$\hbar\omega(\hat{a}^\dagger\hat{a} + \frac{1}{2})\hat{a}^\dagger|n\rangle = \hat{H}\hat{a}^\dagger|n\rangle = (E_n + \hbar\omega)\hat{a}^\dagger|n\rangle, \quad (2.93)$$

where $E_n + \hbar\omega$ is a new eigenvalue and $\hat{a}^\dagger|n\rangle$ is a new eigenstate of the harmonic oscillator.

Thus, the new eigenstate and eigenvalue are given by [121]

$$|n+1\rangle = \hat{a}^\dagger|n\rangle, \quad (2.94)$$

and

$$E_{n+1} = E_n + \hbar\omega, \quad (2.95)$$

respectively. Eq. 2.93 can now be expressed as

$$\hat{H}|n+1\rangle = E_{n+1}|n+1\rangle. \quad (2.96)$$

The above equation is an important result which simply means that there exists another energy higher than the first energy by an amount $\hbar\omega$. In a similar fashion, if we multiply Eq. 2.92 by \hat{a} and use the same commutation relation as described above, then we have

$$\hat{H}\hat{a}|n\rangle = (E_n - \hbar\omega)\hat{a}|n\rangle, \quad (2.97)$$

where the new eigenstate and eigenvalue is given by

$$|n-1\rangle = \hat{a}|n\rangle, \quad (2.98)$$

and

$$E_{n-1} = E_n - \hbar\omega, \quad (2.99)$$

respectively. Thus, Eq. 2.97 becomes

$$\hat{H} |n-1\rangle = E_{n-1} |n-1\rangle. \quad (2.100)$$

If we assume the state $|0\rangle$ to be the ground state with an energy E_0 , we have

$$\hat{H}\hat{a}|0\rangle = (E_0 - \hbar\omega)\hat{a}|0\rangle = 0, \quad (2.101)$$

and therefore $\hat{a}|0\rangle = 0$. Then,

$$\hat{H}|0\rangle = \frac{1}{2}\hbar\omega|0\rangle = E_0|0\rangle, \quad (2.102)$$

where $E_0 = \frac{1}{2}\hbar\omega$. The energy of the n -eigenstate is then given by

$$E_n = (n + \frac{1}{2})\hbar\omega, \quad (2.103)$$

where $n = 0, 1, 2, \dots$ and so on. Eq. 2.103 is the energy of a quantum harmonic oscillator which represents each mode j of the quantized electromagnetic field. The state $|n\rangle$ represents the population of each mode j with n photons.

2.4.2 Single-Photon Source

2.4.2.1 Introduction

In many quantum optics experiments, single photons are generated using the spontaneous parametric down-conversion (SPDC) method. SPDC is a non-linear quantum-mechanical process in which a photon from a pump beam at frequency ω_p is converted into two correlated photons at lower frequency, simultaneously. This thesis used a type-1 SPDC

$$\omega_p = \omega_i + \omega_s \quad (2.104)$$

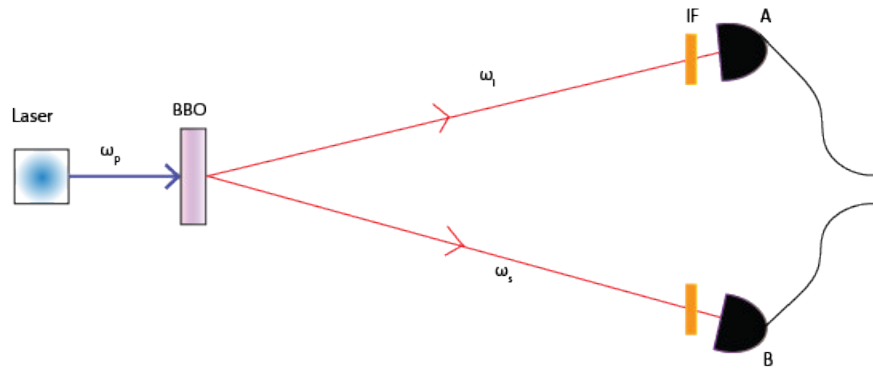


Figure 2.6: SPDC experimental setup. Here, a BBO (β -barium borate) is a nonlinear crystal, IF is an interference filter, and A and B are avalanche photo-detectors.

method. Usually in SPDC, a non-linear crystal (BBO) is used to generate two photon pairs called the idler (propagates through arm A) at a frequency ω_i and the signal (propagates through arm B) at a frequency ω_s , as shown in figure 2.6. In spontaneous parametric down-conversion, energy and momentum are conserved and

$$\mathbf{k}_p = \mathbf{k}_i + \mathbf{k}_s. \quad (2.105)$$

In experiments, a blue laser at 405 nm is used to pump a non-linear crystal. The optical axis of the crystal is cut such that the two photons emerge at 3° from the initial pump direction. The two correlated photons pass through an interference filter (IF) to cut off unwanted light and improve the spectral purity of the photons. A photon detection in arm A is used to herald the presence of another photon in arm B. In the next section, we will discuss the theory of quantum correlation functions which were used to characterise the single photons generated by SPDC.

2.4.2.2 Theory

In classical physics, the light beam intensity-intensity correlations (i.e the beam correlations between intensities I_B and $I_{B'}$ where the light in arm B has been split into B and B' by a 50/50 beamsplitter) is described by the degree of second-order coherence $g_{B,B'}^{(2)}(\tau)$.

$g_{B,B'}^{(2)}(\tau)$ is a function of the time delay τ between the intensity measurements [120] and is given by

$$g_{BB'}^{(2)}(\tau) = \frac{\langle I_B(t)I_{B'}(t+\tau) \rangle}{\langle I_B(t) \rangle \langle I_{B'}(t+\tau) \rangle}, \quad (2.106)$$

where I_B and $I_{B'}$ are the detected intensities. For intensity measurements at zero time delay ($\tau = 0$) the incident intensity $I_I(t)$ gives $I_B(t) = I_{B'}(t) = \frac{1}{2}I_I(t)$, then $g_{BB'}^{(2)}(0)$ can be written as

$$g_{BB'}^{(2)}(0) = \frac{\langle [I_I(t)]^2 \rangle}{\langle I_I(t) \rangle^2} = g^{(2)}(0), \quad (2.107)$$

where $g^{(2)}(0)$ is the second-order coherence for the field in the incident beam. Thus, it follows from the Cauchy-Schwartz inequality [121] that

$$g_{BB'}^{(2)}(0) = g^{(2)}(0) \geq 1 \quad (2.108)$$

In quantum physics, following a similar fashion, the quantum degree of second-order coherence is defined by replacing the I in Eq. 2.106 with a quantum mechanical operator \hat{I} . Thus, the $g_{BB'}^{(2)}(\tau)$ is given by [121]

$$g_{BB'}^{(2)}(\tau) = \frac{\langle : \hat{I}_B(t_1) \hat{I}_{B'}(t+\tau) : \rangle}{\langle \hat{I}_B(t) \rangle \langle \hat{I}_{B'}(t+\tau) \rangle}, \quad (2.109)$$

where the colons represents normally ordered operators with all creation operators to the left and annihilation operators to the right. The numerators of Eq. 2.109 are expectation values of products of creation and annihilation operators with their corresponding Hermitian conjugates and this must be positive. At zero time delay and by substituting in the beamsplitter relations for modes B and B', ie $\hat{a}_B = (\hat{a}_I + \hat{a}_v)/\sqrt{2}$ and $\hat{a}_{B'} = (\hat{a}_I - \hat{a}_v)/\sqrt{2}$ we get

$$g_{BB'}^{(2)}(0) = g^{(2)}(0) = \frac{\langle \hat{n}_I(\hat{n}_I - 1) \rangle}{\langle \hat{n}_I \rangle^2} = 1 - \frac{1}{n}, \quad n \geq 2, \quad \text{and } = 0 \text{ for } n = 0, 1, \quad (2.110)$$

where \hat{n}_I is the photon-number operator and n is the mean photon number. For single-photons, $n = 1$ and $g^{(2)}(0) = 0$. However, in the case where $n = 2$, $g^{(2)}(0) = 0.5$. Thus, following this simple calculation, we expect a value of $g^{(2)} < 0.5$ to show we are in the single-photon regime in an experiment. In the laboratory, single-photon measurements rely on counting statistics and coincidence measurements. Here, heralded single photons were generated using spontaneous parametric down conversion. For two detectors B and B', $g_{BB'}^{(2)}(0)$ can be defined as [122]

$$g_{BB'}^{(2)}(0) = \frac{N_{BB'}}{N_B N_{B'}} N_P, \quad (2.111)$$

where $N_P = T/\tau_c$ is the total possible number of coincidences, T is the total measurement time and τ_c is the coincidence window. $N_{BB'}$ is the coincidence count rate of detector B and B', N_B is the count rate for detector B and $N_{B'}$ is the count rate for detector B'. For three detectors, $g_{ABB'}^{(2)}(0)$ is defined by [122]

$$g^{(2)}(0) = g_{ABB'}^{(2)}(0) = \frac{N_{ABB'}}{N_{AB} N_{AB'}} N_A, \quad (2.112)$$

where $N_{ABB'}$ corresponds to coincidence counts between detectors A, B and B'

2.4.2.3 Experimental setup

To carry-out $g^2(0)$ measurements in the laboratory, a Hanbury-Brown and Twiss (HBT) interferometer was constructed. Figure 2.7 shows a diagram of the HBT interferometer. The associated electronics are placed inside a black box. The photons in arm A of

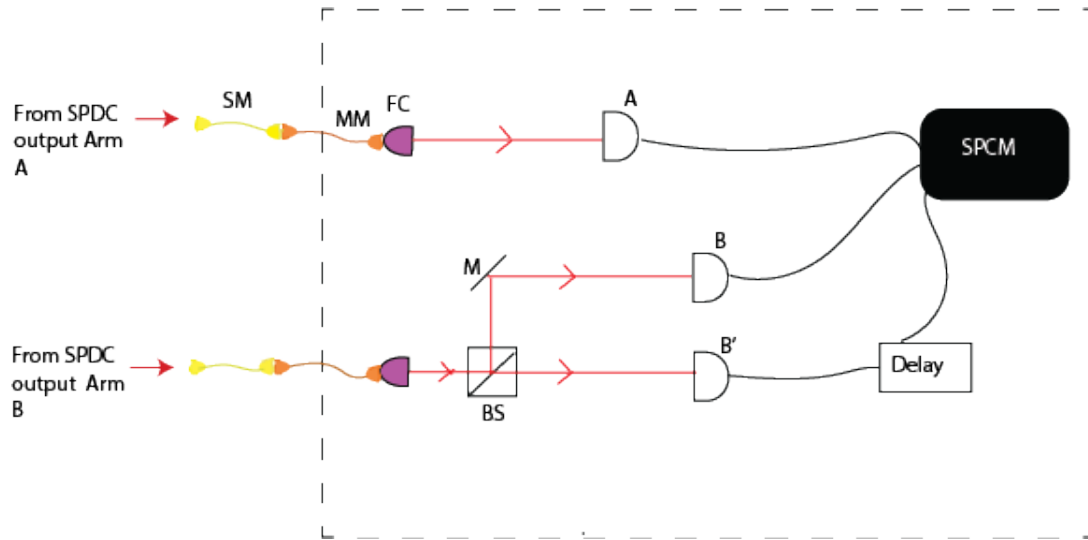


Figure 2.7: A diagram of a Hanbury-Brown and Twiss interferometer, with associated electronics. The output of arm B of the SPDC is connected to the input arms of the interferometer. Here, SM is a single-mode fibre, MM is a multi-mode fibre, FC is a fibre coupler, M is a mirror, BS is a beam splitter, and A, B, and B' are avalanche photo detectors. SPCM is a single-photon counting module.

figure 2.6 are collected using a single-mode fibre (SM). The SM is then connected to a multi-mode fibre (MM) through which single photons are decoupled and focussed onto a single-photon avalanche photo detector (Excelitas SPCM-AQRH-15). In a similar fashion, the photons in arm B of figure 2.6 are decoupled and focussed onto a HBT interferometer such that we may measure correlations between photo-detections at detectors B and B'. The signal from a detected photon is sent through a delay circuit with a delay (τ) that ranges from 0 to 64.5 ns with a resolution of 0.5 ns. In order to set a negative time delay, additional BNC cables were used in such a manner that B' arrives before A and B.

The three detected signals are then sent to a single-photon counting module which then output the photon count rates at each detector, and the coincidence count rates between detectors A, B and B'. The outputs from the counting module are then sent to a personal computer (PC) for recording. On the PC, the count rates were monitored and recorded using a LABVIEW program. Note that SM fibres can directly couple the photons to the rest of the experimental setup in Figure 2.7. The reason that MM fibres were used is that the detectors, and the Hanbury-Brown and Twiss interferometer were set up in the lab for

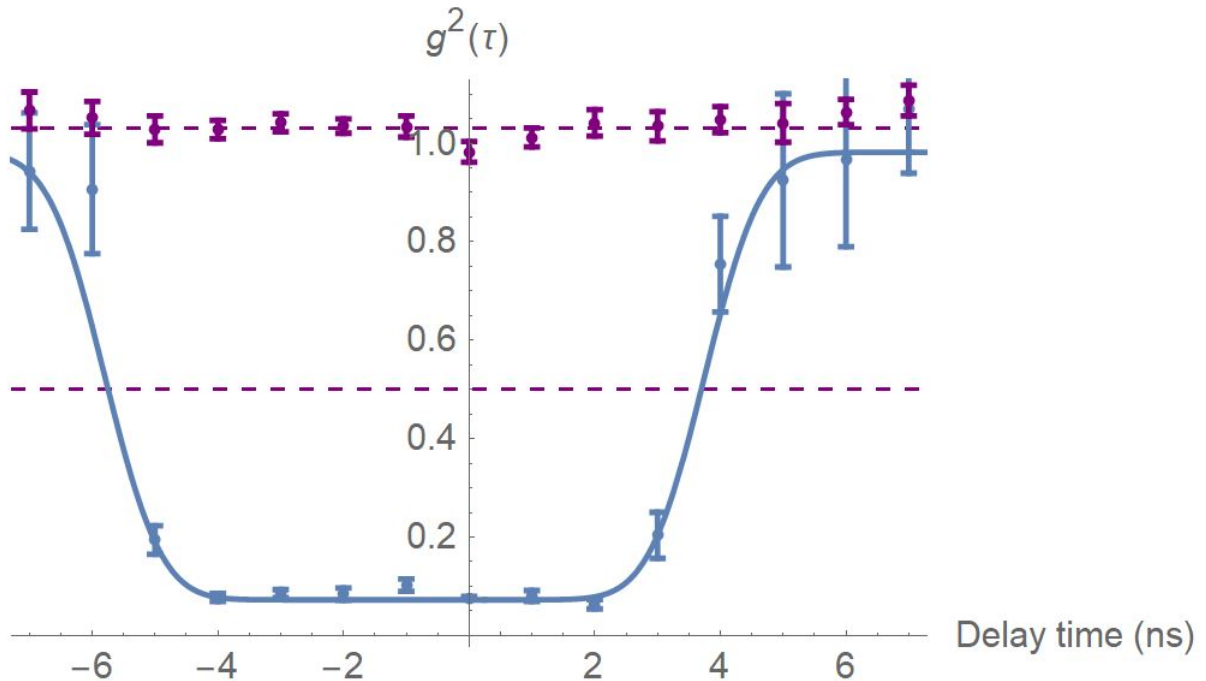


Figure 2.8: A plot of the degree of second-order coherence as a function of delay time. The solid line is for 3 detectors, while the dotted line is for 2 detectors.

common use. Having MM fibres was the most practical configuration due to the different requirements of the other projects.

2.4.2.4 Results and discussion

The photons from both arms of the SPDC source are filtered using an interference filter at 800 ± 5 nm. Table 2.1 shows an example of the count rates obtained. Using Eq. 2.112, a $g^{(2)}$ value for each time delay was then calculated. The average and standard deviation of the set of $g^{(2)}(0)$ values at $\tau = 0$ is 0.081 ± 0.004 and 1 ± 0.001 for 3 and 2 detectors, respectively. Each of the runs was for 5 seconds total measurement time. Figure 2.8 shows a plot of $g^{(2)}(\tau)$ as a function of delay time τ . The results violate the classical lower-bound of 1 for the 3 detectors case (heralded single photon) and is less than the 0.5 predicted for single photons, therefore confirming the presence of single photon

excitations. The trend of the curve in figure 2.8 could be simulated as a convolution of

a wide top-hat function with a Gaussian shape [123]. The shape of the curve is dominated by a strong correlation between detections A and B' [123]. The curve was fitted to an error function equation of the form: $\text{erf}(\tau - w) + \text{erf}(-\tau - w)$, where w is the width. The width consists of the coincidence window (τ_c), coherence time, and detector jitter time. By fitting the curve with a function of the form: $f(\tau) + f(-\tau)$, where $f(\tau) = \text{erf}(b T + c) + d$, we can extract the base-width parameter c which gives $c = 9 \pm 0.5$ ns. However, using Eq. 2.111 we have a more accurate value of $\tau_c = 8 \pm 0.06$ ns.

A BBO was used as an example nonlinear crystal early in the project to show how single-photons could be generated and characterized. However, the nonlinear crystal was then replaced with a BiBO crystal for the remainder of the work, including the study on metamaterials and Markovian channels, as it offered a higher generation rate compared to the BBO. The BiBO crystal has similar properties to the BBO crystal, and so such a detailed characterization was not carried out - only g_2 at zero delay was measured, which matched closely the value of 0.08 obtained from the BBO crystal, thus confirming single photons could be generated by the BiBO and used in probing quantum channels. This is outlined next in Chapters 3 and 4.

Table 2.1: Counts rate at zero time delay

N_A (10^4 cps)	N_B (10^4 cps)	$N_{B'}$ (10^4 cps)	N_{AB} (10^3 cps)	$N_{AB'}$ (10^3 cps)	$N_{BB'}$ (10^1 cps)	$N_{ABB'}$ (cps)
94	29	36	11	13	185	13

Chapter 3

Active control of a plasmonic metamaterial for quantum state engineering

3.1 Introduction

The metallic nanostructures in metamaterials, the ‘unit cells’, are usually arranged periodically in close range to each other, and their material and geometrical properties can be manipulated in order to change the bulk permittivity ϵ and permeability μ of the material. Here, we consider metallic metamaterials. The unusual optical behaviour of metamaterials is due to the collective oscillations of the nanostructures in resonance with the incident light, i.e. a localised surface plasmon resonance [124, 76]. This plasmonic resonance gives metamaterials the ability to control and manipulate many different aspects of light. Controlling the polarisation of light is an important process in many areas of science and technology, for example in communication [125], imaging [48], and sensing [126]. Over the years, conventional optical polarisers have been made from birefringent materials [127], and from crystals or polymers [128]. Recently, the control of the polarisation of light

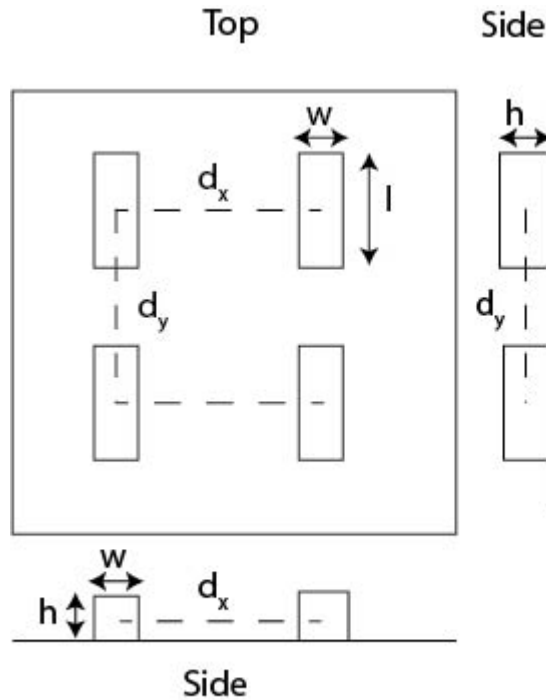


Figure 3.1: A schematic diagram of the metamaterials investigated in this thesis.

using metamaterials has become possible. Shen et al. [54] have demonstrated an ultra-high efficiency metamaterial polariser, where light that is perpendicular to the principal axis is transmitted undisturbed, while light that is parallel is attenuated. Tam and Yan [53] have designed a plasmonic ultra-broadband polariser based on silver nanowire arrays where a broadband transmission was realised. Chin et al. [129] have shown that, with designed metamaterials mimicking anisotropic crystals, it is also possible to change the polarisation state of the field during the polariser operation. In this chapter we theoretically and experimentally investigate a plasmonic metamaterial polariser in the quantum regime. We go further than the previous work and demonstrate the active control of a plasmonic metamaterial polariser in the quantum regime.

3.2 Transmission of single-photons through plasmonic metamaterials: Simulations

In this section we describe the theory of transmission of single-photon states through different metamaterial designs. For this we model the metamaterial as a periodic array of nanoparticles in a rectangular lattice with periods d_x and d_y , as shown in Figure 3.1. In the dipole approximation, each nanoparticle representing a unit cell of the metamaterial is modelled by a dipole with polarisability tensor α , which relates the dipole moment to the local electric field at the particle [130, 88, 131]. The plasmonic nanoparticles in this work are rod-like in shape and are well described as an ellipsoid with semi-axes a , b and c . This gives a diagonal polarisability tensor with non-zero elements [88] as given in Eq. 2.6, and re-written here

$$\alpha_{ii} = 4\pi\epsilon_0 abc \frac{\epsilon_m - \epsilon_d}{3\epsilon_d + 3L_i(\epsilon_m - \epsilon_d)} \quad (3.1)$$

where ϵ_0 is the free space permittivity, L_i ($i = x, y, z$) is a shape factor, $\epsilon_m = -22.842 + 1.8388i$ is the relative permittivity of gold and $\epsilon_d = (1.45)^2$ the relative permittivity of the surrounding medium (silica) at 810 nm. In our simulation, $a = l/2$, $b = w/2$, and $c = t/2$, where l is the length of the nanorod, w is the width and t is the height. As an example we use $d_x = d_y = 200$ nm for the period, $l = 110$ nm for the length, $w = 39$ nm for the width and $t = 30$ nm for the thickness. The transmission (\mathcal{T}) and reflection (R) of light through periodic arrays of these kind of nanoparticles are described in detail in Ref. [131] and for light with normal incidence to the array and polarised in direction k as

$$\mathcal{T}_k = 1 + \frac{i\mu_0\pi fc}{d_x d_y} \frac{\alpha_k}{1 - \beta_k \alpha_k}, \quad (3.2)$$

where $R_k = \mathcal{T}_k - 1$, μ_0 is the free space permeability, f is the frequency of the propagating electromagnetic wave and c is the speed of light in a vacuum. Here we set the interaction

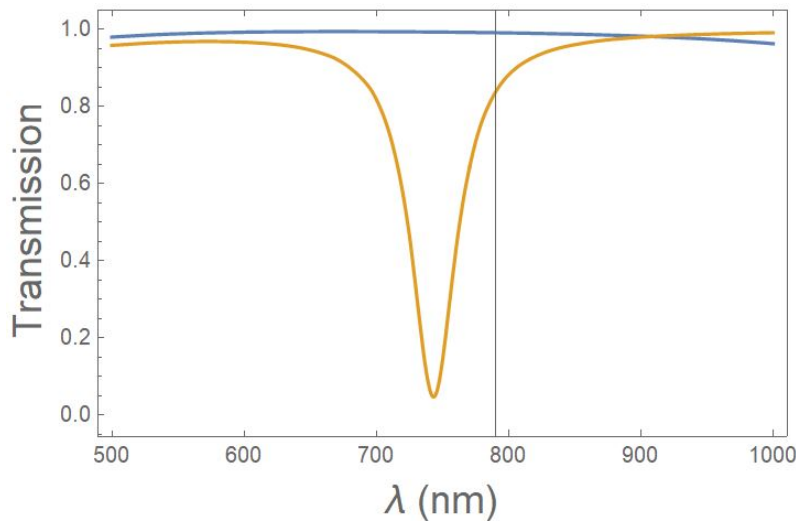


Figure 3.2: Theoretical transmission spectra for horizontally (orange line) and vertically (blue line) polarised light sent through a plasmonic metamaterial made of gold nanorods ($w = 39$ nm, $l = 110$ nm, $t = 30$ nm). The dashed line corresponds to 810 nm.

parameter $\beta_k = 0$ as we consider a large nanorod spacing. Note that in the special case of no absorption in the array, the relation $|R|^2 + |\mathcal{T}|^2 = 1$ is satisfied. However, when $\beta_k \neq 0$, the transmission gets modified (see Ref. [131] for more details). With these equations at hand, we are able to model the transmission of single photons of horizontal and vertical polarisation through different metamaterial designs. Figure 3.2 shows the transmission spectra that were obtained by simulations via a particular plasmonic metamaterial with the dimensions given above. The vertical axis of the polarisation is oriented along the long axis of the nanorods. From the above theory, this means that the probability of transmitting a photon encoded in the state $|V\rangle$ through a metamaterial should decrease as the nanorod length in the metamaterial increases and width decreases. This is due to a stronger plasmonic resonance of the nanorod. On the other hand, the transmission of a photon encoded in the state $|H\rangle$ is constant for all the metamaterial designs as the plasmonic resonance is weak along the width of the nanorod. The horizontally polarized light was transmitted at 810nm wavelength $\sim 100\%$ with no disturbance and $\sim 81\%$ of vertically polarized light was transmitted for this particular metamaterial design.

3.3 Temperature dependence of single photon transmission via plasmonic metamaterials: Simulations

One of the aims of this work is to study how to actively control the transmission response of single photons of horizontal and vertical polarisation states via different plasmonic metamaterials. In order to do this, we need to develop a theoretical model that can be used to explain our experimental results. At this point, it is important to note that the plasmonic metamaterials studied are made of gold nanoparticles that are deposited on a silica substrate. Therefore, for a start, we need to model the temperature dependence of the permittivities of gold (ϵ_{au}) and the surrounding medium, of which, in our case, is fused-silica (ϵ_d). Thus, we report the temperature dependence of the permittivity of fused-silica in the next sub-section.

3.3.1 Temperature dependence of the permittivity of fused-silica

To model the temperature dependence of the silica substrate we use the wavelength-dependent thermo-optic coefficient $d\eta/dT$, where η is the refractive index ($\epsilon_d = \eta^2$) and T is the temperature [132, 133]. The refractive index is related to the thermo-optic coefficient by the relation

$$\eta(T) = \eta(T_r) + (T - T_r)d\eta/dT, \quad (3.3)$$

where $\eta(T)$ is the temperature-dependent refractive index, which is also wavelength dependent, and $T_r = 300 \text{ K}$ is a reference temperature. It is known that the refractive index of fused silica at T_r can be well described by the Sellmeier equation

$$\eta(T_r, \lambda) = \left[1 + \frac{A_1\lambda^2}{\lambda^2 - \beta_1^2} + \frac{A_2\lambda^2}{\lambda^2 - \beta_2^2} + \frac{A_3\lambda^2}{\lambda^2 - \beta_3^2}\right]^{1/2}, \quad (3.4)$$

where

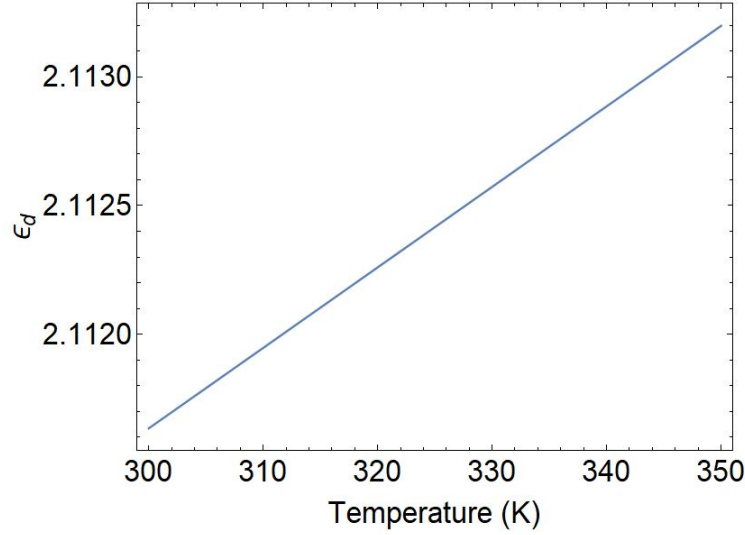


Figure 3.3: Temperature dependence of the permittivity ϵ_d of the silica substrate.

the coefficients are $A_1 = 0.6961663$, $A_2 = 0.4079426$, $A_3 = 0.8974794$, $B_1 = 0.0684043$, $B_2 = 0.1162414$, and $B_3 = 9.896161$ and $\lambda = 0.81 \mu\text{m}$ is the wavelength of interest. We then have

$$\frac{d\eta}{dT} = \frac{(GR + HR^2)}{2\eta(T_r, \lambda)}, \quad (3.5)$$

with $R = \lambda^2/(\lambda^2 - \lambda_{ig}^2)$, $\lambda_{ig} = 0.109 \mu\text{m}$ is the band-gap wavelength of silica, $G = -1.6548 \times 10^{-6} \text{ }^{-1}$, and $H = 31.7794 \times 10^{-6} \text{ K}^{-1}$ [132]. The temperature dependence of ϵ_d is shown in figure 3.3 for $T = 300$ to 350 K . ϵ_d increases as the temperature increases.

3.3.2 Temperature dependence of the permittivity of gold

For the gold nanorods, the temperature dependence is described using a modified Drude model, valid below the interband transition frequency 2.4 eV ($\lambda \geq 520 \text{ nm}$) [62 - 64],

$$\epsilon_m(T) = \epsilon_\infty - \frac{\omega_p^2(T)}{\omega[\omega + i\omega_c(T)]}, \quad (3.6)$$

where ω is the angular frequency of the electromagnetic field, ϵ_∞ is the high-frequency permittivity of the metal, and $\omega_p(T)$ and $\omega_c(T)$ represent the temperature-dependent

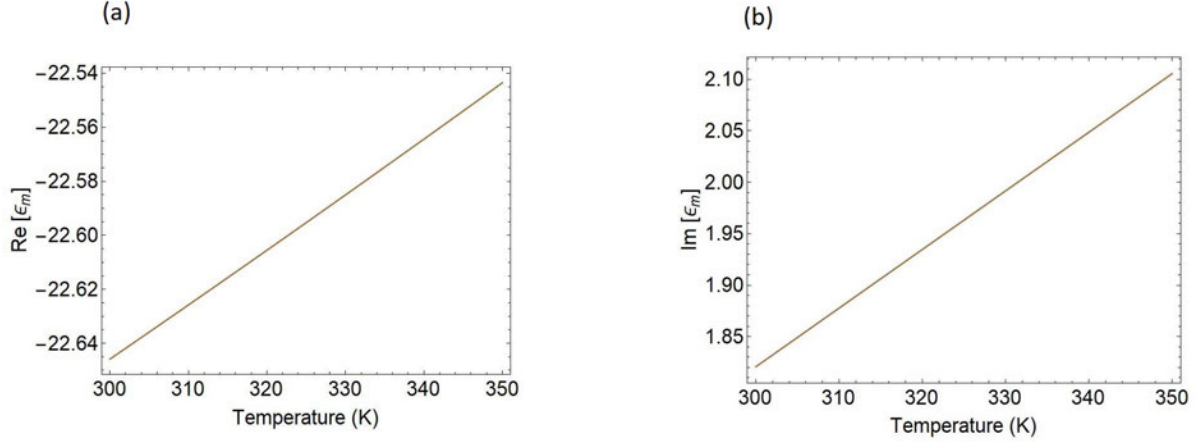


Figure 3.4: Temperature dependence of the permittivity ϵ_m of the gold used for the nanorods. (a) $\text{Re}[\epsilon_m]$ and (b) $\text{Im}[\epsilon_m]$

plasmon frequency and collision frequency of the free electrons, respectively. The plasmon frequency is given by

$$\omega_p(T) = \frac{\omega_p(T_r)}{[1 + 3\gamma(T - T_r)]^{1/2}}, \quad (3.7)$$

where $\omega_p(T_r)$ is the plasmon frequency at the reference temperature and $\gamma = 14.2 \times 10^{-6} \text{ K}^{-1}$ is the thermal linear expansion coefficient. The collision frequency results from a combination of electron-electron and electron-phonon scattering, with $\omega_c(T) = \omega_{e-e}(T) + \omega_{e-ph}(T)$, where

$$\omega_{e-e}(T) = \frac{\pi^3 \Gamma \Delta [(k_B T)^2 + (\hbar\omega/2\pi)^2]}{12\hbar E_F}, \quad (3.8)$$

and

$$\omega_{e-ph}(T) = \omega_0 \left[\frac{2}{5} + 4 \left(\frac{T}{\theta_D} \right)^5 \int_0^{\theta_D/T} z^4 (e^z - 1)^{-1} dz \right]. \quad (3.9)$$

Here k_B is the Boltzmann constant, \hbar is Planck's constant, θ_D is the Debye temperature, E_F is the Fermi-level energy for gold, Γ is the Fermi-surface average of scattering probability, Δ is the fractional umklapp scattering coefficient, and ω_0 is a constant. The

following parameters are used for the above equations: $\theta_D = 185$ K, $E_F = 5.5$ eV, $\Gamma = 0.55$, and $\Delta = 0.77$ [64]. Furthermore, the following parameters are obtained by fitting the experimental data for gold from Ref. [62] at the reference temperature ($\lambda \geq 600$ nm) to Eq. 3.6: $\omega_0 = 0.346$ eV, $\epsilon_\infty = 8$, and $\omega_p(T_r) = 53.41$ eV. The temperature dependence of ϵ_m is shown in figure 3.4(a) for $\text{Re}[\epsilon_m]$ and figure 3.4(b) for $\text{Im}[\epsilon_m]$, for $T = 300$ to 350 K. The permittivity for the real and imaginary parts increases as the temperature increases. Thus, we are now ready to model the temperature-dependent response of the plasmonic metamaterial transmission in the quantum regime.

3.3.3 Temperature dependence of plasmonic metamaterials in the quantum regime

We now theoretically model the active control of plasmonic metamaterial transmission in the quantum regime using the temperature response. Using Eqs. 3.3 and 3.6 in Eq. 3.1, and we are able to model the temperature-dependent response. As an example, in figure 3.5(a) we show the transmission $|T|^2$ for horizontal and vertical polarized light over the wavelength range 600 - 1000 nm for a metamaterial at two different temperatures ($T = 300$ and 340 K). The dimensions used for the simulation are chosen based on the size of the nanorods available in the experiment and given by $d_x = d_y = 200$ nm for the period, $t = 30$ nm for the thickness, $w = 46$ nm for the width, and $l = 130$ nm for the length. One can clearly see the change in the transmission for vertically polarized light as the temperature changes (lower solid and dotted curves), whereas the transmission for horizontally polarized light is not affected significantly (upper solid line). This contrast is due to the dependence of the vertical transmission coefficient on the plasmon resonance

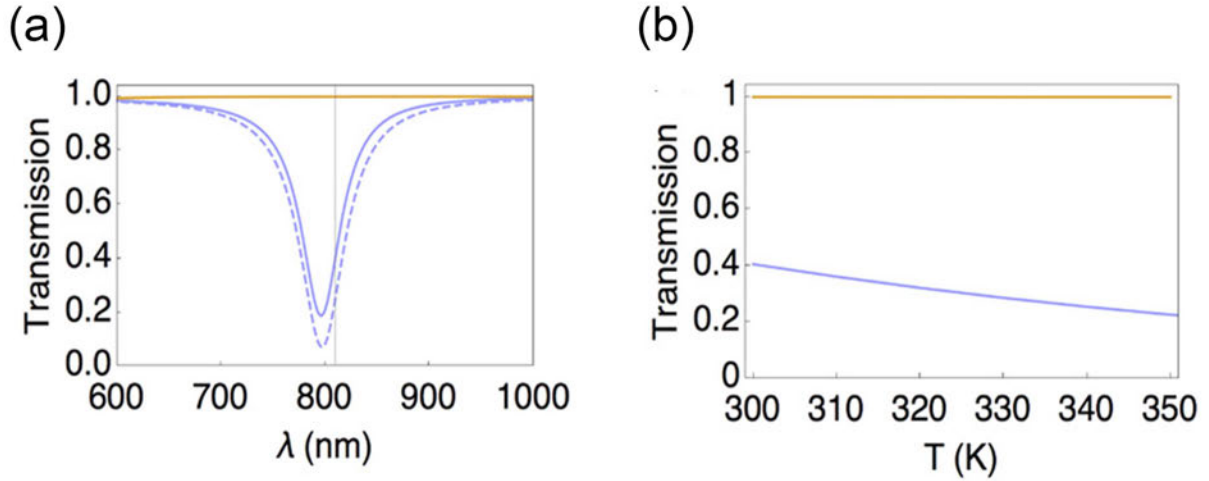


Figure 3.5: Temperature-dependent transmission response of a plasmonic metamaterial with nanorod dimensions, width $w = 46$ nm and length $l = 130$ nm (theory). The period is fixed at $d_x = d_y = 200$ nm and the thickness is $t = 30$ nm. In (a) the lower solid resonance curve is for vertical transmission at $T = 300$ K and the lower dotted resonance curve is for vertical transmission at $T = 340$ K. The horizontal solid line is for horizontal transmission. (b) Corresponding temperature dependence over a range of 50 K at $\lambda = 810$ nm with the nanorod dimensions chosen as those used in (a).

along the length of the nanorod, which is relatively strong and can change significantly depending on the value of the permittivity of the metal. On the other hand, for horizontally polarized light, the plasmonic resonance is weak along the width of the rod and so changes in the permittivity do not have a significant effect. In figures 3.5(a), 3.6(a), 3.7(a) and 3.8, a vertical line marks the wavelength of interest for our experiment ($\lambda = 810$ nm). In figure 3.5(b) we show the temperature dependence of the transmission for $\lambda = 810$ nm over the range 300-350 K. In order to understand further how the transmission changes depending on the nanorod dimensions, we show two more examples of metamaterials in figures 3.6(a), 3.6(b), 3.7(a), and 3.7(b). The dimensions used are the same as the previous example but with $w = 47$ nm and $l = 140$ nm for figures 3.6(a) and 3.6(b) and $w = 48$ nm and $l = 144$ nm for figures 3.7(a) and 3.7(b). One can see that, depending on the nanorod dimensions, the value of the transmission for vertically polarized light can vary significantly as the temperature is modified. In figure 3.8 we show how deviations in the

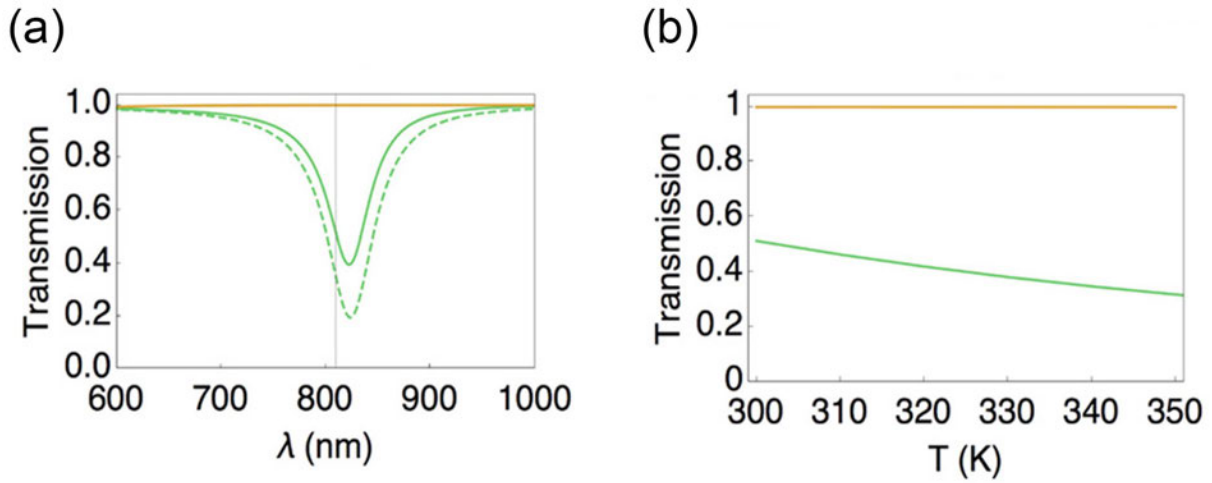


Figure 3.6: Temperature-dependent transmission response of a plasmonic metamaterial with nanorod dimensions: width $w = 47$ nm and $l = 140$ nm (theory). The period is fixed at $d_x = d_y = 200$ nm and the thickness is $t = 30$ nm. In (a) the lower solid resonance curve is for vertical transmission at $T = 300$ K and the lower dotted resonance curve is for vertical transmission at $T = 340$ K. The horizontal solid line is for horizontal transmission. (b) Corresponding temperature dependence over a range of 50 K at $\lambda = 810$ nm with the nanorod dimensions chosen as those used in (a).

nanorod dimensions (± 2 nm for w , t , and l) affect the transmission of vertically polarized light through the metamaterial at a fixed temperature of 300 K. One can see that with only a small deviation of 2 nm the transmission curve plotted as a function of the wavelength of the incident light is shifted considerably to the left (+2 nm) or to the right (-2 nm). This provides useful information about how a realistic metamaterial might respond, as consistency of nanorod dimensions across the array is hard to achieve during fabrication. Based on the behaviour seen in figure 3.8, the result of this would be a linewidth broadening and a shift of the wavelength where the transmission becomes a minimum (the resonance wavelength). We assume ± 2 nm fabrication precision.

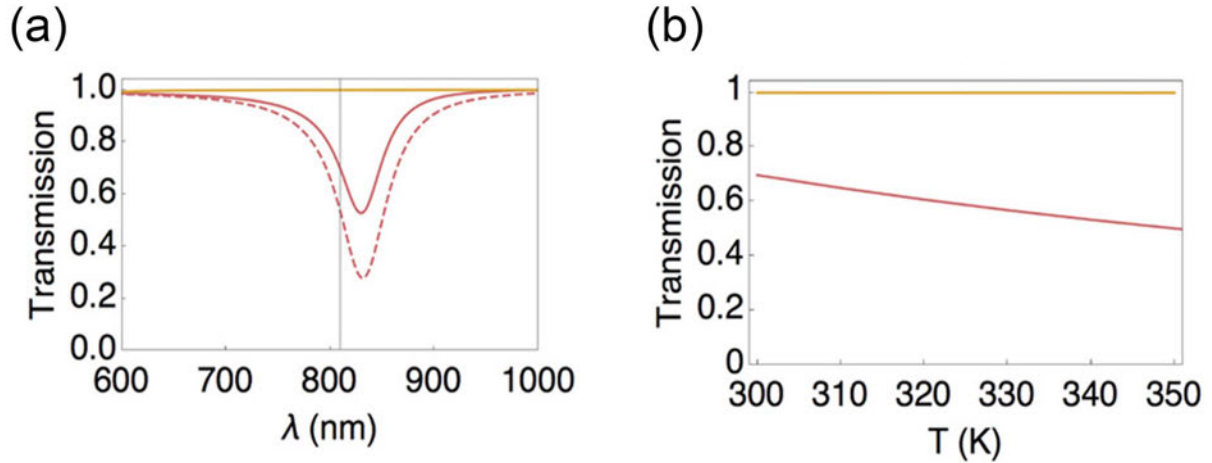


Figure 3.7: Temperature-dependent transmission response of a plasmonic metamaterial with nanorod dimensions: width $w = 48$ nm and $l = 144$ nm. (theory). The period is fixed at $d_x = d_y = 200$ nm and the thickness is $t = 30$ nm. In (a) the lower solid resonance curve is for vertical transmission at $T = 300$ K and the lower dotted resonance curve is for vertical transmission at $T = 340$ K. The horizontal solid line is for horizontal transmission. (b) corresponding temperature dependence over a range of 50 K at $\lambda = 810$ nm with the nanorod dimensions chosen as those used in (a).

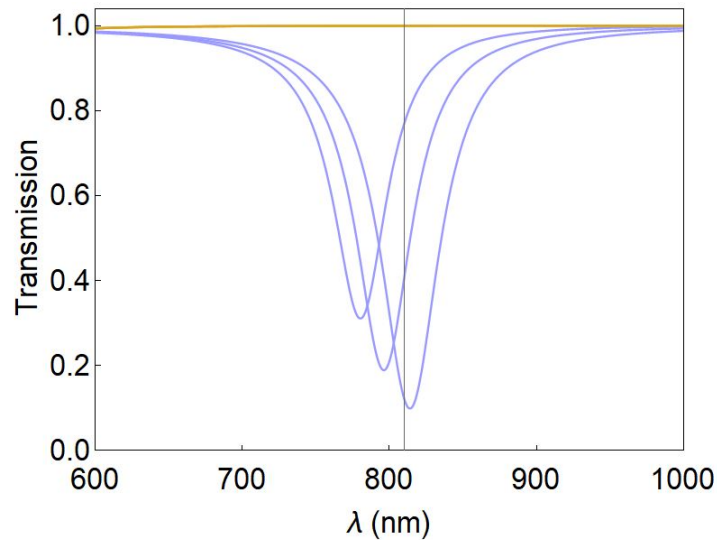


Figure 3.8: Transmission response of a metamaterial with nanorod dimensions corresponding to figure 3.5(a) in the middle and with ± 2 nm added to the length, width and thickness. A larger variation of the nanorod size leads to even bigger shifts in the response.

3.4 Transmission of single photons through plasmonic metamaterials: Experiment

We now present the experimental results of single photons transmitted through plasmonic metamaterials. We begin by presenting the experimental setup.

3.4.1 Experimental setup

The experimental setup is shown in figure 3.9 (a), where type-1 SPDC is used to generate pairs of single photons [134, 135]. A pump laser at 405 nm is rotated to vertical polarisation by a half-wave plate (HWP). The pump beam is then sent through a non-linear crystal, which produces two ‘twin’ (idler and signal) photons polarised horizontally at a lower frequency (wavelength 810 nm). One photon is produced in arm A and the other in arm B. The optical axis of the crystal is cut such that the two photons emerge at $\pm 3^\circ$ from the initial pump direction. A single photon in arm A is used to herald the presence of another single photon in arm B. A qubit is encoded into the single photon in arm B using a quarter-wave plate (QWP) and HWP. Here, the polarisation states $|H\rangle$ and $|V\rangle$ are used as the orthogonal basis states of the qubit. This qubit is then sent through the plasmonic metamaterial. Quantum state tomography is performed on the output of six different polarisation-encoded qubits sent through the metamaterial using a QWP, HWP and a polarising beamsplitter (PBS). This allows the density matrices to be reconstructed via projective measurements [113]. The output of our projective measurement is sent into fibre couplers and coincidence counts between arms A and B are detected by silicon avalanche photodetectors and a coincidence counting unit. In this initial study we use large bandwidth interference filters (800 ± 20 nm) is placed in front of each fibre coupler to cut out photons of higher and lower frequencies corresponding to unwanted down-conversion processes and the pump beam. Later we narrow this bandwidth to improve the spectral quality of the photons, although at the expense of the count rate. Figure 3.9 (b) shows

the telescope system used to focus the single photons onto the metamaterial and Thorlabs DCC1545M monochrome CCD for imaging. Here, the count rate was ~ 4000 counts per second. The interference filter with large bandwidth was used to allow more counts to be collected. As mentioned above, we narrow this in the next section to improve the spectral quality of the photons. The metamaterial sample is translated using an X-Y translation stage. Figure 3.9 (c) shows an image obtained from the CCD displaying the sample used with different metamaterial designs (each $100 \times 100 \mu\text{m}$). An alignment beam (785 nm) sent from the fibre coupler back through the system can be seen at one of the metamaterial designs. The telescope system is designed in such a way that the beam before and after the lenses (plano-convex, $f=25\text{mm}$) is collimated and therefore the beam diameter of single photons traversing in the opposite direction will be roughly the same as that of the alignment beam, which is focused to $\sim 100 \mu\text{m}$ at the metamaterial surface. When single-photons are used in the setup the beamsplitter and mirror in figure 3.9 (b) are flipped down.

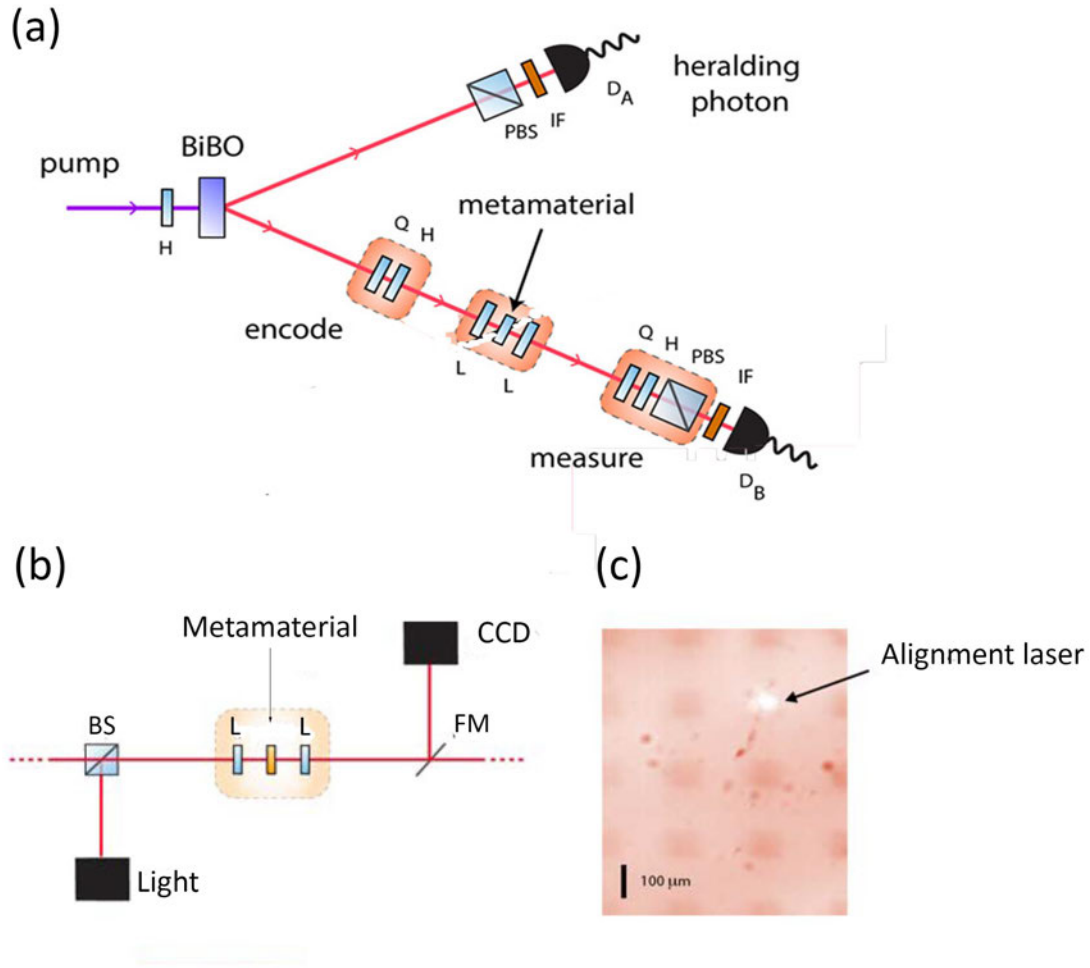


Figure 3.9: Overview of the experiment. (a) Experimental setup. Here, L is a convex lens, HWP and QWP are a half- and quarter-wave plate, BiBO is a nonlinear crystal, PBS is a polarising beamsplitter, IF is an interference filter (800 nm and $\Delta\lambda = 40$ nm) and D_A and D_B are avalanche photodetectors. (b) Telescope system for imaging the alignment laser and its position on different metamaterials. FM is a flip mirror. (c) Image of metamaterials with the alignment beam on a particular design.

3.4.2 Quantum State probing

The input probe states are encoded experimentally by using a QWP and HWP set at a particular angle (see encode box in figure 3.9 (a)). The unitary operations of the wave

plates acting on the polarisation qubit of the single photon in arm B are given by

$$\hat{U}_{QWP}(q) = \frac{1}{\sqrt{2}} \begin{bmatrix} i - \cos(2q) & \sin(2q) \\ \sin(2q) & i + \cos(2q) \end{bmatrix} \quad (3.10)$$

and

$$\hat{U}_{HWP}(h) = \begin{bmatrix} \cos(2h) & -\sin(2h) \\ -\sin(2h) & -\cos(2h) \end{bmatrix}. \quad (3.11)$$

By choosing the angles correctly [18] we obtain six different polarisation-encoded qubits

$$\begin{aligned} |H\rangle &= \begin{pmatrix} 1 \\ 0 \end{pmatrix}, |V\rangle = \begin{pmatrix} 0 \\ 1 \end{pmatrix}, |+\rangle = \frac{1}{\sqrt{2}} \begin{pmatrix} 1 \\ 1 \end{pmatrix}, \\ |-\rangle &= \frac{1}{\sqrt{2}} \begin{pmatrix} 1 \\ -1 \end{pmatrix}, |L\rangle = \frac{1}{\sqrt{2}} \begin{pmatrix} 1 \\ i \end{pmatrix}, |R\rangle = \frac{1}{\sqrt{2}} \begin{pmatrix} 1 \\ -i \end{pmatrix} \end{aligned} \quad (3.12)$$

where $|H\rangle$, $|V\rangle$, $|+\rangle$, $|-\rangle$, $|L\rangle$ and $|R\rangle$ correspond to horizontal, vertical, diagonal, anti-diagonal, left- and right-circularly polarised single photons, respectively. We send these probe states through the metamaterial and perform quantum process tomography based on the state tomography, which was done for six input states as described in detail in chapter 2.

3.4.3 Results and discussion

We now present our experimental results and compare them with results obtained via the theory outlined in the previous section. Figure 3.10 shows the results from experimental probing of horizontal and vertical polarised light via several metamaterials in our setup with different nanorod dimensions (dimension details are given in the figure caption). The transmission response for $|H\rangle$ and $|V\rangle$ polarisation encoded photons were calculated using $T_H = \frac{T_{HM}}{T_{HS}}$ and $T_V = \frac{T_{VM}}{T_{VS}}$, respectively. Here, T_{HS} and T_{HM} are the transmission

probabilities of the state $|H\rangle$ through the substrate (no metamaterial) and through the metamaterial, respectively. Similarly, T_{VS} and T_{VM} are the transmission probabilities of the state $|V\rangle$ through the substrate and metamaterial, respectively. As can be seen in figure 3.10 the transmission of the state $|V\rangle$ decreases from 85% to 75% as the nanorod dimensions vary in the metamaterial (length and thickness fixed, width decreases). On the other hand, the plasmonic metamaterials transmit $\approx 99\%$ of the state $|H\rangle$ compared to the bare substrate. In the experimental results in figure 3.10, the metamaterial design ‘P10’ has nanorods with the same dimensions as those used in the theory for figure 3.2. Considering the finite bandwidth of the single photons, the experimental results are in good agreement with the average transmission obtained from the theory. Also, the trend of our results generally agrees with the transmissions obtained by Asano et al. in Ref. [62], which reported transmissions from 11% to 41% for T_V by classical FTIR for metamaterials with similar nanorod structures, but a different range of dimensions (increasing width) and thus transmission response. The experiment gave a transmission of 1 for horizontally polarized photons and 0.7 for vertically polarized photons, as shown in Figure 3.10. In the theory plot of Figure 3.2 there is a transmission of 1 for horizontally polarized photons and 0.8 for vertically polarized photons. The inconsistency between the theory and experimental results can be attributed to various factors, including the spot size and alignment of the single photons, along with geometric considerations, such as the background permittivity not completely encompassing the nanorods and consistency of the fabrication of the nanorods across the metamaterial and spectral bandwidth of the probing light. Nevertheless, the transmission values tend to correspond.

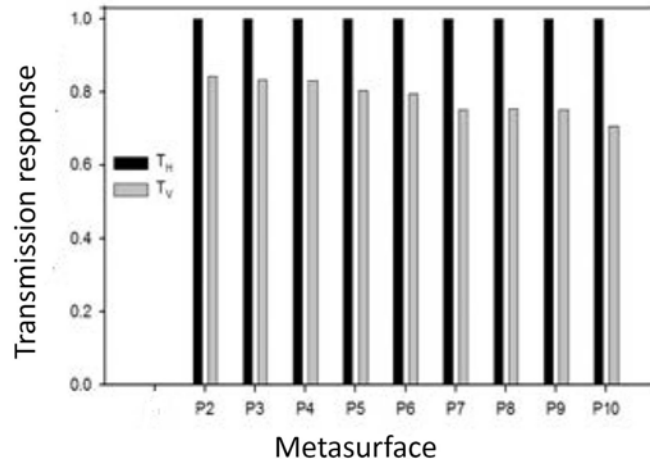


Figure 3.10: Transmission coefficients of horizontally (black) and vertically (grey) polarised single photons (at 810 nm) through different plasmonic metamaterials (nanorods with $w = 39$ to 47 nm, $l = 110$ nm, $t = 30$ nm) obtained via experiment. The nanorod widths increase from left to right.

In order to further investigate metamaterial P10 in the quantum regime we probe it with six polarisation-encoded single photon states: $|H\rangle$, $|V\rangle$, $|+\rangle$, $|-\rangle$, $|L\rangle$ and $|R\rangle$. The fidelity $F = \langle \phi | \rho_{exp} | \phi \rangle$ and purity $P = \text{tr}(\rho_{exp}^2)$ [74] were then calculated for the output states ρ_{exp} obtained using quantum state tomography [113]. We use maximum likelihood estimation and Monte Carlo simulation. Here, $|\phi\rangle$ is the ideal input quantum state and the fidelity provides a measure of the closeness of the output state to the ideal input state. The purity provides a measure of how close the output state is to a pure state. In figures 3.11 to 3.14 we show the real and imaginary parts of the density matrices for four different probe states ($|H\rangle$, $|V\rangle$, $|+\rangle$ and $|L\rangle$) sent through either the substrate or metamaterial P10. We obtained a fidelity of 0.960 ± 0.002 and a purity of 0.950 ± 0.007 for the probe state $|H\rangle$ transmitted through the substrate, and a fidelity of 0.97 ± 0.003 and a purity of 0.956 ± 0.007 for the state $|H\rangle$ transmitted through the metamaterial. The fidelity and purity of all six probe states are given in table 3.1. The data used for reconstructing the density matrices were raw data obtained from the experiment. One can see in figures 3.11 and 3.12 ((a) and (b)) that the $|H\rangle$ and $|V\rangle$ states are transmitted through the

metamaterial in the same way as the substrate, although with fewer photons detected for $|V\rangle$. One can also see from figures 3.13 and 3.14 that the vertical component of the state is reduced slightly when the state is sent through the metamaterial, as expected. This will be studied in more detail next when we include temperature effects also.

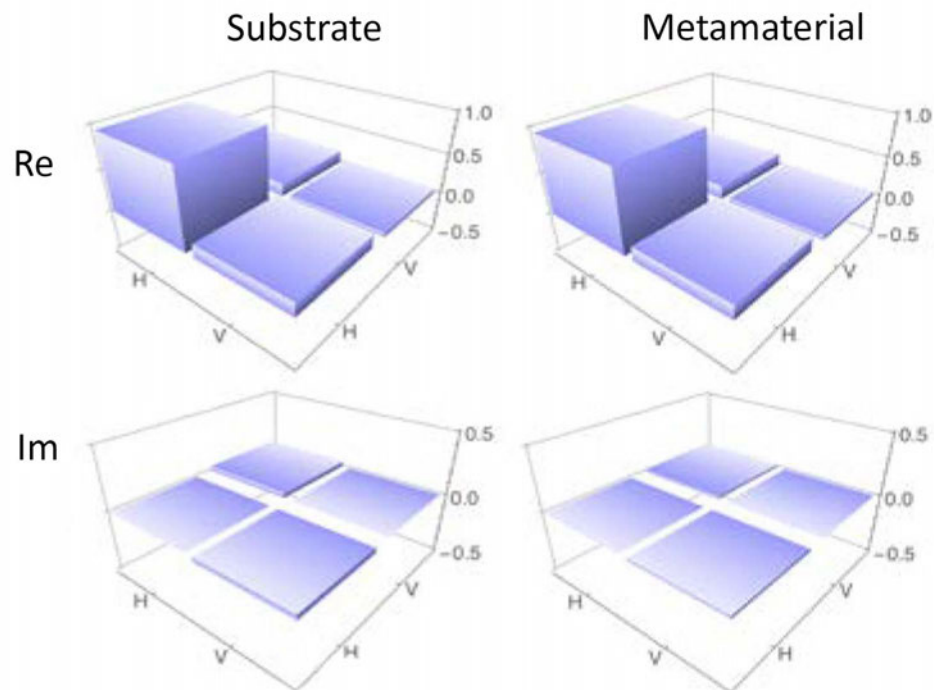


Figure 3.11: Quantum state tomography of probe states sent through the substrate and metamaterial. Real and imaginary parts of the output state ρ_{exp} obtained from the state $|H\rangle$ sent through the substrate and metamaterial.

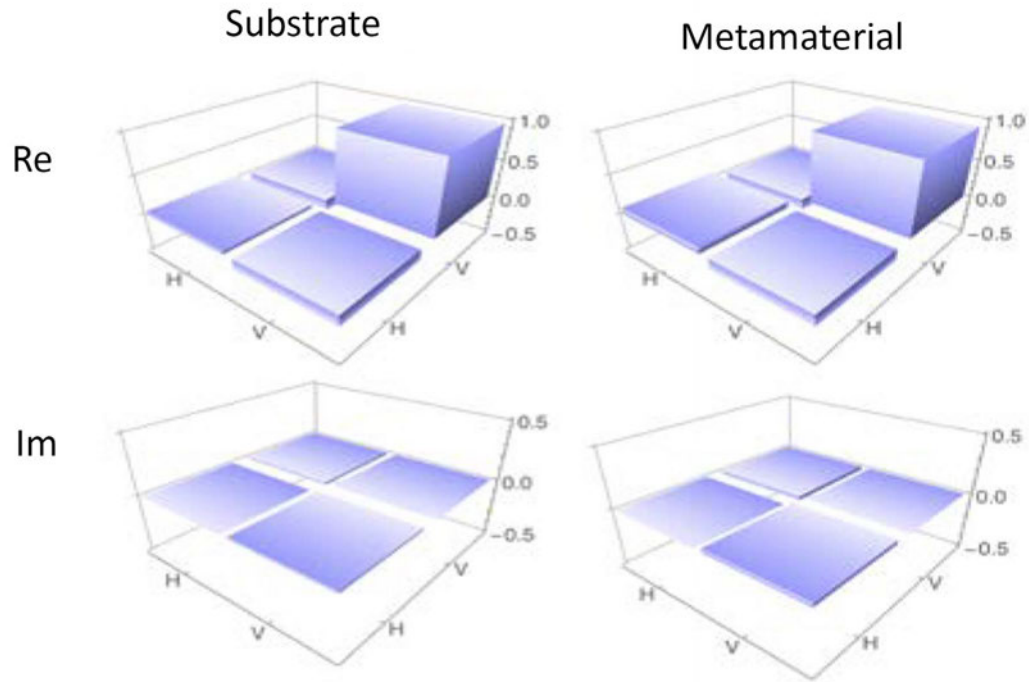


Figure 3.12: Quantum state tomography of probe states sent through the substrate and metamaterial. Real and imaginary parts of the output state ρ_{exp} obtained from the state $|V\rangle$ sent through the substrate and metamaterial.

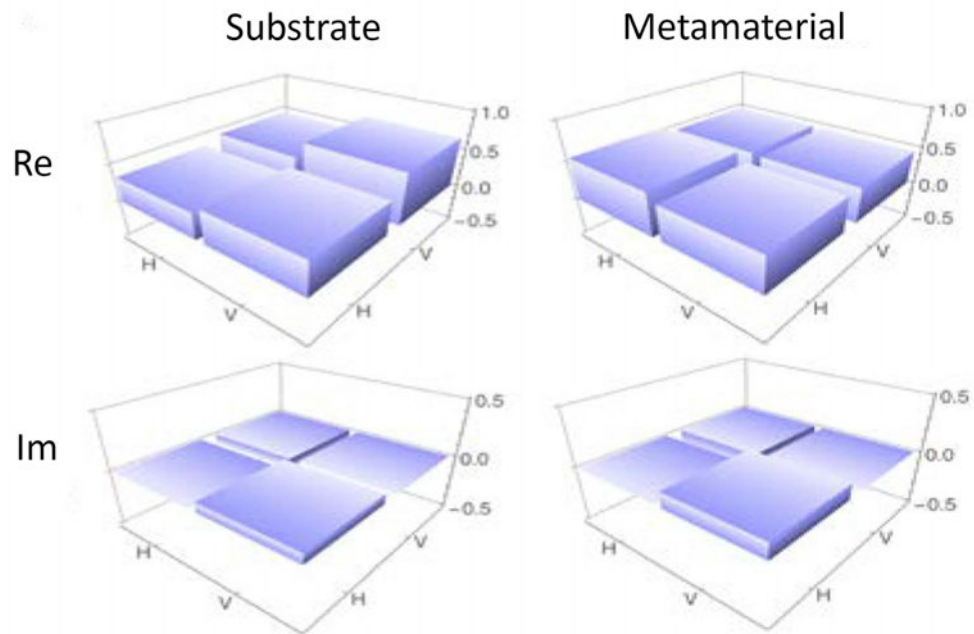


Figure 3.13: Quantum state tomography of probe states sent through the substrate and metamaterial. Real and imaginary parts of the output state ρ_{exp} obtained from the state $|+\rangle$ sent through the substrate and metamaterial.

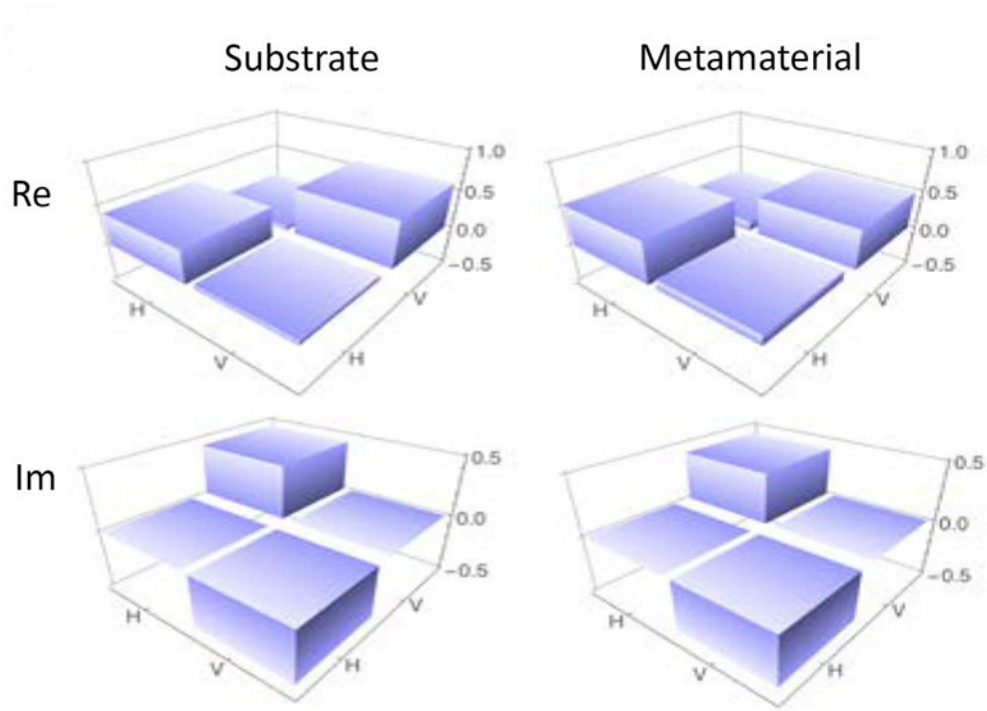


Figure 3.14: Quantum state tomography of probe states sent through the substrate and metamaterial. Real and imaginary parts of the output state ρ_{exp} obtained from the state $|L\rangle$ sent through the substrate and metamaterial.

Table 3.1: Fidelity and purity for the single-photon probe states. The error bars here and elsewhere are obtained from a 100 run Monte Carlo simulation which uses the collected data and adds Poissonian noise on the counts, as this is the main source of noise in down-conversion experiments.

State	Fidelity		Purity	
	Substrate	Metamaterial	Substrate	Metamaterial
$ H\rangle$	0.960 ± 0.002	0.970 ± 0.003	0.950 ± 0.007	0.956 ± 0.003
$ V\rangle$	0.960 ± 0.002	0.928 ± 0.003	0.954 ± 0.004	0.925 ± 0.007
$ +\rangle$	0.940 ± 0.003	0.960 ± 0.002	0.946 ± 0.006	0.968 ± 0.005
$ -\rangle$	0.950 ± 0.003	0.910 ± 0.003	0.953 ± 0.006	0.987 ± 0.007
$ R\rangle$	0.924 ± 0.003	0.925 ± 0.003	0.912 ± 0.006	0.954 ± 0.006
$ L\rangle$	0.938 ± 0.003	0.929 ± 0.003	0.938 ± 0.002	0.934 ± 0.005

3.5 Temperature dependence of a plasmonic metamaterial in the quantum regime: Experiment

In this section, we present the experimental results of single photon transmission through plasmonic metamaterials at different temperatures. We begin this section by presenting the experimental setup.

3.5.1 Experimental setup

A diagram of the scenario for demonstrating the active control of a metamaterial in the quantum regime is shown in figure 3.15 with the temperature control unit included. Here a single-photon (red beam) and an external control laser for heating (white beam) are incident on the metamaterial. The inset shows the geometry of the nanorods in each unit cell. In figure 3.15(b) the optical setup used is shown. Here, single photons are again generated using type-1 SPDC. Pairs of single photons at $\lambda = 810$ nm are produced at angles $\pm 3^\circ$ when a photon from a pump laser at 405 nm is incident on a nonlinear crystal [135, 134]. The pump laser (200 mW) is rotated to vertical polarization by a half-wave plate (HWP) and incident on the crystal (0.5 mm thickness). A single photon from the pump produces two twin (idler and signal) horizontally polarized photons. One photon is produced in arm A and the other in arm B. The detection of a single photon in arm A using a single-photon detector (Excelitas SPCM-AQRH-15) heralds the presence of a single photon in arm B within an 8-ns coincidence window. A qubit is encoded onto the single photon in arm B using a quarter-wave plate (QWP) and a HWP. The polarization states $|H\rangle$ and $|V\rangle$ are used as the orthogonal basis states of the qubit as before. This qubit is then sent through the plasmonic metamaterial, after which the state of the qubit is measured via a projective measurement using a QWP, a HWP, and a single-photon detector [113]. A broadband external control laser (Fianium WhiteLase micro) is used to vary the temperature of the metamaterial by heating it with a range of laser powers.

In order to quantify the performance of the metamaterial as a quantum channel at different temperatures, quantum state tomography is carried out on the output states of four different polarization-encoded qubits $\{|H\rangle, |V\rangle, |+\rangle, |L\rangle\}$ sent through, with the density matrices reconstructed via projective measurements [113]. The output of a given projective measurement is sent to a single-photon detector and a coincidence between the detector in the heralding arm A and the detector in arm B is measured. In order to reduce the impact of the broadband nature of the photons on the transmission response of the metamaterial (see eg. Figure 3.1) we reduce the bandwidth of the single photons from 40nm to 10nm, without affecting significantly the photon detection rate. Interference filters (810 ± 5 nm) are placed in front of each detector to cut out photons of higher and lower frequencies corresponding to unwanted down-conversion processes and the pump beam, leading to ~ 1000 coincidences per second (for $|H\rangle$ encoded and $|H\rangle$ measured). The more narrow bandwidth also reduces the possible variance in the transmission of the metamaterial, as seen in Figure 3.1, giving a more consistent result with respect to the theory. The density matrices obtained from quantum state tomography of the four probe states are then used to reconstruct the quantum channel of the metamaterial via quantum process tomography [74, 136], the details of which are discussed later. The data used for reconstructing the density matrices were raw data obtained from the experiment. Three different plasmonic metamaterials were used in this study, each with a specific set of dimensions for the gold nanorod unit cells. The samples were fabricated by collaborators in the group of Prof. Martin Wegener at the Karlsruhe Institute of Technology in Germany. The metamaterials were fabricated on an Indium Tin Oxide (ITO) coated fused silica substrate by electron-beam lithography. A 5-nm thin layer of ITO was deposited on a 5×5 mm² silica substrate by electron-beam evaporation and then a 200-nm-thick film of polymethylmethacrylate photoresist (MicroChem) was spin coated on top of the ITO. Using electron beam writing (Raith e-line), the photoresist was patterned and then developed, leaving a mask. Subsequent gold evaporation and lift-off produced the gold

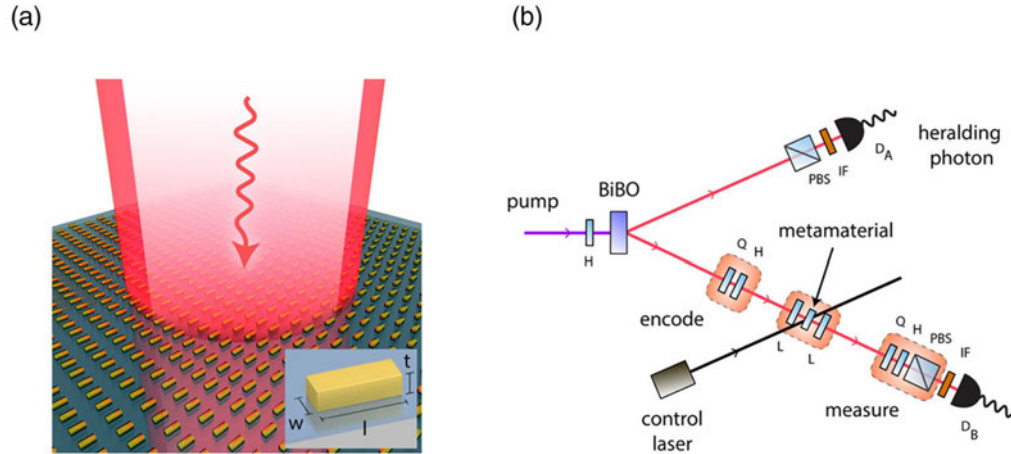


Figure 3.15: Overview and experimental setup for demonstrating active control of a metamaterial in the quantum regime. (a) Pictorial representation of one of the metamaterials used with a single photon (red) and an active control laser beam (white) sent through. The spot size of the control and single-photon beams are the same in the experiment; however, the control beam is shown smaller for pictorial purposes. The inset shows a three-dimensional figure of the nanorods in each unit cell (dimensions considered are given in the main text). (b) Experimental setup, where a nonlinear BiBO crystal is pumped at 405 nm, producing pairs of photons at 810 nm via spontaneous parametric down-conversion. One photon is detected at detector D_A and heralds the presence of a single photon in the other arm. Here H is a half-wave plate, Q is a quarter-wave plate, L is a plano-convex lens ($f = 25$ mm), PBS is a polarizing beam splitter, IF is an interference filter ($\lambda = 810$ nm and $\Delta\lambda = 10$ nm), and D_A and D_B are single-photon detectors.

nanorod antenna arrays for the different metamaterials, each with an area of $100 \times 100 \mu\text{m}^2$. The nanorods have a period of 200 nm, a thickness of 30 nm, a width between 50 and 70 nm, and a length between 100 and 130 nm. Specific dimensions of a given metamaterial are provided later. The full $5 \times 5 \text{ mm}^2$ metamaterial sample consisting of an array of metamaterials with different nanorod sizes is placed inside a telescope system (figure 3.9 (b)) designed in such a way that the beam before and after the (plano-convex) lenses ($f = 25$ mm) is collimated and the beam between the lenses is focused to a spot size with diameter $\lesssim 100 \mu\text{m}$.

3.5.2 Results and discussion

We now analyze our experimental results in light of the theoretical model described previously. Here, each of the three metamaterials used has different nanorod dimensions for the unit cells, as shown in the atomic force microscope (AFM) images in figure 3.17 (a), 3.18 (a) and 3.19 (a). The resolution of the AFM is $\sim 5\text{nm}$. The general trend in dimensions is the same as that used in the theoretical model, i.e., the length and width increase when going from figure 3.17 (a) to figure 3.19 (a). Due to the background dielectric material not completely encompassing the nanorods, as well as the presence of the ITO bonding layer and differences in the permittivity of gold, it is not possible to obtain an exact fit of our theoretical model to the experimental transmission data. However, the general trend seen in the experimental classical transmission results of figures 3.17 (b), 3.18 (b) and 3.19 (b) matches, as seen in the theoretical model of figures 3.5 (a) to 3.6 (a) and 3.7 (a) at 300 K, also taking into account broadening due to the fabrication process. A more refined theory model is needed here, however this is challenging to develop due to the non-symmetric nature of the ‘nanorod on substrate’ metamaterial samples, ie. the background dielectric material not completely encompassing the nanorods. However, this would be a fruitful direction for further work. The dimensions measured by the AFM are $w \simeq 50\text{ nm}$ and $l \simeq 100\text{ nm}$ for figure 3.17 (a), $w \simeq 60\text{ nm}$ and $l \simeq 110\text{ nm}$ for figure 3.18 (a), and $w \simeq 70\text{ nm}$ and $l \simeq 130\text{ nm}$ for figure 3.19 (a). The thickness of the nanorods is 30 nm. Figure 3.16 (a) shows the transmission results for these exact dimensions. The difference to the measured values (seen in Figures 3.17, 3.18 and 3.19) highlights how the basic theory model does not match the experiment so well. As the AFM values have an accuracy of 5nm and the theory model is highly sensitive to small changes in the dimensions, as seen in Figure 3.8, the dimensions used in the theory model in the previous section were chosen to be different to the AFM values, with the corresponding transmissions shown in Figure 3.16 (b). The main consideration in deviating from the AFM values was to ensure the wavelength of the resonance peaks roughly matched. To what extent the geometric asymmetry of the unit

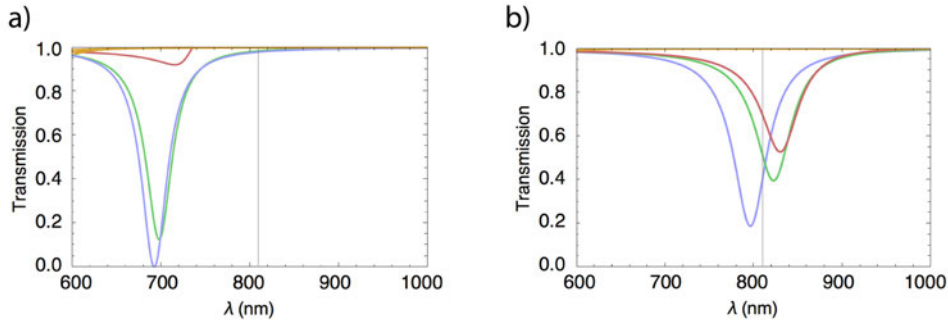


Figure 3.16: Theory and experiment compared.

cells also plays a role in shifting the resonance is an open question requiring a rigorous finite element simulation.

In figure 3.17 (c) to 3.19 (c) we show the transmission results of probing the metamaterials with single photons in the state $|V\rangle$ in arm B as the temperature is increased. Here the transmission is given by the ratio of heralded detection counts (coincidences) when the state $|V\rangle$ is sent through the metasurface and counts when it is sent through the substrate only (no metasurface). It represents the relative probability for a photon in the state $|V\rangle$ to be transmitted through the metamaterial. The data obtained is normalized by the same amount of time integration. The temperature is changed by increasing the power of the control laser in four steps, from 0 to 200 mW, which heats up the metamaterial. The area illuminated by the laser beam is ~ 2 mm in diameter. The time between the control laser activation and the start of measurements is 480 s for each temperature; however, a steady-state response is reached within 240 s (the state at which the transmission was constant over time). For quantum applications such as entanglement distillation [62, 137], this response time is practical as it is much shorter than the time scale on which birefringent fluctuations would occur in a realistic optical fiber quantum network [138]. The response time could be made shorter, if needed for a given application, using alternative heating methods [139, 140, 141]. The control laser was placed at an angle to the normal of the metamaterial to avoid any scattered light reaching the detectors. This

was carefully monitored throughout the experiment. Control via the laser power gives five different temperature settings: $T_0 = 295$ K, $T_1 = 303$ K, $T_2 = 319$ K, $T_3 = 331$ K, and $T_4 = 347$ K, consistent with the range used in the theoretical model. The values are spaced apart by approximately 10 K and are determined by the power set by the control laser software. They are measured using a point-probe temperature sensor placed close to the laser beam on the metasurface sample. Measurements are carried out at the steady state response time and the error in the values is less than 1 K, consistent with ambient temperature fluctuations. Due to the small size of each metamaterial array ($100 \times 100 \mu\text{m}$) it was not possible to measure the spatial homogeneity of the temperature, however the laser beam has an area much larger than the array and so it covers the entire array. Thus the temperature is expected to be roughly constant over the metamaterial.

At $T = T_0$, one can see in figures 3.17 (c) to 3.19 (c) that the photon transmission slightly deviates from that of the classical transmission measured using vertically polarized light at $\lambda = 810$ nm, as shown in figures 3.17 (b) to 3.19 (b). This deviation can be attributed to the spot size of the beam; in the classical case the spot is smaller and easier to align on the metasurface using a CCD camera, whereas in the single-photon case the spot size is comparable to the metasurface and alignment is achieved by optimizing single-photon detection counts. As a result there is some nonideal overlap of the beam and the metamaterial. Regardless of this, the trend of the single-photon transmission at T_0 matches that of the classical case as the nanorod dimensions increase. Moreover, as the temperature increases one can see the effect on the transmission of $|V\rangle$ states for the three metamaterials considered. The largest change is seen for the first metamaterial, shown in figure. 3.17 (c), where the transmission changes from 0.48 to 0.32, corresponding to a percentage change of 33%. The percentage changes for the other two metamaterials are 14% and 5%. We also measured the transmission of $|H\rangle$ states through the metamaterials as the temperature was changed and found that the transmission remained roughly the same as when the states were sent through the substrate only. The exact transmission

values of the $|H\rangle$ state, as well as those of the additional probe states $|+\rangle$ and $|L\rangle$, are combined with the values obtained for the $|V\rangle$ state to obtain a full characterization of the metamaterial as a variable single-qubit quantum channel. The transmission values are part of a larger set of projective measurements which we use for quantum process tomography [136, 74] at the five different temperatures and discussed in detail next.

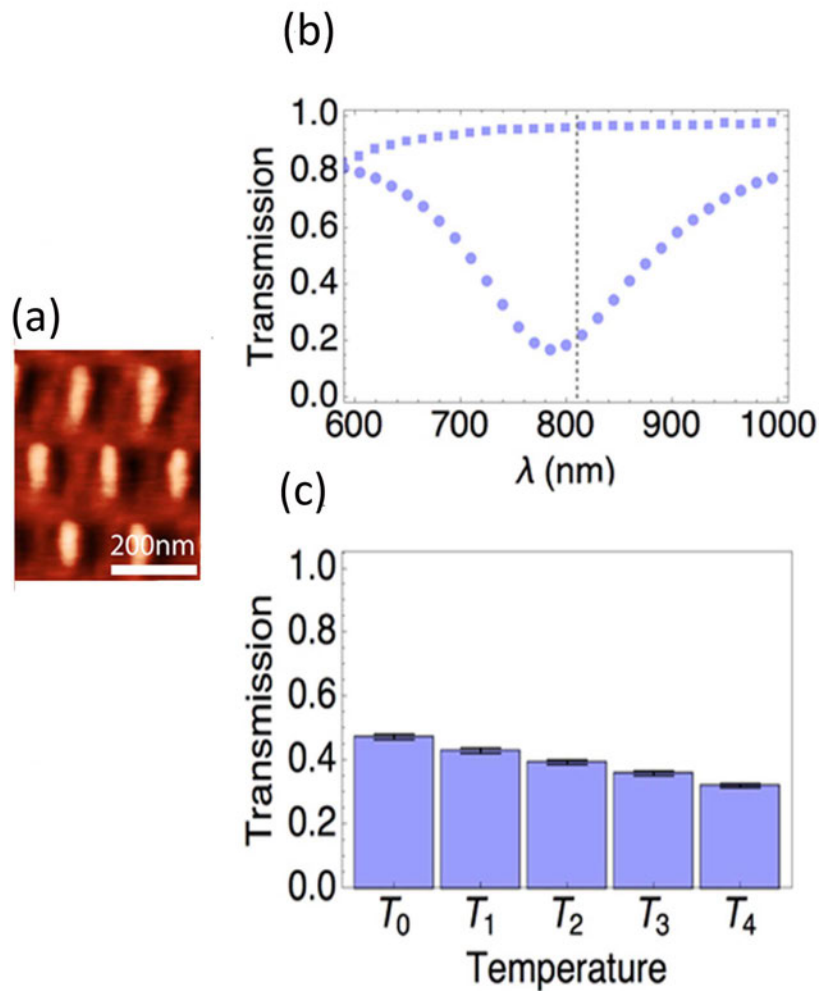


Figure 3.17: Temperature-dependent transmission response of a metamaterial (experiment). (a) Atomic force microscope image. See the main text for dimension details. (b) Classical transmission spectra of the metamaterial at T_0 for horizontal (squares) and vertical (circles) polarized light. The spectra was measured using frustrated total internal reflection (FTIR). (c) Transmission probabilities in the quantum regime for single qubits encoded into the vertical polarization of single photons as $|V\rangle$ and sent through the metamaterials as the temperature is changed. The five different temperature settings are $T_0 = 295$ K, $T_1 = 303$ K, $T_2 = 319$ K, $T_3 = 331$ K, and $T_4 = 347$ K, corresponding to values consistent with the range used in the theoretical model. The values are determined by the laser power used and are spaced apart by approximately 10 K

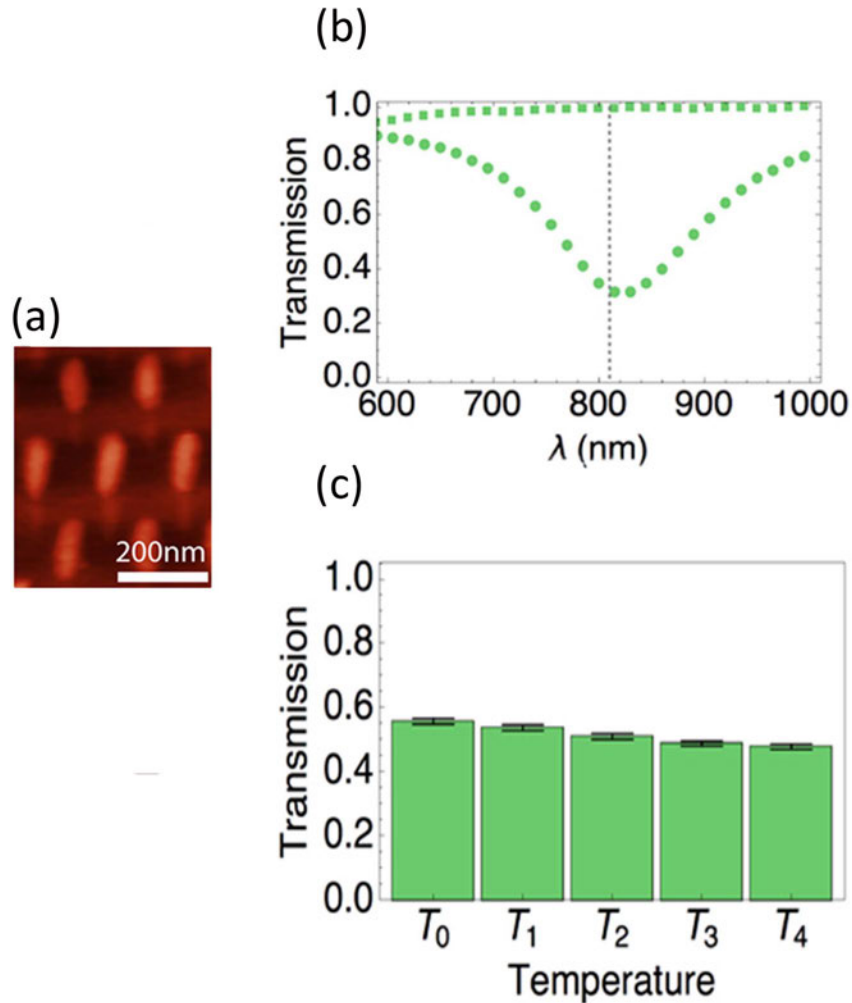


Figure 3.18: Temperature-dependent transmission response of a metamaterial (experiment). (a) Atomic force microscope image. See the main text for dimension details. (b) Classical transmission spectra via FTIR of the metamaterial at T_0 for horizontal (squares) and vertical (circles) polarized light. (c) Transmission probabilities in the quantum regime for single qubits encoded into the vertical polarization of single photons as $|V\rangle$ and sent through the metamaterials as the temperature is changed. The five different temperature settings are $T_0 = 295$ K, $T_1 = 303$ K, $T_2 = 319$ K, $T_3 = 331$ K, and $T_4 = 347$ K, corresponding to values consistent with the range used in the theoretical model. The values are determined by the laser power used and are spaced apart by approximately 10 K

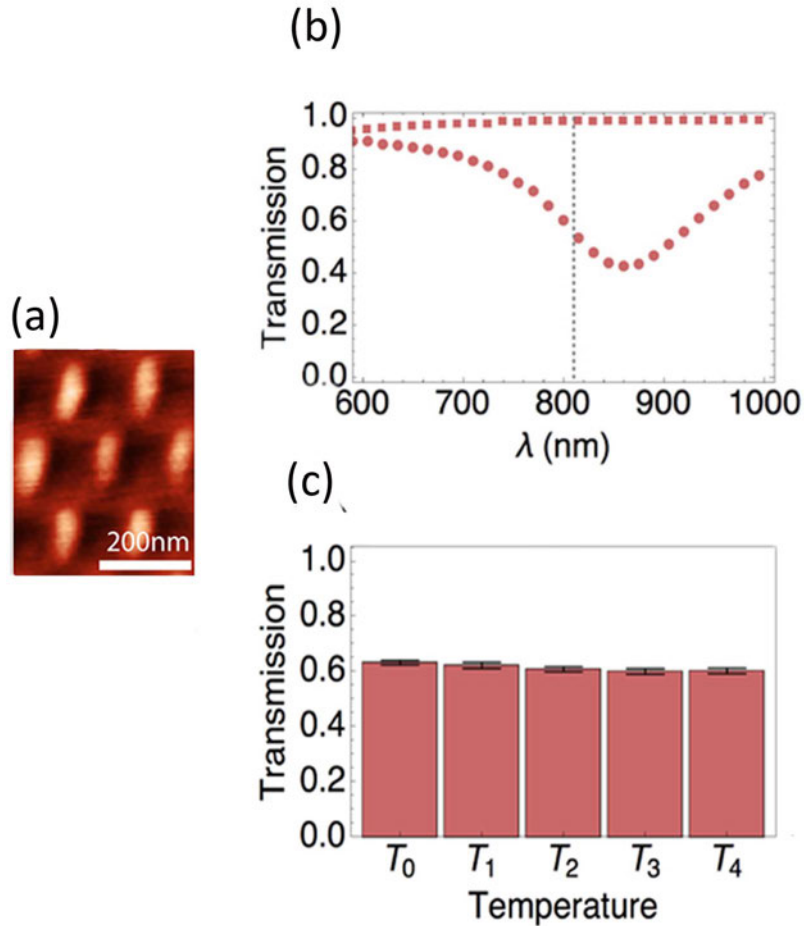


Figure 3.19: Temperature-dependent transmission response of a metamaterial (experiment). (a) Atomic force microscope image. See the main text for dimension details. (b) Classical transmission spectra via FTIR of the metamaterial at T_0 for horizontal (squares) and vertical (circles) polarized light. (c) Transmission probabilities in the quantum regime for single qubits encoded into the vertical polarization of single photons as $|V\rangle$ and sent through the metamaterials as the temperature is changed. The five different temperature settings are $T_0 = 295$ K, $T_1 = 303$ K, $T_2 = 319$ K, $T_3 = 331$ K, and $T_4 = 347$ K, corresponding to values consistent with the range used in the theoretical model. The values are determined by the laser power used and are spaced apart by approximately 10 K

The four probe states sent through the metamaterial in the quantum process tomography are $|H\rangle$, $|V\rangle$, $|+\rangle$, and $|L\rangle$. From projective measurements on the outputs of these states in the bases $|H/V\rangle$, $|+/-\rangle$, and $|R/L\rangle$ we reconstructed their density matrices using quantum state tomography [113]. Using the density matrices, we then obtained the quantum process matrices, or χ matrices, for the three different metamaterials in our investiga-

tion [136] (details are given in chapter 2). The polarization response of the metamaterials is such that they act as partial polarizers and are well represented by a single Kraus operator $K_0 = |H\rangle \langle H| + \sqrt{T_V} |V\rangle \langle V|$ corresponding to a non-trace-preserving channel [62], i.e., $\rho \rightarrow K_0 \rho K_0^\dagger$, where ρ is the qubit of the input single-photon state in the polarization basis. This channel is equivalent to the general quantum channel $\rho \rightarrow \sum_{ij} \chi_{ij} E_i \rho E_j^\dagger$, where the single-qubit Pauli operators $E_i = I, X, Y,$ and Z provide a complete basis for the Hilbert space and the elements of the χ matrix are set to values that allow the general channel to completely match the action of K_0 [62].

The χ matrix obtained for the first metamaterial at T_0 is shown in figure 3.20 (a) and 3.20 (c). Figure 3.20 (a) shows the real part and 3.20 (c) shows the imaginary part. The real and imaginary parts of an ideal partial polarizer matrix χ_{id} with $T_V = 0.476$ are shown in 3.20 (b) and 3.20 (d), respectively. The value of T_V has been found using the process fidelity $F_P(T_V) = \text{tr}(\sqrt{\sqrt{\chi} \chi_{id} \sqrt{\chi}})^2 / \text{tr}(\chi) \text{tr}(\chi_{id})$, which quantifies how close the experimental channel is to an ideal channel of a partial polarizer. We find a maximum of $F_P(T_V) = 0.935 \pm 0.008$ at $T_V = 0.476 \pm 0.008$, which shows that the metamaterial represents well a partial polarizer for single photons with a T_V value consistent with the single-photon transmission measured previously [see figure 3.17 (c)]. The χ matrix for the first metamaterial at T_4 is shown in figures 3.21 (a) and 3.21 (c). Figure (a) shows the real part and figure (c) shows the imaginary part. The real and imaginary parts of an ideal partial polarizer matrix with $T_V = 0.324$ are shown in 3.21 (f) and 3.21 (h). The value of T_V has again been found by maximizing the process fidelity, with a value of $F_P = 0.897 \pm 0.005$. The process fidelities and corresponding T_V values extracted for all three metamaterials at all temperatures are given in Table 3.2. All process fidelities are above 89%, with T_V consistent with the values measured previously [see figures 3.17 (c) to 3.19 (c)], showing that the metamaterials act as variable partial polarizers in the quantum regime. As a result, they can be used to induce a temperature-controlled collective polarization-dependent loss at the single-photon level for quantum information tasks, such as entanglement distillation [62].

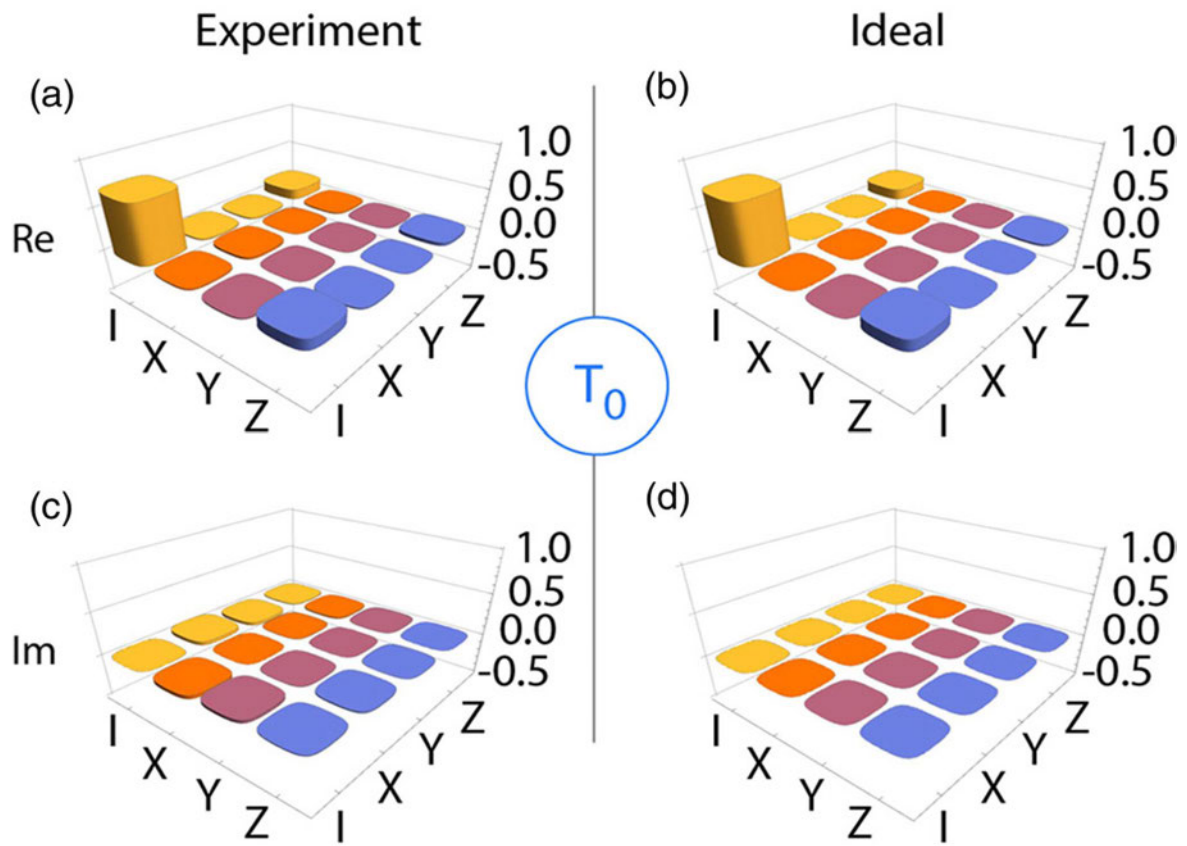


Figure 3.20: Quantum process tomography χ matrices for the first metamaterial at the reference temperature (T_0). (a) and (c) Real and imaginary parts of the experimental χ matrix at T_0 . (b) and (d) Real and imaginary parts of an ideal partial polarizer χ matrix with $T_V = 0.476$.

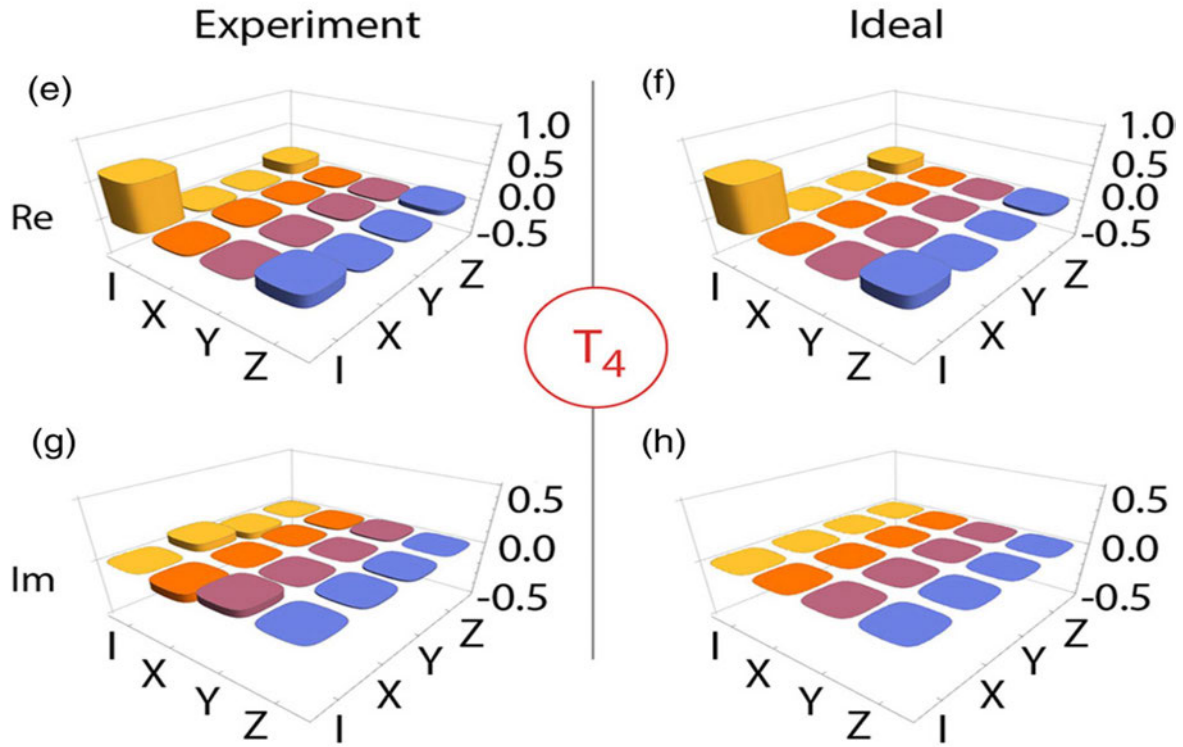


Figure 3.21: Quantum process tomography χ matrices for the first metamaterial at the final temperature (T_4). (a) and (c) Real and imaginary parts of the experimental χ matrix at T_4 . (b) and (d) Real and imaginary parts of an ideal partial polarizer χ matrix with $T_V = 0.476$.

Table 3.2: Process fidelities for the three metamaterials investigated as the temperature is changed, as well as horizontal and vertical transmission probabilities T_H and T_V extracted from maximizing the process fidelity, respectively. The error bars here and elsewhere are obtained from a 100 run Monte Carlo simulation which uses the collected data and adds Poissonian noise on the counts, as this is the main source of noise in down-conversion experiments.

	M ₁			M ₂			M ₃		
Temp	F_P	T_H	T_V	F_P	T_H	T_V	F_P	T_H	T_V
T ₀	0.935 ± 0.007	1	0.476 ± 0.008	0.909 ± 0.012	1	0.560 ± 0.009	0.895 ± 0.009	1	0.634 ± 0.008
T ₁	0.899 ± 0.006	1	0.433 ± 0.008	0.935 ± 0.006	1	0.540 ± 0.009	0.922 ± 0.007	1	0.624 ± 0.011
T ₂	0.899 ± 0.006	1	0.397 ± 0.007	0.934 ± 0.008	1	0.513 ± 0.009	0.942 ± 0.009	1	0.610 ± 0.009
T ₃	0.922 ± 0.005	1	0.362 ± 0.007	0.948 ± 0.008	1	0.491 ± 0.008	0.970 ± 0.006	1	0.602 ± 0.010
T ₄	0.897 ± 0.005	1	0.324 ± 0.006	0.912 ± 0.006	1	0.481 ± 0.008	0.939 ± 0.009	1	0.604 ± 0.010

Chapter 4

Markovian and non-Markovian quantum channels

4.1 Introduction

The study of open quantum systems is key to understanding fundamental issues in quantum physics, as well as for developing technological applications, such as quantum communication and computing. Realistic quantum systems interact and exchange information with their environment. In most cases, such an interaction results in the loss of information from the system due to its weak coupling to the environment. This information loss is called decoherence. Thus, quantum decoherence is the loss of quantum information (coherence). The term decoherence was first coined by German physicist H. D. Zeh, in 1970 [142], and since 1980 the field has grown rapidly with a large interest from researchers involved in quantum computing and quantum information processing.

A quantum system combined with its environment evolves with a unitary evolution. The concept of decoherence and the flow of information between a quantum system and its environment has made it possible to study some important and interesting quantum dynamics. For example, the control of entanglement and quantum phases in many-body

systems [143, 144], driving quantum computation by dissipation [145], controlling the transition from Markovian dynamics to a regime with quantum memory effects (non-Markovian) [146], and to create quantum system simulators [147]. However, the concept of decoherence has almost always been treated within the framework of Markovianity (i.e Markov process) and non-Markovianity. A Markovian process is a stochastic process whereby the conditional probability of the future state depends only on the present state and is independent of any state that preceded it. A Markovian process is sometimes called a memoryless quantum channel or process. On the other hand, a non-Markovian process is a process that does not demonstrate the Markov property. This type of process is sometimes called a memory process. Markovian and non-Markovian processes are usually described based on quantum dynamical maps, whereby system-environment interactions (described by unitary transformations) are properly studied. Figure 4.1 shows a simple representation of a system-environment interaction. The time-dependent unitary transformation describing such an interaction from initial time t_0 to final time t can be written as

$$\rho_S(t) = \text{tr}_E[U(t, t_0)(\rho_S(t_0) \otimes \rho_E(t_0))U(t, t_0)^\dagger], \quad (4.1)$$

where $U(t, t_0)$ is the unitary operation for the system-environment dynamics and $(\rho_S(t_0) \otimes \rho_E(t_0))$ is the assumed uncorrelated system and environment initially. The dynamics of the system alone, excluding the environment can be written using a superoperator $\Lambda(t, t_0)$, known as a system propagator

$$\Lambda(t, t_0)(\rho_S(t_0)) = \text{tr}_E[U(t, t_0)(\rho_S(t_0) \otimes \rho_E(t_0))U(t, t_0)^\dagger] = \rho_S(t) \quad (4.2)$$

where $\Lambda(t, t_0)$ acts only on the system $\rho_S(t_0)$ resulting in an open system, $\rho_S(t)$. For the evolution of the system to be physical, the system propagator (i.e $\Lambda(t, t_0)$) must be trace-preserving and completely positive. The system propagator can also be described using the Kraus representation

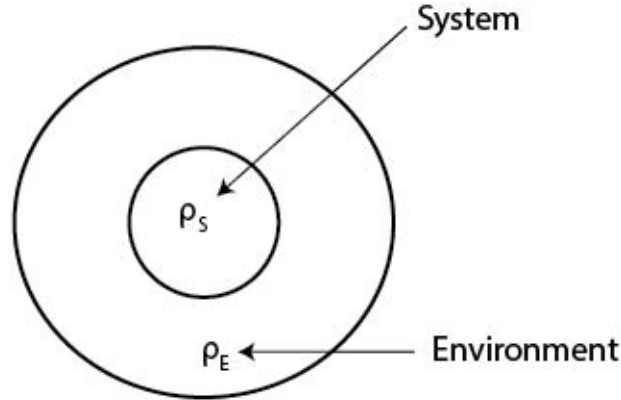


Figure 4.1: Representation of a system-environment time-dependent unitary transformation. The entire system is 'closed', but the dynamics of the system alone can be described using open quantum system techniques.

$$\Lambda(\rho_S) = \sum_i A_i \rho_S A_i^\dagger = \sum_{m,n} \chi_{mn} E_m \rho_S E_n^\dagger, \quad (4.3)$$

where $\sum_i A_i A_i^\dagger = \mathbf{1}_S$ and χ_{mn} is the normal χ matrix. If Eq. 4.3 is satisfied, then Λ is a quantum channel. In this chapter we will discuss the theory of Markovian and non-Markovian processes and how these processes can be realised experimentally. We also discuss how to construct a non-Markovian process from the summation of two Markovian processes (that is, two semi-group dynamical maps), and vice-versa. The chapter ends with the experimental realisation of a Markovian process from the sum of two non-Markovian processes, and vice-versa.

4.2 Markovian Quantum channels

Markovianity has attracted a lot of attention recently due to its applications in quantum information processing. In classical stochastic processes, the theory of Markovianity is fully developed but in quantum evolution, still remains vague and not well understood.

Consider the following open system dynamics having the following system propagators

of the form

$$\Lambda(t_2, t_0) = \Lambda(t_2, t_1)\Lambda(t_1, t_0) \quad \text{with } \Lambda(t_0, t_0) = \mathbb{1} \quad \text{for all } t_2 \geq t_1 \geq t_0 \quad (4.4)$$

If Eq. 4.4 is satisfied by any time parameters, then the corresponding family of operators/propagators is called an evolution family (EF). Thus an EF of quantum channels is an EF for which $\Lambda(t_f, t_i)$ is a quantum channel for all $t_f \geq t_i \geq 0$. The family of the system propagators are called a one-parameter semigroup (OPSG) if the following conditions are met

$$\Lambda(r)\Lambda(s) = \Lambda(r + s) \quad \text{for all } r, s \geq 0, \quad (4.5)$$

where $\Lambda(0) = \mathbb{1}$, r and s represent time differences. Thus, a OPSG of quantum channels is then a OPSG for which $\Lambda(s)$ is a quantum channel for all $s \geq 0$. Under very general mathematical conditions such a semigroup, if it is uniformly continuous ($t \rightarrow \Lambda(t)$ is continuous), has a generator \mathcal{L} which allows us to write

$$\Lambda(r) = e^{\mathcal{L}r}, \quad (4.6)$$

where \mathcal{L} is a time-independent generator. Eq. 4.6 satisfies the semigroup law

$$\Lambda(r)\Lambda(s) = \Lambda(r + s) = e^{(r+s)\mathcal{L}}. \quad (4.7)$$

From Eq. 4.6, the system can be reduced to

$$\frac{d\rho_s(t)}{dt} = \mathcal{L}(\rho_s(t)). \quad (4.8)$$

$\mathcal{L}(\rho_s(t))$ is a generator of a OPSG of quantum channels which obeys the Gorini-Kossakowski-

Sudarshan-Lindblad (GKSL) master equation of the form

$$\mathcal{L}(\rho_s(t)) = -i[H, \rho_s(t)] + \sum_k \gamma_k [L_k \rho_s(t) L_k^\dagger - \frac{1}{2} \{L_k^\dagger L_k, \rho_s(t)\}_+], \quad (4.9)$$

where H is time-independent and Hermitian, γ_k is a positive number, and L_k are the Lindblad operators. The evolution of an open quantum system according to Eq. 4.9 is known as Markovian semi-group dynamics. The generator \mathcal{L} may also be time-dependent for a more general case for an EF of quantum channels if it is denoted by

$$\mathcal{L}(t)(\rho_s(t)) = -i[H(t), \rho_s(t)] + \sum_k \gamma_k(t) [L_k(t) \rho_s(t) L_k^\dagger(t) - \frac{1}{2} \{L_k^\dagger(t) L_k(t), \rho_s(t)\}_+], \quad (4.10)$$

with $\Lambda(t, s) = e^{\int_s^t \mathcal{L}(t') dt'}$ as a general EF channel and not a OPSG channel. Eq. 4.10 is a time-dependent master equation and follows from the same Markovian approximations as the time-independent case, when derived from a microscopic model.

4.2.1 Non-Markovian process from two Markovian processes

We discuss in this section how a non-Markovian process can be obtained from two Markovian processes. Consider the following dynamical map for a single qubit

$$\Lambda_t = \frac{1}{2}(\Lambda_t^{(x)} + \Lambda_t^{(y)}), \quad (4.11)$$

where we use a subscript t for time for ease of notation and $\Lambda_t^{(k)} = e^{\mathcal{L}_k t}$, with $\mathcal{L}_k(\rho) = c(\sigma_k \rho \sigma_k - \rho)$, where $k = x, y$. The parameter c is a rate that describes the time scale on which the dynamics take place. We then have

$$\Lambda_t^{(k)}(\rho) = \frac{1}{2}(1 + e^{-2ct})\rho + \frac{1}{2}(1 - e^{-2ct})\sigma_k \rho \sigma_k, \quad (4.12)$$

and so,

$$\Lambda_t(\rho) = \frac{1}{2}(1 + e^{-2ct})\rho + \frac{1}{4}(1 - e^{-2ct})(\sigma_x\rho\sigma_x + \sigma_y\rho\sigma_y) \quad (4.13)$$

Eq. 4.13 is a convex sum of two Markovian semigroup dynamics and because Markovian and non-Markovian channels do not form a convex set it may no longer be possible to write $\Lambda_t = e^{\mathcal{L}t}$ for some time-independent \mathcal{L} . In general, we can write Λ_t as

$$\Lambda_t = e^{\int_0^t \mathcal{L}_\tau d\tau}, \quad (4.14)$$

with $\mathcal{L}_t(\rho) = \sum_j \gamma_j(t)\mathcal{L}_j(\rho)$. In this case, we have

$$\mathcal{L}_t(\rho) = \sum_{k=x,y,z} \gamma_k(t)(\sigma_k\rho\sigma_k - \rho), \quad (4.15)$$

with $\gamma_x = \gamma_y = \frac{c}{2}$ and $\gamma_z = -\frac{c}{2}\tanh(ct)$. Now, if we consider a single-qubit in the Bloch sphere denoted by $\rho = \frac{1}{2}(\mathbb{I} + \sum_{x,y,z} x_k\sigma_k)$, we can then have

$$\Lambda_t(\rho) = \frac{1}{2}(\mathbb{I} + \sum_{k=x,y,z} \lambda_k(t)x_k\sigma_k) \quad (4.16a)$$

$$\Lambda_t^{(x)}(\rho) = \frac{1}{2}(\mathbb{I} + \sum_{k=x,y,z} v_k(t)x_k\sigma_k) \quad (4.16b)$$

$$\Lambda_t^{(y)}(\rho) = \frac{1}{2}(\mathbb{I} + \sum_{k=x,y,z} \mu_k(t)x_k\sigma_k) \quad (4.16c)$$

where $\lambda_x(t) = \frac{1}{2}(1 + e^{-2ct})$, $v_x(t) = 1$, $\mu_x(t) = e^{-2ct}$, $\lambda_y(t) = \frac{1}{2}(1 + e^{-2ct})$, $v_y(t) = e^{-2ct}$, $\mu_y(t) = e^{-2ct}$, $\lambda_z(t) = e^{-2ct}$, $v_z(t) = e^{-2ct}$ and $\mu_z = e^{-2ct}$. Figure 4.2 shows the time-dependent probability $p(t) = \frac{1}{2}(1 + e^{-2ct})$ for applying σ_x and σ_y at different times for $c = \frac{1}{2}$.

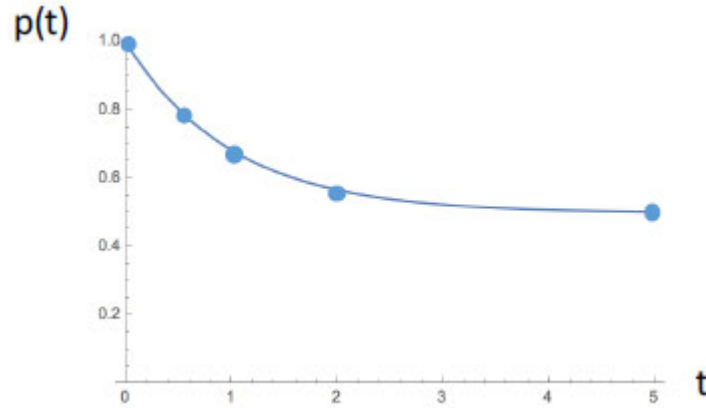


Figure 4.2: Time dependent probability for application of σ_x and σ_y in Eq. 4.12. The points at various times represent possible times at which the channels could be realized for.

4.2.2 Determining Markovianity

While the combined map can be written in the form given in Eq. 4.14, this form includes both Markovian and non-Markovian dynamics. The evolution of a dynamical map Λ_t is Markovian if and only if it can be denoted as

$$\Lambda_t = V_{t,s}\Lambda_s, \quad t \geq s \quad (4.17)$$

where $V_{t,s}$ is a completely positive (CP) operator. The dynamics of Eq. 4.17 is completely positive divisible and we have $V_{t,s} = \Lambda_t\Lambda_s^{-1}$. One may decide to check if it is a CP map directly by calculating Λ_s^{-1} for a given Λ_s and multiplying it by Λ_t to get $V_{t,s}$. In general, this is challenging. As a result, a method based on a transfer matrix approach is more helpful [148]. We start by constructing a transfer matrix F that is isomorphic with a dynamical map Λ_t

$$F_{\alpha,\beta}(t) = \text{tr}(G_\alpha^\dagger \Lambda_t(G_\beta)), \quad (4.18)$$

where $\{G_\alpha\}$ is a set of n orthonormal operators with $n = 2$ for a qubit (for example, the pauli operators including \mathbb{I}). From Eq. 4.18, we then have

$$\Lambda_t(\rho) = \sum_{\alpha,\beta=1}^{n^2} F_{\alpha,\beta}(t) G_\alpha \text{tr}(G_\beta^\dagger \rho). \quad (4.19)$$

Thus, if we choose unit matrices $G_\alpha = |k\rangle\langle\ell|$ with $\alpha = (k, \ell)$, then we can relate F to the Choi matrix W as

$$W(t) = \frac{1}{n} \sum_{\alpha,\beta=1}^{n^2} F_{\alpha,\beta}(t) G_\beta \otimes G_\alpha, \quad (4.20)$$

where $W(t) = (\mathbb{I} \otimes \Lambda_t)P_+$, with $P_+ = |\psi_+\rangle\langle\psi_+|$ and $|\psi_+\rangle = \frac{1}{\sqrt{n}} \sum_{i=0}^{n-1} |i\rangle \otimes |i\rangle$. The dynamical map Λ_t is completely positive and trace preserving (CPTP) if and only if the corresponding Choi matrix $W(t)$ is positive and $\text{tr}(W(t)) = 1$. While, one can simply use Λ_t to get $W(t)$ for a single map and check CPTP, our interest is in linking two maps Λ_t and Λ_s via the propagator $V_{t,s}$ and checking if Λ_t is Markovian or non-Markovian via Eq. 4.17. In light of this, for two maps Λ_A and Λ_B , the transfer matrices can be multiplied to get the total transfer matrix so that

$$F(t) = F(t, s)F(s) \quad \rightarrow \quad F(t, s) = F(t)F^{-1}(s), \quad (4.21)$$

where $F(t, s)$ corresponds to Λ_A and $F(s)$ corresponds to Λ_B . The transfer matrix $F(t, s)$ is associated with the propagator $V_{t,s}$ and if it yields a positive Choi matrix $W(t, s)$ for all $t \geq s$, then Λ_t is Markovian (that is, $V_{t,s}$ is CP and therefore Λ_t is CP-divisible). To check for positivity of $W(t, s)$ it is enough to calculate its eigenvalues. Finding $F^{-1}(s)$, $F(t)$ and therefore $F(t, s)$, then obtaining $W(t, s)$ and checking positivity is easier than finding Λ_s^{-1} and checking $V_{t,s}$ for CP. If $F(s)^{-1}$ does not exist, then the map is immediately identified as indivisible and therefore non-Markovian. The above criteria can be applied to the example given in the previous section. We will discuss this in more detail in the next section and shows that the combination of two Markovian channels leads to a non-Markovian channel.

4.3 non-Markovian quantum channels

In general, non-Markovianity has been broadly defined if and only if the dynamical map Λ_t is indivisible [149], or if there is a form of back-flow of information from the environment to the system, leading to some form of memory effect [150]. For example, if the evolution of the quantum system evolves via an EF that is not an EF of quantum channels, then we can call the EFs indivisible and they may lead to memory effects. An EF of a system propagator is indivisible if there exist some $t_f \geq t_i \geq 0$ for which $\Lambda(t_f, t_i)$ is not a quantum channel. It is important to note that, if an indivisible EF is not completely positive then it is not physical.

4.3.1 Markovian process from two non-Markovian process

In a similar fashion to getting a non-Markovian process from two Markovian processes, we can also sum up two non-Markovian processes to give a Markovian process.

To get a Markovian process from the sum of two non-Markovian processes, we consider the following channel

$$\Lambda_t = p\Lambda_t^1 + (1-p)\Lambda_t^2 \quad (4.22)$$

where $\Lambda_t^1(\rho) = p_1(t)\rho + [1 - p_1(t)]\sigma_x\rho\sigma_x$ and $\Lambda_t^2(\rho) = p_2(t)\rho + [1 - p_2(t)]\sigma_x\rho\sigma_x$ are non-Markovian channels with time-dependent probabilities p given by

$$p_1(t) = \frac{3}{2}\left[\frac{1}{2}(1 + e^{-t}) - \frac{1}{3}\cos^2(t)\right] \quad (4.23)$$

$$p_2(t) = \cos^2(t). \quad (4.24)$$

Using the above equations, we can then write Eq. 4.22 as

$$\Lambda_t = \frac{1}{2}(1 + e^{-t})\rho + \frac{1}{2}(1 - e^{-t})\sigma_x\rho\sigma_x \quad (4.25)$$

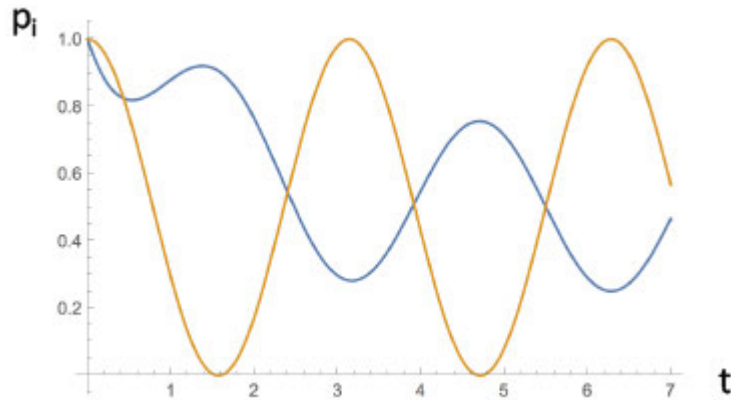


Figure 4.3: Time-dependent probabilities p_1 and p_2 .

where $p = \frac{2}{3}$. $\Lambda_t(\rho)$ is a typical damping channel and Markovian for $p=2/3$. Figure 4.3 shows the time-dependent probabilities p_1 and p_2 .

4.4 Experimental setup/procedure

Figure 4.4 (a) shows the type-1 SPDC source [134, 135] used in the experiment. A pump laser at 405 nm is rotated to vertical polarisation by a half-wave plate (HWP). The pump beam is then sent through a non-linear BiBO crystal, which produces two ‘twin’ (idler and signal) photons polarised horizontally at a lower frequency (wavelength 810 nm). One photon is produced in arm A and the other in arm B. The optical axis of the BiBO is cut such that the two photons emerge at 3° from the initial pump direction. A single photon in arm A is used to herald the presence of another single photon in arm B.

A Mach-Zehnder interferometer was then constructed and placed in arm B of the SPDC source, as shown in figure 4.4 (a) in order to create two channels. Here, the top arm of the interferometer is called the top channel while the bottom arm of the interferometer is called the bottom channel. A qubit is encoded into the single-photon in arm B using a quarter-wave plate (QWP) and a half-wave plate (HWP) before the interferometer. Here, the polarisation states $|H\rangle$ and $|V\rangle$ are used as the orthogonal basis states of the qubit. Note that the interferometer was not set up to interfere the two channels, but simply

combine them. This means that the two channels are taken together as a probabilistic summation. Thus, entangled states are not generated. Eq. 4.22 shows the theory of the summation of the two channels. The p values are implemented by varying the occurrence of waveplates in the top and bottom channels. The operation $\mathbb{1}$ or σ_x ($\mathbb{1}$ or σ_y) for the top (bottom) channel is carried out using the waveplates set at the angles shown in Figure 4.4. Note that here only the half waveplate needs to be rotated to carry out the two different operations. Thus, the half wave plates are put in automatic wave plate rotators. The relative occurrence of $\mathbb{1}$ or σ_x ($\mathbb{1}$ or σ_y) over a total of 100 half waveplate settings is fixed by the value of p . For instance, if $p=0.5$ then there is an equal chance of $\mathbb{1}$ or σ_x being implemented during the 100 settings. State tomography is carried out during the time when the waveplate rotators have stopped rotating - which we call the dwell time. For the case of the joint channel, where both the top and bottom channels are combined, the wave plate rotators operate independently, but the dwell times are made to coincide so that the collection of counts is done equally via both channels. The state tomographies for a fixed value of p for all the probe states are then combined, so that the chi matrix for a given p can be reconstructed. Probe states $|H\rangle, |V\rangle, |+\rangle$ and $|L\rangle$ are encoded and sent through the top, bottom and joint channels. For the case of realising a non-Markovian process from two Markovian process, the relative occurrence (determined by p) of $\mathbb{1}$ and σ_x for the top channel and $\mathbb{1}$ and σ_y for the bottom channel (see section 4.2.1) is achieved via the rotation of waveplates in either channel. For the case of realising a Markovian process from two non-Markovian process, $\mathbb{1}$ and σ_x are used on both the top and bottom channels (see section 4.3.1). The top channel consists of a QWP, HWP and QWP arranged in series as shown in figure 4.4 b (i). Figure 4.4 b (ii) shows the waveplates angles used for the $\mathbb{1}$ and σ_x operations. The bottom channel has a QWP, QWP and HWP arranged in series as shown in figure 4.4 c (i) and their corresponding waveplate rotation angles in figure 4.4 c (ii). For each probe state sent through, state tomography is carried out at the measurement stage. The state tomographies are then combined to obtain the χ matrix

for the top, bottom and joint channels for a given p . The p values were implemented by automated wave plates placed in both channels. The automated waveplates were rotated and the p values were taking only during dwell times. The quantum process matrices for the top, bottom, and joint channels were obtained via process tomography and we obtained random set of data. The raw data were combined at the interferometer output before quantum process estimation. A list of 100 χ matrices are obtained for each channel and each p .

For a given channel, the χ matrices for two different time pairs (p values $p(s)$ and $p(t)$) are used to obtain the Choi matrices $W(t, s)$ for the channel linking the two times s and t . All permutations of the χ 's are used, leading to 10000 Choi matrices for a given time pair. From the Choi matrices, the distribution of the lowest eigenvalue is obtained, and the mean and standard deviation of these distributions is extracted.

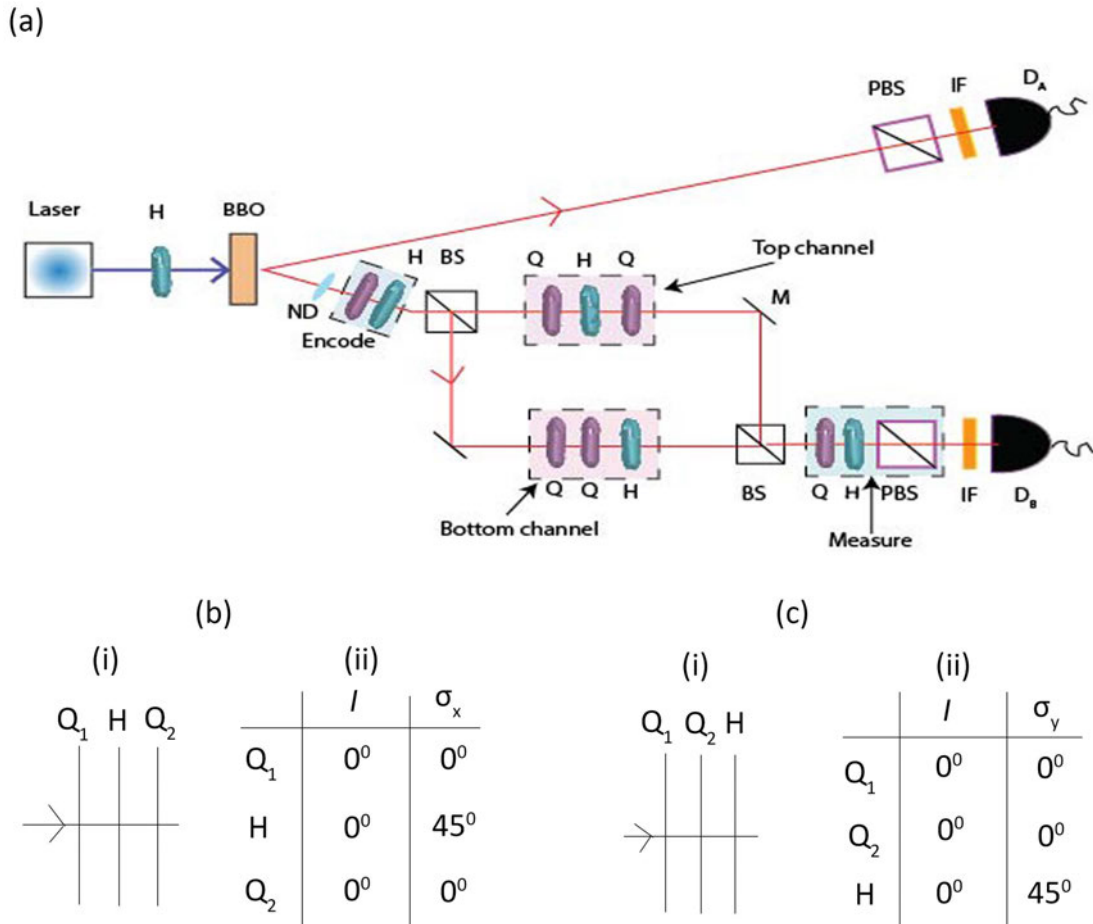


Figure 4.4: Overview and experimental setup for realising Markovian and non-Markovian channels. Experimental setup, where a nonlinear BiBO crystal is pumped at 405 nm, producing pairs of photons at 810 nm via spontaneous parametric down-conversion. One photon is detected at detector D_A and heralds the presence of a single photon in the other arm. Here H is a half-wave plate, Q is a quarter-wave plate, PBS is a polarizing beam splitter, BS is a beam splitter, ND is neutral density filter, IF is an interference filter ($\lambda = 810$ nm and $\Delta\lambda = 10$ nm), and D_A and D_B are single-photon detectors. (b) shows the top channel waveplates and angles settings and (c) shows the bottom channel waveplates and angles settings.

Expected behaviour

Figure 4.5 shows the expected behaviour of the eigenvalues of the Choi matrices for times s to t , for when $t > s$ for the top and bottom channels. It can be seen from the figure that the eigenvalues of the Choi matrices with a smaller value of s have a longer tail.

All eigenvalues are non-negative, indicating Markovian channels. Figure 4.6 shows the expected behaviour for the joint channels. Here, the maximum negative value becomes more negative for larger s . As there is a negative eigenvalue, this indicates the channel is non-Markovian.

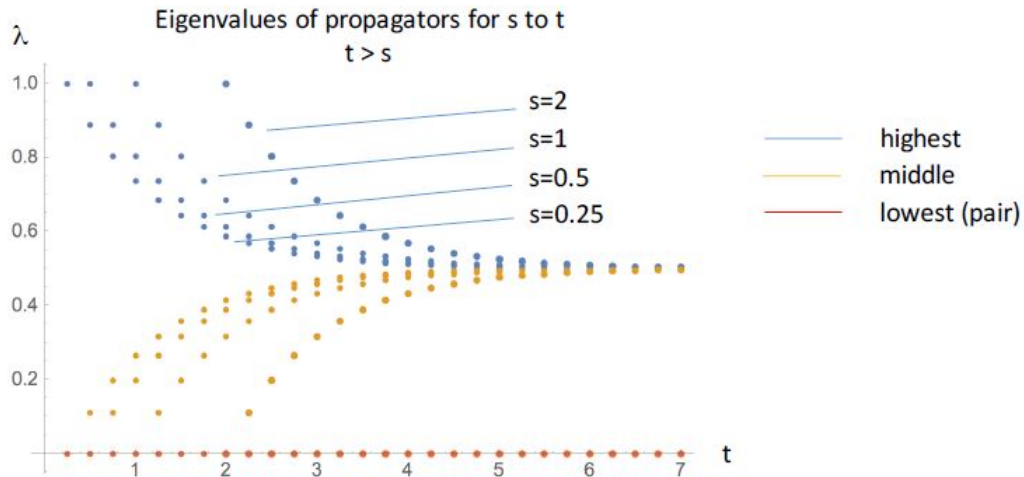


Figure 4.5: Expected behaviour of individual channels: top or bottom (Markovian)

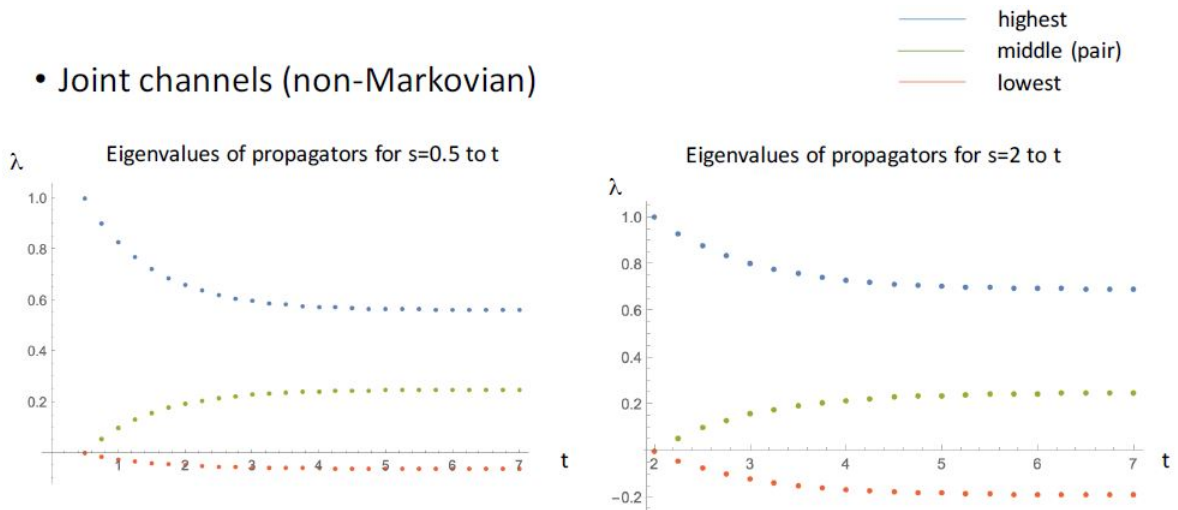


Figure 4.6: Expected behaviour of the joint channel (non-Markovian). Similar behaviour for other starting times s with the maximum negative value becoming more negative for larger s .

For the case of a Markovian process from two non-Markovian processes, the expected behaviour of lowest eigenvalues for the example times $s = 0.6$ and $t = 1.2$ are -0.14

and -0.52, respectively for individual channels. Other times give similar results, with the eigenvalues of the joint channel being non-negative.

4.4.1 Results and discussion

(i) non-Markovian process from two Markovian processes

Quantum process tomography was performed for five different times (0.5, 0.6, 0.75, 2, 2.25). Table 4.1 shows the process fidelity for the top, bottom and joint channels for the various times. We obtained high process fidelities at all times. Figures 4.7 and 4.8 show the eigenvalues of the Choi matrices for the top, bottom and joint channels for times $s = 0.5$ and $t = 0.75$. Similar to the distribution of the lowest eigenvalue, the distributions of all the eigenvalues are skewed towards either higher or lower values (not shown) and not Gaussian for the individual channels (i.e top and bottom channels). For the top channel, we obtained a lowest mean eigenvalue of -0.011 ± 0.004 from the experiment and a zero value from theory. For the bottom channel, we obtained a lowest mean eigenvalue of -0.016 ± 0.007 from experiment and zero value from theory. For the joint channel we obtained a lowest mean eigenvalue of -0.024 ± 0.005 from the experiment and -0.014 from theory. The times 0.5 and 0.75 were chosen because this is near the start of the $p(t)$ curve with a large gradient.

Table 4.1: Process fidelity of the channels for different times for the top, bottom and joint channels.

Time	Top channel	Bottom channel	Joint channels
0.5	0.95 ± 0.01	0.91 ± 0.01	0.95 ± 0.01
0.6	0.95 ± 0.01	0.92 ± 0.01	0.95 ± 0.01
0.75	0.94 ± 0.01	0.92 ± 0.01	0.96 ± 0.01
2	0.95 ± 0.01	0.93 ± 0.01	0.98 ± 0.01
2.25	0.95 ± 0.01	0.94 ± 0.01	0.98 ± 0.01

Figures 4.9 and 4.10 show the eigenvalues of the Choi matrices for the top, bottom and joint channels for times $s = 2$ and $t = 2.25$. For the top channel, we obtained a lowest

mean eigenvalue of -0.042 ± 0.018 from the experiment and a zero value from theory. For the bottom channel we obtained a lowest mean eigenvalue of -0.024 ± 0.011 from the experiment and a zero value from theory. For the joint channel we obtained mean a lowest mean eigenvalue of -0.058 ± 0.020 from the experiment and -0.042 from theory. The times 2 and 2.25 were chosen as this is where the $p(t)$ curve has a smaller gradient and doesn't change much.

We note that the lowest eigenvalues obtained here for the individual channels from the experiment are not zero within the standard deviation as is expected for a Markovian channel. To further understand this discrepancy, we decided to check the mean eigenvalues and standard deviations for ideal photon counts with Poissonian fluctuations (if our experiment was perfect). The mean eigenvalues obtained agree with the ones we obtained from the experiment. For example, for $s = 0.5$ and $t = 0.75$, we obtained a lowest mean eigenvalue of -0.009 ± 0.007 for the top and bottom channels, and -0.015 ± 0.007 for the joint channel as shown in figure 4.11 and figure 4.12. Thus, even if we had an ideal experiment, we would not see a lowest eigenvalue with mean of zero and a Gaussian distribution for the individual channels. Therefore, from the above observation, if the lowest eigenvalue distribution is close enough to zero, with a similar shape to the ideal case, it could be taken as an indication that the individual channels are approximately Markovian. For the joint channel, the mean eigenvalue was clearly negative, which confirms it is non-Markovian.

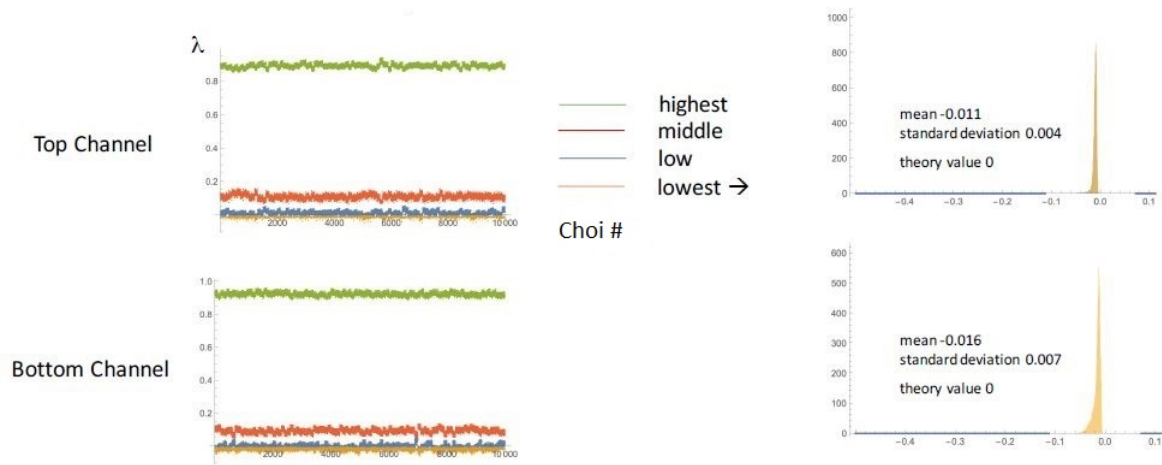


Figure 4.7: Individual channels for times $s = 0.5$ and $t = 0.75$

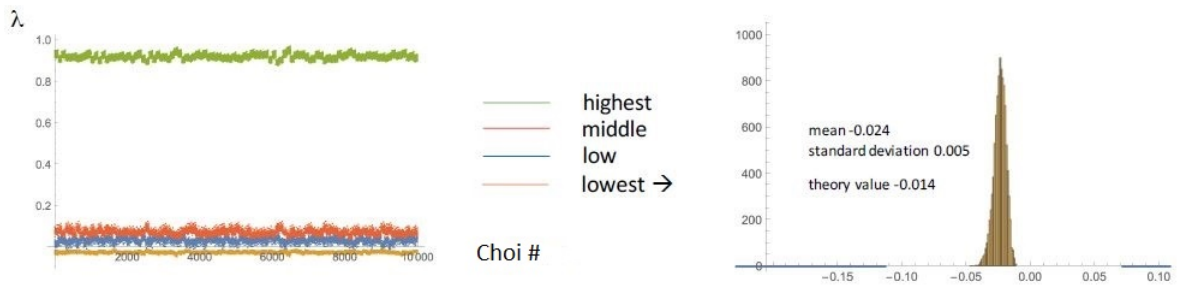


Figure 4.8: Joint channel for times $s = 0.5$ and $t = 0.75$

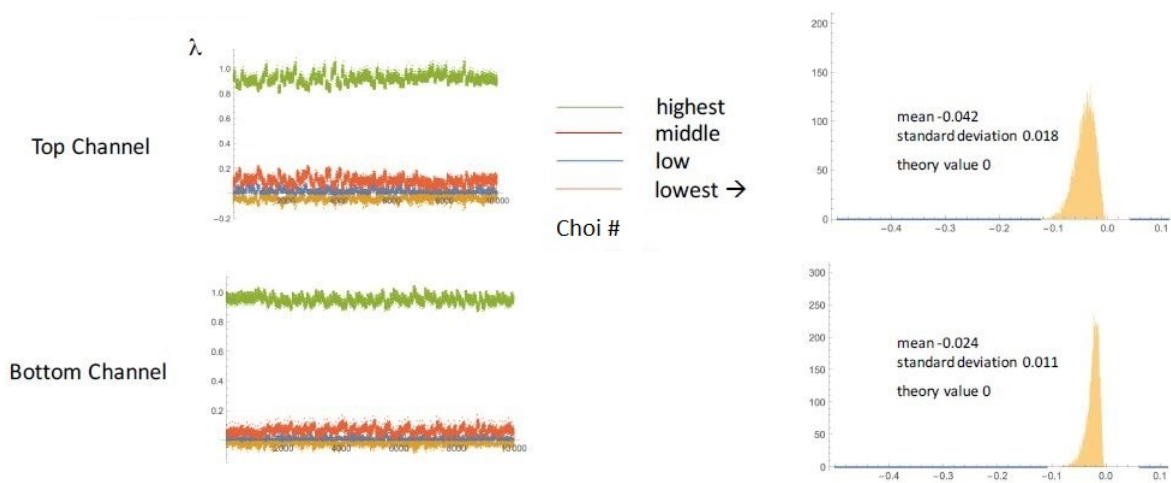
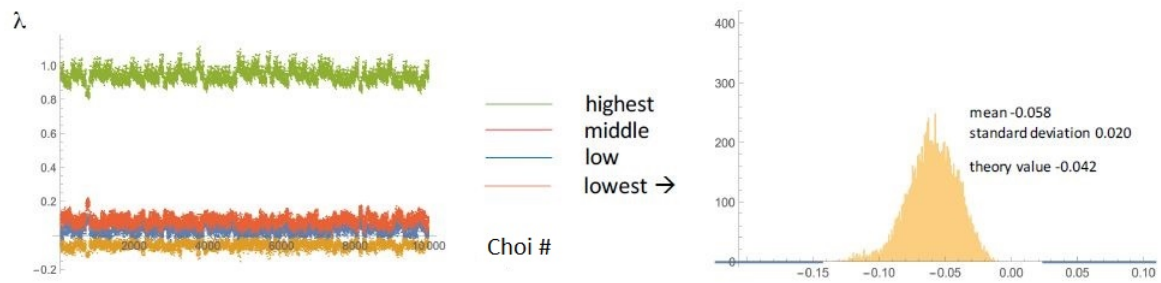
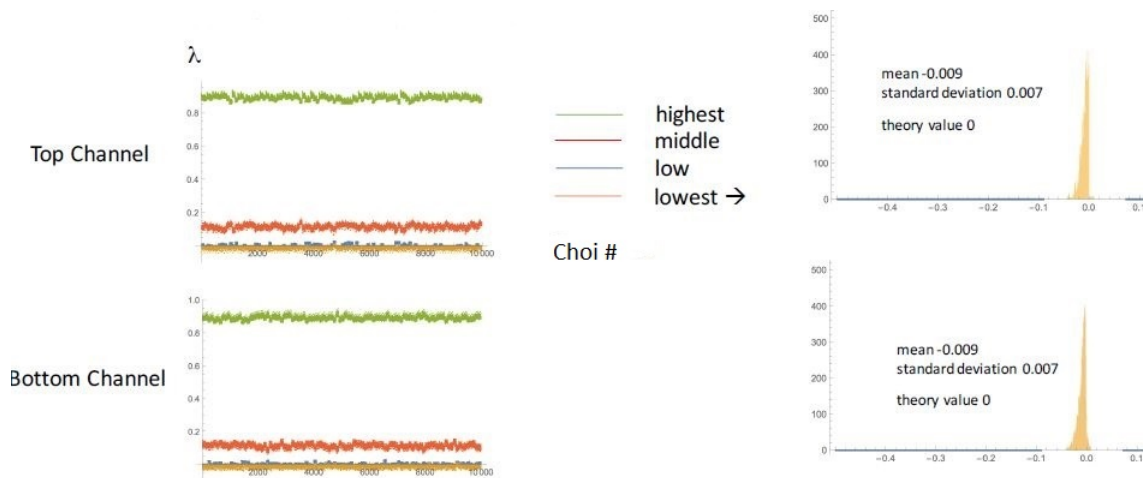
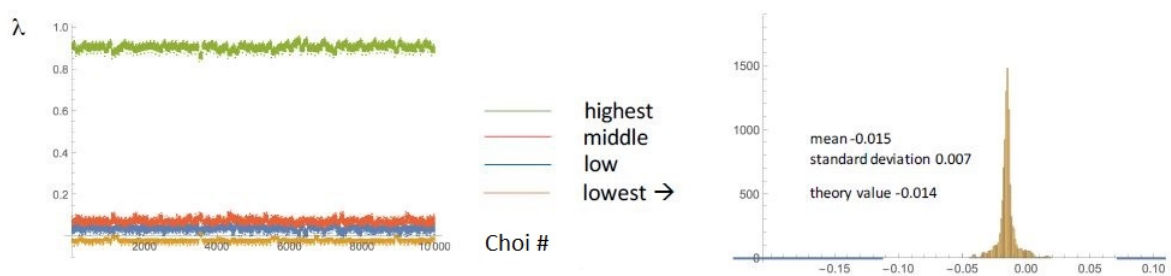


Figure 4.9: Individual channels for times $s = 2$ and $t = 2.25$

Figure 4.10: Joint channel for times $s = 2$ and $t = 2.25$ Figure 4.11: Using ideal counts for top and bottom channels for times $s = 0.5$ and $t = 0.75$ Figure 4.12: Using ideal counts for the joint channel for times $s = 0.5$ and $t = 0.75$

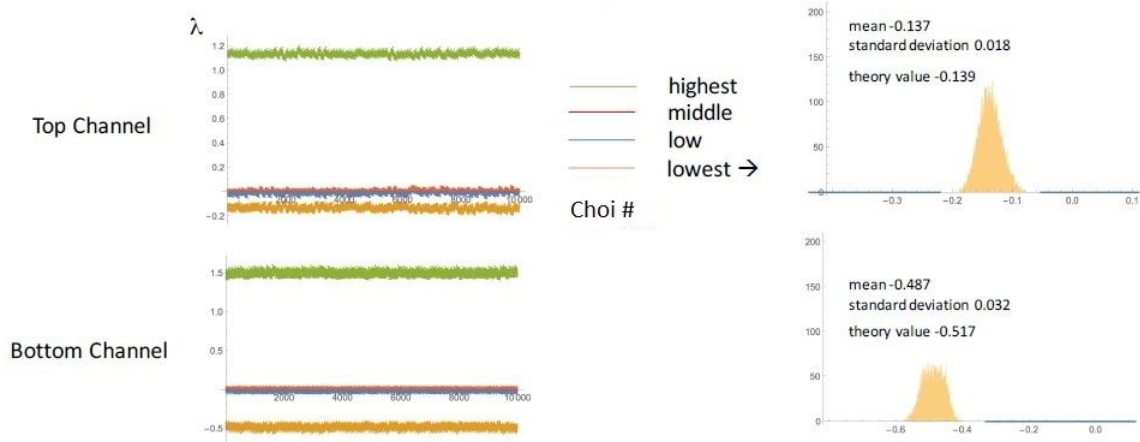
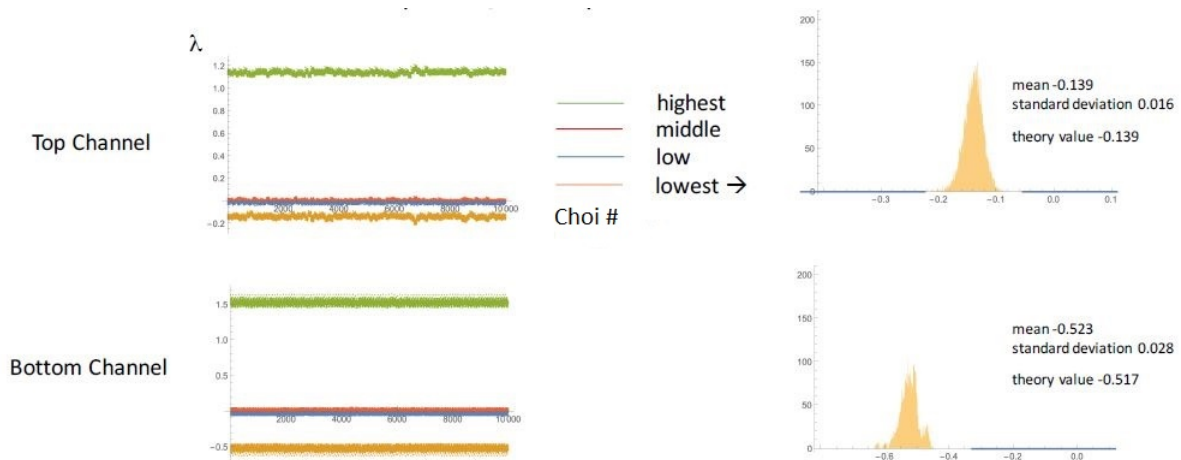


Figure 4.13: Top and bottom channels for time-distribution for $s = 0.6$ and $t = 1.2$

(ii) Markovian process from two non-Markovian processes

In a similar fashion, we performed quantum process tomography for this case at two different times, $s = 0.6$ and $t = 1.2$, and obtained high process fidelities. Table 4.2 shows the process fidelities for the top, bottom and joint channels for the two times. Figures 4.13 and 4.14 show the eigenvalues of the Choi matrices for the top, bottom and joint channels for $s = 0.6$ and $t = 1.2$. For the top channel, we obtained a lowest mean eigenvalue of -0.137 ± 0.018 from the experiment and -0.139 from theory. For the bottom channel, we obtained a lowest mean eigenvalue of -0.487 ± 0.032 from the experiment and -0.517 from theory. For the joint channel we obtained a lowest mean eigenvalue of -0.048 ± 0.009 from the experiment and zero from theory. Clearly, the top and bottom channels are non-Markovian with negative lowest eigenvalues, but a similar effect to that in the previous section is seen again, but this time it is the joint channel where the shape of the distribution is skewed for the lowest eigenvalue. For the joint channel, the eigenvalue is negative but, very close to zero.

Figure 4.14: Both channels combined for times $s = 0.6$ to $t = 1.2$ Figure 4.15: Using Ideal counts for top and bottom channels for times $s = 0.5$ to $t = 0.75$

Just as in the previous section, we checked what eigenvalue distribution ideal photon counts would give. The ideal photon counts appear to agree with what we obtained from the experiment, as shown in figures 4.15 and 4.16. Thus, as already noted previously, even if we had an ideal experiment we would not see a lowest eigenvalue with mean of zero and a Gaussian distribution for the joint channel. As before, one may also consider that if the eigenvalue distribution is close enough to zero and has a similar shape to the ideal case, it could be taken as approximately Markovian. Further work is needed to fine tune the method of using eigenvalues of the Choi matrices as an indicator of Markovian or non-Markovian nature.

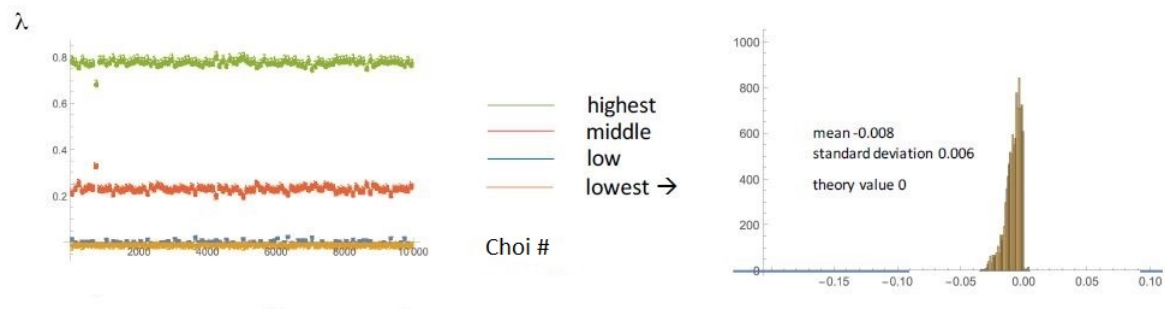
Figure 4.16: Using Ideal counts for both channels combined for times $s = 0.6$ to $t = 1.2$

Table 4.2: Process fidelity at different time-distribution for top, bottom and joint channels.

Time	Top channel	Bottom channel	Joint channels
0.6	0.95 ± 0.01	0.98 ± 0.01	0.89 ± 0.02
1.2	0.95 ± 0.01	0.99 ± 0.01	0.89 ± 0.01

Chapter 5

Conclusion

This thesis looked at ways to experimentally realise different types of quantum channels with the possibility of using them for quantum information processing tasks. We did this by probing and characterising different quantum channels in plasmonic metamaterials and standard optical materials. The fundamental basic tools and techniques needed in the quantum regime to probe quantum channels were discussed at the start in chapter two.

In chapter three, we demonstrated the active control of a plasmonic metamaterial for quantum state engineering. In this chapter, we investigated the active control of a plasmonic metamaterial in the quantum regime via its thermal response. Metamaterials with unit cells made from gold nanorods were probed with polarisation qubits encoded into single photons. We experimentally characterised the plasmonic metamaterial in the quantum regime and showed that the metamaterial behaves like a partial polariser, transmitting the horizontally polarised component of single photons undisturbed and blocking part of the vertically polarised component. The experimental results are in agreement with the theory. The other metamaterials studied showed polarisation dependence for vertically polarised photons according to the dimensions of the nanorods used as unit cells. The transmission of horizontally polarised photons was essentially constant for all metamateri-

als. Using an external laser, we controlled the temperature of the nanorods and substrate. We then carried out quantum process tomography, characterizing the metamaterials as variable quantum channels. It was found that the overall polarization response of the metamaterials can be tuned by up to 33% for particular nanorod dimensions. We used a theoretical model to describe the thermal response of the metamaterials and found that our experimental results matched the predicted behavior well. Our work goes beyond previous studies of simple passive plasmonic systems in the quantum regime and shows that external control of plasmonic elements provides variable metamaterials that can be used for quantum state engineering tasks.

In chapter four, we experimentally probed quantum channels in bulk optical systems. We realised a non-Markovian quantum process from the sum of two Markovian quantum processes and also the reverse of this by obtaining a Markovian process from the sum of two non-Markovian processes. We reported high process fidelities for all the quantum channels observed. For the first channel (i.e the obtaining a non-Markovian process from the sum of two Markovian processes), we reported the eigenvalues of the Choi matrices for different times (0.5, 0.6, 0.75, 2, 2.25). The distributions of the eigenvalues were skewed towards either higher or lower values and not Gaussian. For the second channel (i.e obtaining a Markovian process from the sum of two non-Markovian processes), two different times (0.6 and 1.2) were studied. Again, we found the distributions were skewed and not Gaussian. However, on inspection of the ideal case, there appeared to be similarities between it and the experiment. Further work is needed to understand why the lowest eigenvalues are not at their expected values in the ideal and experimental cases.

Future work and outlook

We are looking at other degrees of freedom of photons for light control using plasmonic metamaterials. We are currently probing orbital angular momentum of light in the quan-

tum regime using a metamaterial. This work is important as it will allow unbounded quantum information transfer, and with the aim of integrating this on-chip device in a plasmonic waveguide. Second, further work is needed to experimentally investigate the propagator method for Markovian and non-Markovian processes in order to understand why the lowest eigenvalues are not at their expected values in the ideal and experimental cases. For example, in the results reported in this thesis, we saw that if the expected channel is Markovian with a zero eigenvalue as the lowest, then the propagator method employed here does not work well. To be more precise, if the expected channel is Markovian and has 2 degenerate eigenvalues that are zero, then one is always made more positive at the expense of the other, which is made more negative. Thus, it is likely that a Markovian channel with only 1 zero eigenvalue (or all positive eigenvalues) would not have this problem.

References

- [1] W. Cai and V. Shalaev. *Optical Metamaterials: Fundamentals and Applications*. Springer Science and Business Media, LLC, New York., 2010.
- [2] <http://www.metamorphose-vi.org/index.php/metamaterials>. Accessed online on 15 May, 2018.
- [3] <https://en.wikipedia.org/wiki/Metamaterial>. Accessed online on 15 May, 2018.
- [4] T. J. Cui, D. R. Smith, and R. Liu. *Metamaterials: Theory, Design and Applications*. Springer Science and Business Media, LLC, New York., 2010.
- [5] R. M. Walser. Electromagnetic metamaterials. *Proc. SPIE Complex Mediums II beyond Linear Isotropic Dielectrics, San Diego, CA, USA*, 4467: 1 – 15, 2001 .
- [6] V. G. Veselago. The electrodynamics of substances with simultaneously negative values of ϵ and μ . *Sov. Phys. Usp*, 10 (4): 509 – 514, 1967.
- [7] J. C. Bose. On the rotation of plane of polarization of electric waves by a twisted structure. *Proc. R. Soc. Lond.*, 63: 146 – 152, 1898.
- [8] W. E. Kock. Metallic delay lenses. *Bell Sys. Tech. J.*, 27: 58 – 82, 1948.
- [9] I. V. Lindell, A. H. Sihvola, J. Kurkijarvi, and K. F. Lindman. The last hertzian, and a harbinger of electromagnetic chirality. *IEEE Antennas Propag. Mag.*, 34: 24 – 30, 1992.

-
- [10] L. Mandlshtam. Group velocity in a crystal lattice. *Zhurn. Eksp. Teor. Fiz. (in Russian. English translation in Sov. Phys. ZETF)*, 15: 476 – 478, 1945.
- [11] G. D. Malyuzhinets. A note on the radiation principle. *Sov. Phys Tech. Phys.*, 21: 940 – 942, 1951.
- [12] W. E. Kock. Metal-lens antennas. *Proc I.R.E. and Waves and Electrons*, 34: 828 – 836, 1946.
- [13] J. Brown. Artificial dielectrics having refractive indices less than unity. *Proc IEE*, 100: 51 – 62, 1953.
- [14] W. Rotman. Plasma simulation by artificial dielectrics and parallel-plate media. *IEE Trans Antennas Propag. AP*, 10: 82 – 95, 1962.
- [15] W. N. Hardy and L. A. Whitehead. Split-ring resonator for use in magnetic-resonance from 200 - 2000 mhz. *Rev. Sci. Instrum.*, 52: 213 – 216, 1981.
- [16] W. Froncisz and J. S. Hyde. The loop-gap resonator - a new microwave lumped circuit electron-spin-resonance sample structure. *J. Magn. Reson.*, 47: 515 – 521, 1982.
- [17] M. M. I. Saadoun and N. Engheta. A reciprocal phase-shifter using novel pseudochiral or omega-medium. *Microw. Opt. Tech.*, 5: 184 – 88, 1992.
- [18] J. S. Hong and M. J. Lancaster. Couplings of microstrip square open-loop resonators for crosscoupled planar microwave filters. *IEEE Trans. Microw. Theory. Tech.*, 44: 2099 – 2109, 1996.
- [19] N. Engheta and R. W. Ziolkowski. *Metamaterials: Physics and Engineering Explorations*. IEEE Press, A John Wiley & Sons, Inc., 2006.
- [20] J. B. Pendry, A. J. Holden, W. J. Stewart, and I. Youngs. Extremely low frequency plasmons in metallic mesostructures. *Phys. Rev. Lett.*, 76: 4773 – 4776, 1996.

-
- [21] J. B. Pendry, A. J. Holden, D. J. Robbins, and W. J. Stewart. Magnetism from conductors and enhanced nonlinear phenomena. *IEEE Trans. Microw. Theory Techn*, 47 : 2075 – 2084, 1999.
- [22] D. R. Smith, W. J. Padilla, D. C. Vier, S. C. Nemat-Nasser, and S. Schultz. Composite medium with simultaneously negative permeability and permittivity. *Phys. Rev. Lett.*, 84: 4184 – 4187, 2000.
- [23] J. B. Pendry. Negative refraction makes a perfect lens. *Phys. Rev. Lett.*, 85: 3966 – 3969, 2000.
- [24] D. R. Smith, J. J. Mock, A. F. Starr, and D. Schurig. Gradient index metamaterials. *Phys. Rev. E*, 71: 036609, 2005.
- [25] J. B. Pendry, D. Schurig, and D. R. Smith. Controlling electromagnetic fields. *Science*, 312: 1780 – 1782, 2006.
- [26] U. Leonhardt. Optical conformal mapping. *Science*, 312: 1777 – 1780, 2006.
- [27] J. D. Baena, R. Marques, and F. Medina. Artificial magnetic metamaterial design by using spiral resonators. *Phys. Rev. B*, 69: 014402, 2004.
- [28] S. Linden, C. Enkrich, M. Wegener, J. Zhou, T. Koschny, and C. M. Soukoulis. Magnetic response of metamaterials at 100 terahertz. *Science*, 306: 1351 – 1353, 2004.
- [29] S. Zhang, W. Fan, B. K. Minhas, A. Frauenglass, K. J. Malloy, and S. R. J. Brueck. Midinfrared resonant magnetic nanostructures exhibiting a negative permeability. *Phys. Rev. Lett.*, 94: 037402 – 37404, 2005.
- [30] U. K. Chettiar, A. V. Kildishev, H.K. Yuan, W. Cai, S. Xiao, V. P. Drachev, and V. M. Shalaev. Double negative index metamaterial: Simultaneous negative permeability and permittivity at 812 nm. *Photonics Metamaterials in OSA*, MA3, 2007.

- [31] U. K. Chettiar, A. V. Kildishev, H. Yuan, W. Cai, S. Xiao, V. P. Drachev, and V. M. Shalaev. Dual-band negative index metamaterial: Double-negative at 813 nm and single-negative at 772 nm. *Opt Lett.*, 32: 1671 – 1673, 2007.
- [32] S. Zhang, W. Fan, N. C. Panoiu, K. J. Malloy, R. M. Osgood, and S. R. J. Brueck. Experimental demonstration of near-infrared negative-index metamaterials. *Phys. Rev. Lett.*, 95: 137404, 2005.
- [33] V.P. Drachev, W. Cai, U. Chettiar, H. K. Yuan, A. K. Sarychev, A. V. Kildishev, G. Klimeck, and V. M. Shalaev. Experimental verification of an optical negative-index material. *Laser Phys. Lett.*, 3: 49 – 55, 2006.
- [34] T. A. Klar, A. V. Kildishev, V.P. Drachev, and V. M. Shalaev. Negative-index metamaterials: Going optical. *Selected Topics in Quantum Electronics, IEEE*, 12: 1106 – 1115, 2006.
- [35] A. K. Popov, S. A. Myslivets, T. F. George, and V. M. Shalaev. Compensating losses in positive- and negative-index metamaterials through nonlinear-optical quantum switching. In *Lasers and Electro-Optics - Pacific Rim, IEEE*, 2007.
- [36] M. W. Klein, M. Wegener, N. Feth, and S. Linden. Experiments on second- and third-harmonic generation from magnetic metamaterials. *Optics Express*, 15: 5238 – 5247, 2007.
- [37] A. K. Popoy and Y. M. Shalaev. Negative-index metamaterials: second-harmonic generation, manley-rowe relations and parametric amplification. *Applied Physics*, 84: 131 – 137, 2006.
- [38] M. W. Klein, C. Enkrich, M. Wegener, and S. Linden. Second-harmonic generation from magnetic metamaterials. *Science*, 313: 502 – 504, 2006.
- [39] W. Cai, U. K. Chettiar, A. V. Kildishev, and V. M. Shalaev. Designs for optical cloaking with high-order transformations. *Optic Express*, 16: 5446, 2008.

-
- [40] F. Zhou, Y. Bao, W. Cao, C. T. Stuart, J. Gu, W. Zhang, and C. Sun. Hiding a realistic object using a broadband terahertz invisibility cloak. *Sci. Rep.*, 1: 78, 2011.
- [41] J. Li and J. B. Pendry. Hiding under the carpet: A new strategy for cloaking. *Phys. Rev. Lett.*, 101: 203901, 2008.
- [42] D. Schurig, J. J. Mock, B. J. Justice, S. A. Cummer, J. B. Pendry, A. F. Starr, and D. R. Smith. Metamaterial electromagnetic cloak at microwave frequencies. *Science*, 314: 977 – 980, 2006.
- [43] W. Cai, U. K. Chettiar, A. V. Kildishev, and V. M. Shalaev. Nonmagnetic cloak with minimized scattering. *Appl. Phys. Lett.*, 91: 111105, 2007.
- [44] W. Cai, U. K. Chettiar, A. V. Kildishev, and V. M. Shalaev. Optical cloaking with metamaterials. *Nature Photon.*, 1: 224 – 227, 2007.
- [45] Z. Liu, H. Lee, Y. Xiong, C. Sun, and X. Zhang. Far-field optical hyperlens magnifying sub-diffraction-limited objects. *Science*, 315: 1686, 2007.
- [46] D. Lu and Z. Liu. Hyperlenses and metalenses for far-field super-resolution imaging. *Nat. Commun.*, 3: 1205, 2012.
- [47] T. Taubner, D. Korobkin, Y. Urzhumov, G. Shvets, and R. Hillenbrand. Near-Field Microscopy through a SiC Superlens. *Science*, 313 (5793): 1595, 2006.
- [48] N. Fang, H. Lee, C. Sun, and X. Zhang. Sub-diffraction-limited optical imaging with a silver superlens. *Science*, 308 (5721): 534 – 537, 2005.
- [49] W. Cai, D. A. Genov, and V. M. Shalaev. Superlens based on metal-dielectric composites. *Phys. Rev. B.*, 72: 193101, 2005.
- [50] I. S. Nefedov and S. A. Tretyakov. Waveguide containing a backward-wave slab. *Radio Science*, 38 (6): 1101, 2003.

-
- [51] Y. Yu, Z. Yang, M. Zhao, and P. Lu. Broadband optical circular polarizers in the terahertz region using helical metamaterials. *J. Opt.*, 13: 055104, 2011.
- [52] X. Ma, C. Huang, M. Pu, C. Hu, Q. Feng, and X. Luo. Multi-band circular polarizer using planar spiral metamaterial structure. *Opt. Express*, 20 (14): 16050 – 16058, 2012.
- [53] C. Han and W. Y. Tam. Plasmonic ultra-broadband polarizers based on Ag nano wire-slit arrays. *Appl. Phys. Lett.*, 106: 081102, 2015.
- [54] B. Shen, P. Wang, R. Polson, and R. Menon. Ultra-high-efficiency metamaterial polarizer. *Optica*, 1 (5): 356 – 360, 2014.
- [55] A. L. Rakhmanov, A. M. Zagoskin, S. Savelev, and F. Nori. Quantum metamaterials: Electromagnetic waves in a Josephson qubit line. *Phys. Rev. B.*, 77: 144507, 2008.
- [56] J. Q. Quach, C. Su, A. M. Martin, A. D. Greentree, and L. C. L. Hollenberg. Reconfigurable quantum metamaterials. *Opt. Express*, 19 (12): 11018 – 11033, 2011.
- [57] J. Plumridge, E. Clarke, R. Murray, and C. Phillips. Ultra-strong coupling effects with quantum metamaterials. *Solid State Commun.*, 146: 406 – 408, 2008.
- [58] Z. Alexandre. Quantum metamaterials: concept and possible implementations. In *Meta Conferences, Meta'12*, 2011.
- [59] D. Pile. Metamaterials mature. *Nature Photonics*, 6(7): 419, 2012.
- [60] P. Jung, A. V. Ustinov, and S. M. Anlage. Progress in superconducting metamaterials. *Supercond. Sci. Technol.*, 27: 073001, 2014.
- [61] C. L. Cortes, W. Newman, S. Molesky, and Z. Jacob. Quantum nanophotonics using hyperbolic metamaterials. *J. Opt.*, 14: 063001 – 063016, 2012.

-
- [62] M. Asano, M. Bechu, M. Tame, S. K. Ozdemir, R. Ikuta, D. O. Guney, T. Yamamoto, L. Yang, M. Wegener, and N. Imoto. Distillation of photon entanglement using a plasmonic metamaterial. *Sci. Rep.*, 5: 18313, 2015.
- [63] T. Roger, S. Vezzoli, E. Bolduc, J. Valente, J. F. Heitz, J. Jeffers, C. Soci, J. Leach, C. Couteau, N. I. Zheludev, and D. Faccio. Coherent perfect absorption in deeply subwavelength films in the single-photon regime. *Nat. Commun.*, 6: 7031, 2015.
- [64] K. R. McEnery, M. S. Tame, S. A. Maier, and M. S. Kim. Tunable negative permeability in a quantum plasmonic metamaterial. *Phys. Rev. A.*, 89: 013822, 2014.
- [65] Z. Jacob, J. Y. Kim, G. V. Naik, A. Boltasseva, E. E. Narimanov, and V. M. Shalaev. Engineering photonic density of states using metamaterials. *Appl. Phys. B.*, 100: 215 – 218, 2010.
- [66] M. A. Noginov, H. Li, Y. A. Barnakov, D. Dryden, G. Nataraj, G. Zhu, C. E. Bonner, M. Mayy, Z. Jacob, and E. E. Narimanov. Controlling spontaneous emission with metamaterials. *Opt. Lett.*, 35: 1863 – 1865, 2010.
- [67] S. M. Wang, S. Y. Mu, C. Zhu, Y. X. Gong, P. Xu, H. Liu, T. Li, S. N. Zhu, and X. Zhang. Hong-Ou-Mandel interference mediated by the magnetic plasmon waves in a three-dimensional optical metamaterial. *Opt. Express*, 20(5): 5213 – 5218, 2012.
- [68] K. P. Jha, X. Ni, C. Wu, Y. Wang, and X. Zhang. Metasurface-enabled remote quantum interference. *Phys. Rev. Lett.*, 115: 025501, 2015.
- [69] T. S. Kuhn. *The Structure of Scientific Revolutions*. The University of Chicago Press, London, fourth edition, 2012.
- [70] Z. Nouredine. *Quantum Mechanics: Concepts and Applications*. John Wiley and Sons, 2009.
- [71] S. Franco. *Wave-Particle Duality*. Springer Science and Business Media, 2012.

- [72] D. Sen. The uncertainty relations in quantum mechanics. *Curr. Sci.*, 107(2): 203 – 218, 2014.
- [73] E. Schrodinger. The present situation in quantum mechanics. In *Proceedings of the American Philosophical Society*, volume 124, pages 323 – 338, 1925.
- [74] M. A. Nielsen and I. L. Chuang. *Quantum Computation and Quantum Information*. Cambridge University Press, New York., 10th anniversary edition edition, 2010.
- [75] M. Siomau, A. A. Kamli, S. A. Moiseev, and B. C. Sanders. Entanglement creation with negative index metamaterials. *Phys. Rev. A.*, 85(5): 050303, 2012.
- [76] M. S. Tame, K. R. McEnery, S. K. Ozdemir, J. Lee, S. A. Maier, and M. S. Kim. Quantum plasmonics. *Nat. Phys.*, 9: 329 – 40, 2013.
- [77] C. Wang, C. Du, and X. Luo. Surface plasmon resonance and super-resolution imaging by anisotropic superlens. *J. Appl. Phys.*, 106: 064314, 2009.
- [78] K. Kim, Y. Oh, W. Lee, and D. Kim. Plasmonics-based spatially activated light microscopy for super-resolution imaging of molecular fluorescence. *Opt. Lett.*, 35(20): 3501 – 3503, 2010.
- [79] A. V. Kabashin, P. Evans, S. Pastkovsky, W. Hendren, G. A. Wurtz, R. Atkinson, R. Pollard, V. A. Podolskiy, and A. V. Zayats. Plasmonic nanorod metamaterials for biosensing. *Nat. Mater.*, 8: 867 – 871, 2009.
- [80] F. Hao, Y. Sonnefraud, P. V. Dorpe, S. A. Maier, N. J. Halas, and P. Nordlander. Symmetry breaking in plasmonic nanocavities: Subradiant lspr sensing and a tunable fano resonance. *Nano Lett.*, 8(11): 3983 – 3988, 2008.
- [81] I. Berini and D. Leon. Surface plasmon-polariton amplifiers and lasers. *Nat. Photonics*, 6: 16 – 24, 2011.

- [82] R. M. Ma, R. F. Oulton, V. J. Sorger, and X. Zhang. Plasmon lasers: Coherent light source at molecular scales. *Laser Photonics Rev.*, 7: 1 – 21, 2012.
- [83] O. Hess, J. B. Pendry, S. A. Maier, R. F. Oulton, J. M. Hamm, and K. L. Tsakmakidis. Active nanoplasmonic metamaterials. *Nature Mater.*, 11: 573 – 584, 2012.
- [84] V. Giannini, A. I. Fernandez-Dominguez, S. C. Heck, and S. A. Maier. Plasmonic nanoantennas: Fundamentals and their use in controlling the radiative properties of nanoemitters. *Chem. Rev.*, 111: 3888 – 3912, 2011.
- [85] S. A. Maier. *Plasmonics: Fundamentals and Applications*. Springer Science and Business Media LLC, 2007.
- [86] R. Matthew, C. M. Claire, Z. Jie, L. Weiyang, M. H. Christine, Z. Qiang, Q. Dong, and X. Younan. Controlling the synthesis and assembly of silver nanostructures for plasmonic applications. *Chem. Rev.*, 111: 3669 – 3712, 2011.
- [87] L. Xin and M. T. Swihart. Heavily-doped colloidal semiconductor and metal oxide nanocrystals: an emerging new class of plasmonic nanomaterials. *Chem. Soc. Rev.*, 43: 3908 – 3920, 2014.
- [88] C. F. Bohren and D. R. Huffman. *Absorption and Scattering of Light by Small Particles*. John Wiley & Sons, Inc., 1983.
- [89] R. G. Newton. *Scattering theory of waves and particles*. Springer Science and Business media, LLC, 1982.
- [90] A. Boltasseva and V. M. Shalaev. Fabrication of optical negative-index metamaterials: Recent advances and outlook. *Metamaterials*, 2: 1 – 17, 2008.
- [91] V. M. Shalaev, W. Cai, U. K. Chettiar, H.K. Yuan, A. K. Sarychev, V. P. Drachev, and A. V. Kildishev. Negative index of refraction in optical metamaterials. *Opt. Lett.*, 30: 3356 – 3358, 2005.

-
- [92] W. S. Cai, U. K. Chettiar, H. K. Yuan, V. C. de Silva, A. V. Kildishev, V. P. Drachev, and V. M Shalaev. Metamagnetics with rainbow colors. *Opt. Express*, 15: 3333 – 3341, 2007.
- [93] E. Plum, V. A. Fedotov, A. S. Schwanecke, N. I. Zheludev, and Y. Chen. Giant optical gyrotropy due to electromagnetic coupling. *Appl. Phys. Lett.*, 90: 223113, 2007.
- [94] G. Dolling, C. Enkrich, M. Wegener, C. M. Soukoulis, and S. Linden. Low-loss negative-index metamaterial at telecommunication wavelengths. *Opt. Lett.*, 31: 1800, 2006.
- [95] G. Dolling, M. Wegener, C. M. Soukoulis, and S. Linden. Negative index metamaterial at 780 nm wavelength. *Opt. Lett.*, 32: 53, 2007.
- [96] C. Enkrich, F. Perez-Willard, D. Gerthsen, J. Zhou, T. Koschny, C. M. Soukoulis, M. Wegener, and S. Linden. Focused-ion-beam nanofabrication of near-infrared magnetic metamaterials. *Adv. Mater.*, 17: 2547 – 2549, 2005.
- [97] T. Morita, R. Kometani, K. Watanabe, K. Kanka, Y. Haruyama, and T. Hoshino. Free-space-wiring fabrication in nano-space by focused-ion beam chemical vapor deposition. *J. Vac. Sci. Technol. B.*, 21: 2737 – 2742, 2003.
- [98] S. J. Corbitt, M. Francoeur, and B. Raeymaekers. Implementation of optical dielectric metamaterials: A review. *J. Quant. Spectrosc. Radiat. Transfer.*, 158: 3 – 16, 2015.
- [99] S. R. J. Brueck. Optical and interferometric lithography nanotechnology enablers. *Proc. IEEE*, 93: 1704, 2005.
- [100] N. Feth, C. Enkrich, M. Wegener, and S. Linden. Large-area magnetic metamaterials via compact interference lithography. *Opt. Express*, 15: 501, 2006.

-
- [101] S. Zhang, W. Fan, N. C. Panoiu, K. J. Malloy, R. M. Osgood, and S. R. J. Brueck. Experimental demonstration of near-infrared negative-index metamaterials. *Phys. Rev. Lett.*, 95: 137404, 2005.
- [102] S. Fan, S. Zhang, K. J. Malloy, and S. R. J. Brueck. Large-area, infrared nanophotonic materials fabricated using interferometric lithography. *J. Vac. Sci. Technol. B.*, 23: 2700, 2005.
- [103] Z. Ku and S. R. J. Brueck. Comparison of negative refractive index materials with circular, elliptical and rectangular holes. *Opt. Express*, 15: 4515, 2007.
- [104] S. Y. Chou, P. R. Krauss, and P. J. Renstrom. Nanoimprint lithography. *J. Vac. Sci. Technol. B.*, 14: 4129, 1996.
- [105] W. Wu, E. Kim, E. Ponizovskaya, Z. Liu, Z. Yu, N. Fang, Y. R. Shen, A. M. Bratkovsky, W. Tong, C. Sun, X. Zhang, S. Y. Wang, and R. S. Williams. Optical metamaterials at near and mid-IR range fabricated by nanoimprint lithography. *Appl. Phys. A.*, 87: 147, 2007.
- [106] W. Wu, Z. Yu, S. Y. Wang, R. B. Williams, Y. Liu, C. Sun, X. Zhang, E. Kim, R. Shen, and N. Fang. Midinfrared metamaterials fabricated by nanoimprint lithography. *Appl. Phys. Lett.*, 90: 063107, 2007.
- [107] Y. Chen, J. Tao, X. Zhao, Z. Cui, A. S. Schwanecke, and N. I. Zheludev. Nanoimprint lithography for planar chiral photonic meta-materials. *Microelectron. Eng.*, 78 - 79: 612 – 617, 2005.
- [108] Y. Chen, Y. Zhou, G. Pan, and E. Huq. Nanofabrication of SiC templates for direct hot embossing for metallic photonic structures and metamaterials. *in: Micro- and Nano Engineering Conference Proceedings*, MNE07: 592, 2007.
- [109] S. W. Pang, T. Tamamura, M. Nakao, A. Ozawa, and H. Masuda. Direct nano-printing on Al substrate using a SiC mold. *J. Vac. Sci. Technol. B.*, 16: 1145, 1998.

-
- [110] G. Dolling, M. Wegener, and S. Linden. Realization of a three functional layer negative-index photonic metamaterial. *Opt. Lett.*, 32: 551, 2007.
- [111] G. Dolling, C. Enkrich, M. Wegener, C. M. Soukoulis, and S. Linden. Simultaneous negative phase and group velocity of light in a metamaterial. *Science*, 312: 892, 2006.
- [112] S. Subramania and S. Y. Lin. Fabrication of three-dimensional photonic crystal with alignment based on electron beam lithography. *Appl. Phys. Lett.*, 85: 5037, 2004.
- [113] D. F. V. James, P. G. Kwiat, W. J. Munro, and A. G. White. Measurement of qubit. *Phys. Rev. A.*, 64: 052312, 2001.
- [114] M. Planck. On the improvement of Wien's equation for the spectrum. *Verh. dtsh. phys. Ges. Berlin*, 2: 202 – 204, 1900.
- [115] A. Einstein. On a heuristic point of view about the creation and conversion of light. *Ann. Physik*, 17: 132 – 148, 1905.
- [116] G. N. Lewis. The conservation of photons. *Nature*, 118: 874 – 875, 1926.
- [117] P. A. M. Dirac. The quantum theory of the emission and absorption of radiation. *Proc. R. Soc. Lond. A.*, 114: 243 – 265, 1927.
- [118] M. O. Scully and M. Sargent. The concept of the photon. *Physics Today*, 25(3): 38 – 47, 1972.
- [119] T. H. Maiman. Stimulated optical radiation in ruby. *Nature*, 187: 493 – 494, 1960.
- [120] C. C. Gerry and P. L. Knight. *Introductory Quantum Optics*. Cambridge University Press, Cambridge, 2005.
- [121] R. Loudon. *The Quantum Theory of Light*. Oxford University Press, Oxford, 3rd edn edition, 2000.

- [122] B. J. Pearson and D. P. Jackson. A hands-on introduction to single photons and quantum mechanics for undergraduates. *Am. J. Phys.*, 78: 471, 2010.
- [123] S. Bettelli. Comment on "coherence measures for heralded single-photon sources". *Phys. Rev. A.*, 81: 037801, 2010.
- [124] E. Huttler and J. H. Fendler. Exploitation of localized surface plasmon resonance. *Adv. Matter*, 16: 1685 – 1706, 2004.
- [125] J. N. Damask. *Polarization optics in Telecommunications*. Dordrecht: Springer, 2004.
- [126] T. Chen, S. Li, and H. Sun. Metamaterials application in sensing. *Sensors*, 12: 2742 – 2765, 2012.
- [127] R. Tyan, A. A. Salvekar, H. Chou, C. Cheng, A. Scherer, P. Sun, F. Xu, and Y. Fainman. Design, fabrication, and characterization of form-birefringent multilayer polarizing beam splitter. *Opt. Soc. Am. A.*, 14: 1627 – 1636, 1997.
- [128] E. H. Land. Some aspects of the development of sheet polarizers. *J. Opt. Soc. Am.*, 41: 957 – 963, 1951.
- [129] J. Y. Chin, M. Lu, and T. J. Cui. Metamaterial polarizers by electric-field-coupled resonators. *Appl. Phys. Lett.*, 93: 251903, 2008.
- [130] Y. Zhao and A. Alu. Tailoring the dispersion of plasmonic nanorods to realize broadband optical meta-waveplates. *Nano Lett.*, 13: 1086 – 1091, 2013.
- [131] A. Alu and N. Engheta. *Structured Surfaces as Optical Metamaterials*. New York: Cambridge University Press, 2011.
- [132] D. G. Zhang R. S. Zheng P. Wang Y. H. Lu K. Q. Lin, L. M. Wei and H. Ming. Temperature effects on prism-based surface plasmon resonance sensor. *Chin. Phys. Lett.*, 24: 3081, 2007.

-
- [133] D. B. Leviton and B. J. Frey. Temperature-dependent absolute refractive index measurements of synthetic fused silica. In J. Antebi E. Atad-Ettedgui and D. Lemke, editors, *Proc. in SPIE Astronomical Telescopes and Instrumentation*, page 6273K. SPIE, Bellingham, 2006.
- [134] C. K. Hong and L. Mandel. Experimental realization of a localized one-photon state. *Phys. Rev. Lett.*, 56: 58 – 60, 1986.
- [135] D. C. Burnham and D. L. Weinberg. Observation of simultaneity in parametric production of optical photon pairs. *Phys. Rev. Lett.*, 25: 84 – 87, 1970.
- [136] I. L. Chuang and M. A. Nielsen. Prescription for experimental determination of the dynamics of a quantum black box. *J. Mod. Opt.*, 44: 2455, 1997.
- [137] M. Abdullah, A. L. Farooqui, J. Breeland, M. I. Aslam, M. Sadatgol, M. S. Tame S. K. Ozdemir, L. Yang, and D. O. Guney. Quantum entanglement distillation with metamaterials. *Opt. Express*, 23: 17941, 2015.
- [138] A. Poppe, A. Fedrizzi, T. Loruenser, O. Maurhardt, R. Ursin, H. R. Boehm, M. Peev, M. Suda, C. Kurtsiefer, H. Weinfurter, T. Jennewein, and A. Zeilinger. Practical quantum key distribution with polarization-entangled photons. *Opt. Express*, 12: 3865, 2004.
- [139] T. Driscoll, S. Palit, M. M. Qazilbash, M. Brehm, F. Keilmann, B. G. Chae, S. J. Yun, H. T. Kim, S. Y. Cho, N. M. Jokerst, D. R. Smith, and D. N. Basov. Dynamic tuning of an infrared hybrid-metamaterial resonance using vanadium dioxide. *Appl. Phys. Lett.*, 93: 024101, 2008.
- [140] X. Liu and W. J. Padilla. Thermochromic infrared metamaterials. *Adv. Mater.*, 28: 871, 2016.

-
- [141] W. Lewandowski, M. Fruhnert, J. Mieczkowski, C. Rockstuhl, and E. Gorecka. Dynamically self-assembled silver nanoparticles as a thermally tunable metamaterial. *Nat. Commun.*, 6: 6590, 2015.
- [142] H. D. Zeh. On the interpretation of measurement in quantum theory. *Foundations of Physics*, 1: 69 – 76, 1970.
- [143] S. Diehl, A. Micheli, A. Kantian, B. Kraus, H. P. Buchler, and P. Zoller. Quantum states and phases in driven open quantum systems with cold atoms. *Nat. Phys.*, 4: 878 – 883, 2008.
- [144] H. Krauter, C. A. Muschik, K. Jensen, W. Wasilewski, J. M. Petersen, J. I. Cirac, and E. S. Polzik. Entanglement generated by dissipation and steady state entanglement of two macroscopic objects. *Phys. Rev. Lett.*, 107: 080503, 2011.
- [145] F. Verstraete, M. M. Wolf, and J. I. Cirac. Quantum computation and quantum state engineering driven by dissipation. *Nat. Phys.*, 5: 633 – 636, 2009.
- [146] B. Liu, L. Li, Y. Huang, C. Li, G. Guo, E. Laine, H. Breuer, and J. Piilo. Experimental control of the transition from markovian to non-markovian dynamics of open quantum system. *Nat. Phys.*, 7: 931 – 934, 2011.
- [147] J. T. Barreiro, M. Muller, P. Schindler, D. Nigg, T. Monz, M. Chwalla, M. Hennrich, C. F. Roos, P. Zoller, and R. Blatt. An open-system quantum simulator with trapped ions. *Nature*, 470: 486 – 491, 2011.
- [148] F. A. Wudarski and F. Petruccione. Robustness and fragility of markovian dynamics in a qubit dephasing channel. *Phys. Rev. A.*, 95: 052130, 2017.
- [149] A. Rivas, S. F. Huelga, and M. B. Plenio. Quantum non-markovianity: characterization, quantification and detection. *Rep. Prog. Phys.*, 77: 094001, 2014.

-
- [150] M. M. Wolf, J. Eisert, T. S. Cubitt, and J. I. Cirac. Assessing non-markovian quantum dynamics. *Phys. Rev. Lett.*, 101: 150402, 2008.